The Dissertation Committee for Akshay Kumar Singh Certifies that this is the approved version of the following dissertation:

Trion and Exciton Dynamics in Two Dimensional Semiconductors

Committee:

Xiaoqin Li, Supervisor

Chih-Kang Shih

Michael C. Downer

Qian Niu

Seth R. Bank

Trion and Exciton Dynamics in Two Dimensional Semiconductors

by

Akshay Kumar Singh, B. Tech

Dissertation

Presented to the Faculty of the Graduate School of

The University of Texas at Austin

in Partial Fulfillment

of the Requirements

for the Degree of

Doctor of Philosophy

The University of Texas at Austin

May 2016

Dedication

Dedicated to my parents, family and friends.

Acknowledgements

Doing a PhD was certainly the most challenging and fun adventure for me. The fact that it extended over an extended period of six years meant a continuous cycle of ups and downs, which I would not have been able to go through if not for my set of support pillars.

Firstly I would like to thank my parents. The weekly skype meetings and continuous encouragement and support was incredibly helpful. My sisters and extended family were a source of constant enthusiasm and pampering. From creating an intellectual atmosphere in my home to supporting my move away to another country, they were right with me. I would also like to thank my friends living in India who continually encouraged me.

The scientific journey would not be possible without my advisor, Elaine Li, who gave me the maximum support possible. We had many engaging and stimulating scientific discussions, as well as conversations about my career. She gave me the freedom to grow, but at the same time helped me in doing work in the most efficient way.

I would like to acknowledge the support of my dissertation committee for their useful feedback and constant encouragement.

The members of Li group were incredibly awesome and helpful in the lab. Firstly, I would like to appreciate the guidance provided by Yanwen Wu and Brian Ruzicka during the initial stages of working in the lab. The senior members of the lab including Daniel Birt, Farbod Shafifei, Daniel Ratchford and Megan Creasey also helped me getting started. The second generation of the lab, including me, Tom Hartsfield, Kavir Dass and Kyongmo An, started together. I would like to appreciate the constant help and

banter provided by these members. Kha Tran, who is taking over the setup after I leave, was really fun to work with and a big help in the lab. I hope that I have left a decently working lab behind, for him to do great things. Jinwei Shi, Gabriel Cossio, Liuyang Sun, Kai Hao, Junho Choi and Joe Seifert were also great lab members to work with. I would also like to acknowledge and appreciate Galan Moody and Mirco Kolarczik for their help in the scientific process including writing and analysis. I also acknowledge the support given by my collaborators, Xiaodong Xu, Markus Betz and Ulrike Woggon. I also appreciate the cheerfulness spread by the TU-Dortmund lab members during my short visit to Dortmund.

I would further like to thank the people working in the machine shop especially Ed Baez and Jack Clifford, and the jovial administrators on the fifth floor including Matt Erwin, Lisa Gentry, Eric Patowski and Michele Landfield. I would also like to thank Downer lab group members for their help.

Life outside the lab was also a lot of fun and my friends provided me a lot of happiness. They acted as my family in Austin for which I am exceedingly grateful. I would like to acknowledge my apartment mates – Mukund, Akhilesh and Vineet, who had to put up with me during graduate school. I would like to thank Gaurav Chaudhary, Avni, Shravya, Priya, Gunja and Rachit for their continual affection. I also appreciate Sucheta, Akanksha Jain, Subhamoy, Riddhi, Ramya, Suyog, Esha, Abhishek Baradia, Siddharth, Garima, Gaurav Assat, Anand Surada and Spandana, for their never ending enthusiasm. I would also like to raise a toast to my crown and anchor Friday evening buddies, Abhimanyu, Rashish, Nishant and Prashant.

Finally, I would like to thank my running group friends. It would be hard to imagine my life in Austin, without the Run for India group. So long, and thanks for all the gatorade.

Trion and Exciton Dynamics in Two Dimensional Semiconductors

Akshay Kumar Singh, PhD

The University of Texas at Austin, 2016

Supervisor: Xiaoqin Li

Two-dimensional semiconducting systems have become increasingly important for a variety of applications including photo-detectors, high-power transistors and optoelectronics. With the discovery of the indirect-to-direct bandgap transition in atomically thin transition metal dichalcogenide (TMDs') materials, a plethora of further applications and advances await. Optical properties in these materials are especially interesting to measure, due to presence of spin-valley coupling giving rise to valleytronic applications, and enhanced light emission (and absorption) with applications in optoelectronics.

Optical studies in semiconductors near the bandgap primarily relate to the fundamental optical excitation of semiconductors, an exciton (a Coulomb-bound electron-hole pair). If the Coulomb interaction is strong enough, excitons may capture an extra electron or hole, forming charged excitons known as trions. Trions have shown to carry longer-lived spin information, and can drift under an electric field. The interaction between excitons and trions, is thus a technologically important issue in optoelectronics.

The purpose of this dissertation is to measure the interactions between excitons and trions in a variety of two-dimensional systems, primarily in the new class of semiconducting two-dimensional materials, TMDs'. The interactions are measured for their character (coherent or incoherent) and dynamics. Utilizing a two-color pump-probe

setup we uncover coherent coupling, between excitons and trions in monolayer molybdenum diselenide, an order of magnitude larger than traditional semiconductors (like gallium arsenide). Incoherent relaxation pathways towards trions, are measured via resonant excitation of excitons. A mobility edge within the exciton resonance is uncovered, with applications in quantifying transport properties of materials under study. Further, valley sensitive measurements are carried out on monolayer tungsten diselenide, revealing the long-lived trion spin polarization and ultrafast exciton valley relaxation. The possible spectroscopy feature of biexcitons is discussed in monolayer tungsten diselenide. Finally, measurements are extended to high mobility gallium arsenide quantum well systems, and electron-density dependent spin scattering mechanisms are uncovered. We further discuss the possibility to suppress spin relaxation, via gate voltage, in these gallium arsenide quantum wells.

Table of Contents

List of Tables

List of Figures

Chapter 1: Motivation

SEMICONDUCTORS AND ELECTRONICS

Semiconductors are ubiquitous in today's world encompassing fields of electronics and energy. It is surprising though when we realize that semiconductors are a relatively new class of materials compared to metals and insulators. The first documented study of semiconductors was in the 1830's when Faraday reported decreasing resistance of silver sulfide when heated, contrary to commonly seen behavior for metals. The generation of voltage when light is incident, or photovoltaic effect, was seen by Becquerel in 1837.

Semiconductors can be thought of having an intermediate bandgap between conductors (zero bandgap) and insulators (large bandgap). The use of an electron as an information carrier began with semiconductors. The ability to control the electron flow by utilizing a gate voltage created innumerable applications for these materials. First transistors were developed in the beginning of the 20th century and are now at the heart of all electronics. The field has come a long way from the time when Wolfgang Pauli criticized it as "wallowing in dirt" [1]. The dirt he was referring to are dopants in the semiconductors, which have since been realized as tuning knobs to create photovoltaic devices and diodes [2]. Fabrication techniques including molecular beam epitaxy have been improved tremendously to create ultra-pure materials which provide even more control for semiconductor devices [3]. The state of the art is less than 1 part impurity atoms in a billion desired semiconductor atoms. This has given rise to high mobility transistors and efficient electronic and photovoltaic devices.

The quest towards miniaturization of semiconductor transistors has been an interesting one and has been driven by advances in fabrication [4]. The ask is to pack

more transistors on a chip which yields speed, cost as well as energy benefits. This follows the guiding principle of Moore's law which envisaged doubling of transistors on a chip every two years [5,6]. Remarkably, this "law" has held true for over 50 years led by progress in fabrication and manufacturing techniques. Techniques like photolithography and roll-to-roll manufacturing have been developed to work on a large scale [7]. The miniaturization quest has led to new questions being asked related to the quantum nature of transport of electrons. As the size of the transistors has been reduced, from ~ 10 μm in 1965 to ~10 nm in 2015, quantum effects have come into focus [8]. Quantum tunneling which gives rise to leakage current and reduces efficiency of devices is a leading cause of noise for these tiny devices. Figure 1.1, courtesy Intel Inc., addresses these concerns towards scaling of devices and the need to explore material space.

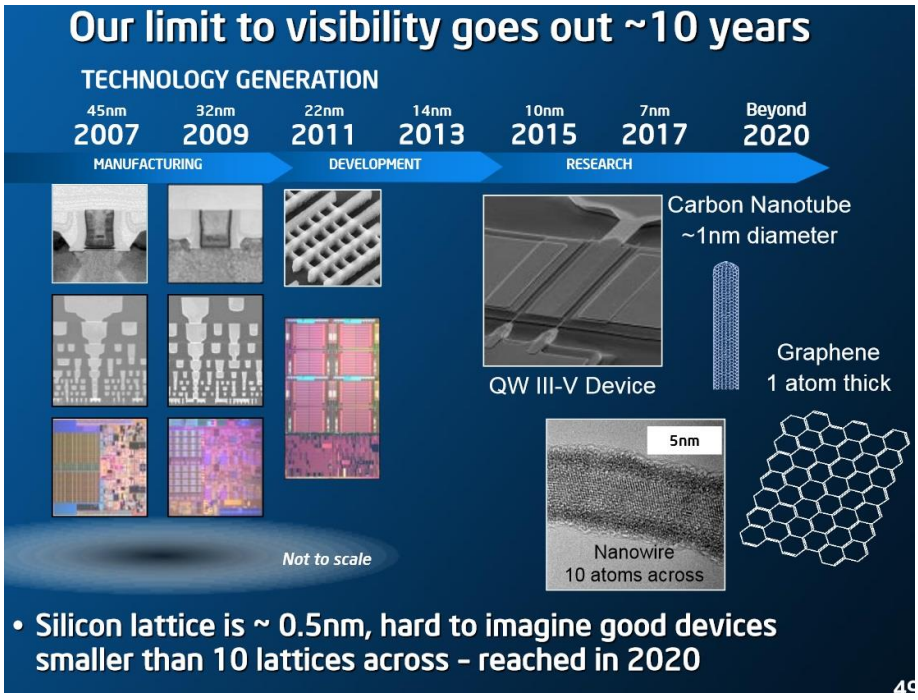

Figure 1.1: Schematic of Intel Inc. technology road map.

The choice of material for these transistors has, since the inception, been silicon (a typical transistor is illustrated in Figure 1.2 [9]). Silicon, an indirect bandgap semiconductor, is widely available in nature in compound form with oxygen, namely silicon oxide or silica. Silica can be purified to create mono-crystalline silicon which can be used to create wafers for use in integrated circuits. The compound is however what makes use of silicon widespread. The oxide can easily be grown on top of the pure silicon and acts as an insulating layer reducing current leakage. Additionally the oxide insolubility in water provides robustness to the transistor and ease in fabrication. Thus, even though germanium is technologically superior (higher mobility and better transport properties), due to germanium oxide being soluble in water, silicon is preferred and almost exclusively used.

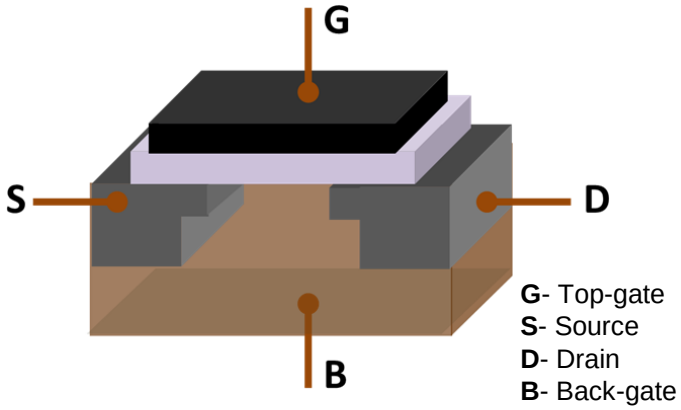

Figure 1.2: Typical structure of a MOSFET (Metal Oxide Semiconductor Field Effect Transistor).

A transistor, briefly consists of three parts. The semiconductor is separated from the metallic gate (G) by an oxide layer (gate dielectric layer). The source (S) and drain (D) are doped semiconductors and the current flow can be controlled using the gate voltage. Two key figures of merit for transistors and integrated circuits are the on-off

ratio for current and the ability to control the current flow with the minimum gate voltage possible. The on-off ratio is the ratio of current when the transistor is switched on and the current when no voltage is applied. It is basically a measure of current leakage and the ability to switch devices. This affects the speed at which devices work (frequency of operation) and the energy used when switched off or when in stand-by power mode. With the advent of portable devices, the thrust is towards lower power applications which makes the leakage current an important beast to control. The second figure of merit, voltage required for switching, is also similarly important for high frequency transistors and the power used for operation. The gate voltage essentially controls the speed at which electron current traverses the conduction channel of the transistor. If lower voltages can be used for switching (referred to as voltage required for subthreshold decade swing), then the energy towards powering the device can be reduced, leading to less heat generation as well and providing tremendous energy and environmental savings.

As transistors are made smaller, the thickness of the silicon oxide is reduced to increase gate capacitance and thereby increase current flow. The capacitance of the dielectric oxide layer is an important tuning parameter in the design of the transistor and can be written as

$$C = {(\kappa\epsilon_0)A}/{t} \tag{1.1}$$

, where A= area and t= thickness of oxide. Thus, capacitance is directly proportional to the dielectric constant and inversely proportional to thickness of the oxide. The quest towards increasing capacitance by decreasing thickness however leads to increasing current leakage through quantum tunneling. Another direction being taken is the replacing of silicon oxide with high dielectric constant material (high κ materials) to

reduce current leakage [10,11]. These high κ materials provide an opportunity to scale down transistors by providing a physically thicker layer (to reduce quantum tunneling current) while increasing gate capacitance to boost current flow (through a larger dielectric constant compared to silicon oxide). In other words, a thicker layer can be used to provide same capacitance and lower leakage current (exponentially lower leakage since quantum tunneling current scales as *exp(-t))*.

More importantly, it is becoming clear that silicon may not be the material of choice for transistors moving forward. Other materials like gallium arsenide (GaAs), graphene and non-planar geometries (nanotubes, nanowires, three dimensional transistors) are being explored (see Figure 1.1) [12]. These materials provide various tuning knobs, from higher electron mobilities to easier fabrication.

The most common technique for fabrication of silicon and other semiconductor based transistors is photolithography [13,14]. Briefly, the technique utilizes a physical mask (fabricated by other nano-lithography techniques like e-beam lithography) which is patterned with the requisite features. A suitable photoresist is deposited on the oxide followed by light incidence (lamp light or laser), shadowed by the physical mask. Subsequently, chemical etchants are used to remove the non-exposed parts. Naturally, the limiting factor for the smallest feature size here is the size of the mask and the wavelength of the light used. Photolithography techniques have progressed from using 400 nm Mercury lamp light in 1960's to utilizing 194 nm argon fluoride lasers with a subsequent feature size reduction from micron scale to ~ 20 nm. Thus, photolithography and the semiconductor industry have greatly benefited from the improvement in laser technology. The use of low wavelength lasers however, have additional constraints namely absorption by air in the ultraviolet wavelength range, which necessitate the use of vacuum pumps increasing cost of production [15]. Additionally, the lithography process

has to be repeated many times in a commercial fabrication facility. Consequently, these top down techniques are not scalable beyond a certain point and can be cost prohibitive. Bottom-up techniques might be worth exploring.

Bottom up fabrication techniques involve the growth of structures from the desired material [16-18]. The processes could be solution based or vapor based (chemical vapor deposition). Nanostructures down to arbitrary size (down to few atoms) and shape (circular, cylindrical, pyramidal) can be created with a very fine control on the critical dimension. Size fluctuations can be reduced tremendously and the cost of manufacturing reduced dramatically. The size and dimension control goes beyond the control offered by top-down techniques and will be discussed further in section 1.3.

An important fundamental question is whether other particles (or excitations), separate from charge of electrons can be used as information carriers. We will explore the possibility of light and optical excitations as information carriers in the next section. We will also explore the possibility of spin of the electron as a means of communication and use in electronics in section 1.4.

LIGHT MATTER INTERACTIONS

The interaction of light with matter is one of the broadest fields in science and has been studied since time immemorial. Light is used to measure as well as modify properties of materials. Light can be used to drive chemical reactions, act as activation agents and as catalysts [19,20]. Light can be used to slow down the vibrations of objects and cool them down to ultracold (nanokelvin) temperatures [21]. Conversely, matter can be designed to trap light to enhance absorption (use in solar cells) or slow light down to fractions of speed of light in vacuum or even localize it completely [22,23].

Light (used interchangeably with electromagnetic waves) spans a large range of length scales. In order of decreasing wavelength scales, light can be of the form of radio waves (m to km), microwaves (mm to m), infrared (μm to mm), visible (350 to 700 nm), ultraviolet (10 to 400 nm), x-rays (0.01 to 10 nm) or gamma-rays (λ < 1e-12 m). These length scales are illustrated in Figure 1.3, along with corresponding frequencies (in hertz) and energy (in electron-volts, eV). These different forms of light can be used to measure and control physical phenomena at different length scales. Radio waves are the backbone of communication. They are used for over-the-air television broadcasts, phone communication and radar. Microwaves can be used to measure spatial location (GPS), for heating and power and for communication. The study of celestial objects (astronomy) is heavily dependent on the analysis of microwaves. Infrared radiation (and absorption by earth) is responsible for regulating earth temperatures. The ability to see things comes from the reflection and scattering of visible light from objects. Meanwhile, different objects having varied colors results from the fundamental and engineered properties of materials. For example, the different colors of aluminum oxide (alumina) are due to the small impurities of dopants (or impurities) which can make alumina blue (sapphire) or red (ruby) or anything in between and beyond. Further, ultraviolet light is utilized for driving chemical reactions and use in arc lamps. It is also important for use in photolithography and high spatial resolution imaging techniques. X-rays can be used to measure the internal structure of materials and medical radiography in treating cancer and are widely used in crystallography. The study of gamma rays in astronomy is important for characterizing supernovae and pulsars.

Sources of electromagnetic radiation covering these wavelengths are present in nature as we have discussed briefly. For example, gamma rays are created by spontaneous nuclear reactions and stars, infrared waves are radiated by heated objects.

However, these are quite limited in their scope and is difficult to control them. Lasers (Light amplification by stimulated emission of radiation) covering a range of these wavelengths are available now. Further, lasers in continuous as well as pulsed form have been developed. Lasers started with the development of masers (microwave lasers) in 1953 and rapidly extended to visible light lasers (ruby laser, 1960). Currently, the laser spectrum has extended to generating coherent X-rays [24]. Laser systems are of various types depending on applications (pulse-width and band-width) and extend from gas based lasers (helium-neon, excimer) to dye lasers and solid state lasers (semiconductor, fiber). Table top laser sources have been responsible for revolutions in the medical, industrial and scientific domains. These laser systems, generating different wavelengths, can be used to probe phenomenon at diverse length-scales.

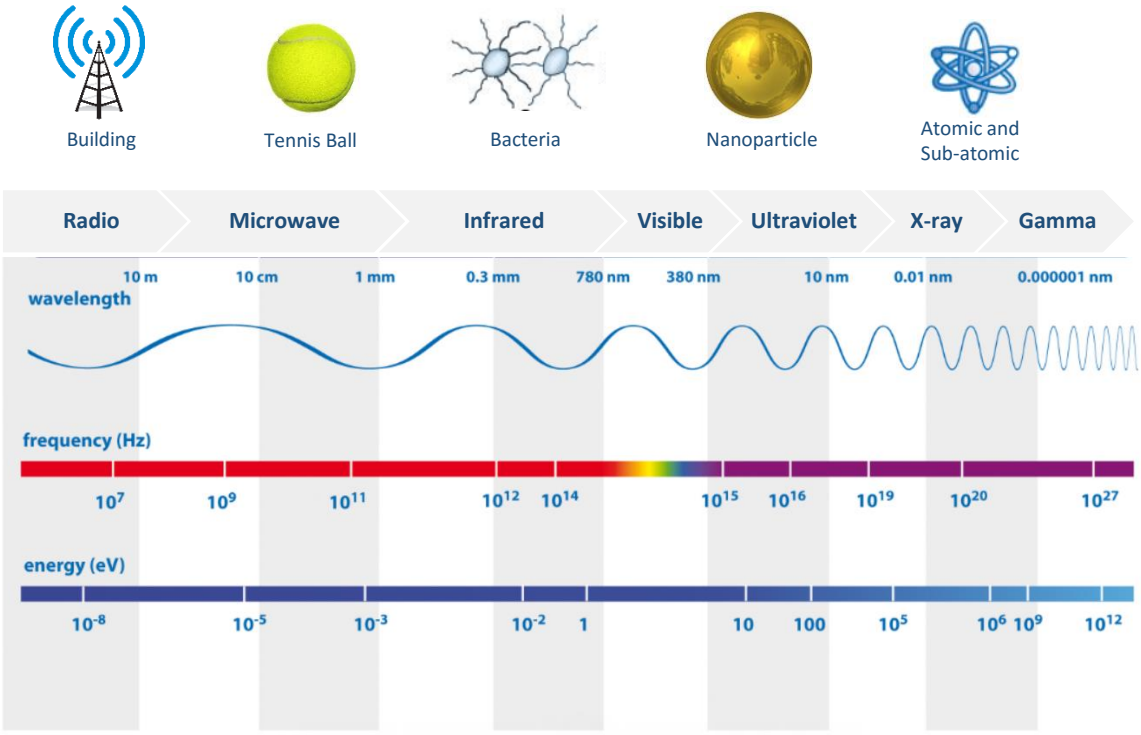

Figure 1.3: Schematic of length scales in the Electromagnetic spectrum.

Light spanning this large length-scale range is intrinsic to length scale of matter in the universe. Additionally, the concept of matter behaving as wave (wave-particle duality) was described by Debroglie in 1924. Importantly, the beauty of interaction of matter with light (or electromagnetic waves) is that it can be described by a set of four length invariant equations, the Maxwell equations.

$$\nabla \times H = J_c + {}^{\delta D}/_{\delta t} \tag{1.2}$$

$$\nabla \times E = -{}^{\delta B}/_{\delta t} \tag{1.3}$$

$$\nabla . D = \rho \tag{1.4}$$

$$\nabla . B = 0 \tag{1.5}$$

These equations were proposed by Maxwell in 1861 and have been utilized to solve problems involving the interaction of electric and magnetic fields (of light) with matter. These equations are invoked for describing dipole radiation, propagation of waves in crystals and scattering problems [25,26]. The list and scope is truly endless. Further, the scale invariance of the equations has been exploited to create new areas of research exemplified by nano-photonics which have taken device know-how at the microwave and radiowave scale and extended them to visible light [27-29].

Maxwell equations have been used to design structures over a large length scale range as well as explain physical phenomenon. On the other hand, there are active fields of research looking beyond Maxwell equations, which are classical in nature, and extend the physics to quantum phenomena [30]. At small length scales (~ 1 nm), the conventional rules (Maxwell) have to be re-examined and a full quantum treatment might be necessary. For example, quantum plasmonics is a dynamic field of research dealing with extreme confinement of visible light using metal nanoparticles revealing nature of quantum tunneling and creating applications in nanoscale photochemistry [31,32].

The wavelength regime of near-ultraviolet, visible and NIR (near infrared) light is referred to as the optical regime. The interaction of optical light with matter is particularly interesting due to a number of reasons. Most (organic and inorganic) semiconductors have bandgaps in the region of 1 – 3 eV (400 – 1000 nm) (bandgap can be thought of as minimum photon energy required for excitation from the ground state to the first excited state, bandgaps are a consequence of crystal symmetry and wave reflection and will be discussed in chapter 2 in detail). Thus, visible and NIR light are ideal for investigation of semiconductor phenomena. Additionally, some metals have interband transitions in the visible range and thus can be optically probed [33]. Further, metallic nanoparticles scatter light in the visible range and thus can be used for a variety

of applications including extreme confinement of light and photovoltaic devices [34,35]. This relatively new field of plasmonics has also led to a number of innovations including cheap water purifiers and devices with enhanced chemical sensitivity (for detection of small quantities of compounds) [36]. On the other hand, the use of light to visualize biological processes is not new, indeed the first microscopes were created in 1600's. Optical microscopes though suffer from limited spatial resolution, limited by wavelength of the light used (Abbe diffraction limit ~ $\lambda/2$). Recently however, imaging techniques have seen great improvement, beating the diffraction limit and successfully bringing optical microscopy techniques to the nanoscale. These super-resolution microscopy techniques utilize light emitting fluorophores, nonlinear effects of light and tailored illumination [37,38]. These techniques were awarded the chemistry Nobel Prize in 2014. Another great example of visible light matter interaction is the chemical process of photosynthesis. In most organisms, the molecules responsible for photosynthesis (present in chlorophyll) absorb only the visible portion of the sunlight. Interestingly, beautiful non-linear spectroscopy experiments revealed the quantum nature of transport of electrons in plants undergoing photosynthesis [39,40]. The photosynthetic process was found to result from a coherent interaction of light with the molecules (coherent and incoherent coupling processes will be discussed in chapter 2 and chapter 4).

The other reason why the optical regime is more studied than other regimes is the large availability of semiconductor and other table-top laser sources. Semiconductors emit light (spontaneous or stimulated) in the energy range of their bandgap which can be utilized to measure other semiconductors and materials. This bandgap as we have discussed, is in the optical regime. The semiconductors can be driven electrically (electroluminescence), can be put in an optical cavity to create coherent laser light or used in engineered diode structures to generate light [41-43]. Additionally, easily

available incoherent sources, like incandescent lamps, have their emission spectrum in the range of 400 - 1000 nm, resulting from the blackbody radiation of the heated filament of the bulb. This incoherent light can be used to measure scattering cross-sections of nanoparticles and for optical microscopy helpful in microstructure characterization [34]. Further, coherent laser sources can be used to measure the dynamic evolution of quantum processes as also discussed earlier in context of photosynthesis. Interestingly, non-linear effects requiring high light intensities were made possible only through the development of lasers and made easier through pulsed sources [44,45]. Presently, there has been much work on developing infrared and terahertz laser sources which can probe intraband transitions in semiconductors [46,47]. As a result, these intraband transitions which provide information into the internal structure and interactions of the bands, are now accessible [48]. Thus, the correlation between light sources and interesting physics being discovered and studied is clear.

Measuring certain quantum effects (Rabi frequency, Quantum entanglement) have been possible only after invention of coherent laser light sources [49,50]. The studies of these quantum effects have led to vast interest in controlling bits of information for computing purposes. The field of quantum computing has specific advantages over classical computing including use of qubits (quantum bits) which work in Hilbert space rather than classical space and thus can be faster in certain cases [51-53]. The control of these qubits are done by employing a set of lasers and the use of flying qubits (photons) can enhance the large spatial separation of networks and make error correction scalable [54,55].

Certain aspects of the quantum nature of light matter interaction though were revealed even before lasers were invented. Quasiparticles in semiconductors are a beautiful example of emergent quantum phenomena in physics, which were studied

before the advent of lasers. Interactions and correlations amongst simple constituents can give rise to complex phenomena when they behave collectively [56-58]. These emergent phenomena are widespread in nature including motion of flock of birds and traffic patterns, and extend to physical systems [58,59]. Quasiparticles in solid state physics arise due to complex interactions between electrons and/or the crystal lattice. Quasiparticles are essentially simplifications to the full quantum mechanical many-body problem in semiconductors and other materials.

Quasiparticles in semiconductors are of different types. There are fermionic quasiparticles, following Fermi-Dirac statistics. Electrons in a crystal as well as a hole, left behind after an electron is excited (from the ground state to the excited state), are fermionic quasiparticles. Electrons in a semiconductor have different effective masses than free electron masses and are affected by the dielectric environment. Another interesting example is the Majorana fermion which has attracted considerable interest in the community (it is a particle which is its own antiparticle) but is beyond the scope of this work [60]. Additionally, there are bosonic quasiparticles which means they follow Bose-Einstein statistics. Quantum of crystal (atoms in the crystal) vibrations are phonons, quantum of magnetic excitations are magnons and quantum of electron oscillations are plasmons (quantum literally means a discrete quantity). Coulomb bound electron-hole pairs are called excitons, they are optically generated and are bosonic [61,62]. Interestingly, composite quasiparticles, for example trions, are a combination of electrons (fermionic) and excitons (bosonic) and are a result of doped systems [63,64]. Trions are fermionic and will be discussed in much detail in chapter 2, along with excitons. The bosonic quasiparticles have integer spin while the fermionic quasiparticles (electrons in crystals, holes) have n × (1/2) spin, where n is an odd integer. Further, the energy of a bosonic quasiparticle can simply be written as

$$E = hv \tag{1.6}$$

, where h is Planck's constant and v is the frequency (of excitation or creation) associated with the quasiparticle. As we have mentioned, quasiparticles in semiconductors were studied even before the advent of lasers. The discovery of excitons predates the invention of lasers and showed up as optical transitions, below the band gap, in absorption experiments [65,66]. However, lasers completely revolutionized the study of excitons and other quasiparticles. They offered unprecedented possibilities to study the dynamics as well as manipulate these quasiparticles. At present, time scales of exciton creation-annihilation and interaction with other quasiparticles (phonons, trions) have been studied extensively utilizing pulsed as well as continuous laser sources. We will discuss these quasiparticles in detail in this dissertation, specifically in chapter 2 and in the experimental sections. Further, excitons have technological importance in creating white light sources and enhancing absorption for photo-voltaic applications [67,68]. In context of optoelectronic circuits, they can also be considered as information carriers and the importance of these quasiparticles is set to increase in the coming years.

The dynamics of the light-matter interactions occur over a large time scale range. Some of these dynamics are summarized in figure 1.4. A wide variety of materials have electron and impurity spins of the order of a microsecond to a second [69,70]. Recently, spin lifetimes of the order of minutes was found in silicon [71]. However, most of these are better addressed by electrical means. The dynamics occurring on the fast (nanosecond) to ultrafast (picosecond, femtosecond) are best addressed through the optical route. As, we will also see in this dissertation, the dynamics involving the optical quasiparticles (excitons, trions) occur over a range of few femtoseconds to few

nanoseconds [72,73]. The shortest laser pulses are of the order of a few atto-seconds and are being used to probe dynamics on the atomic scale [74].

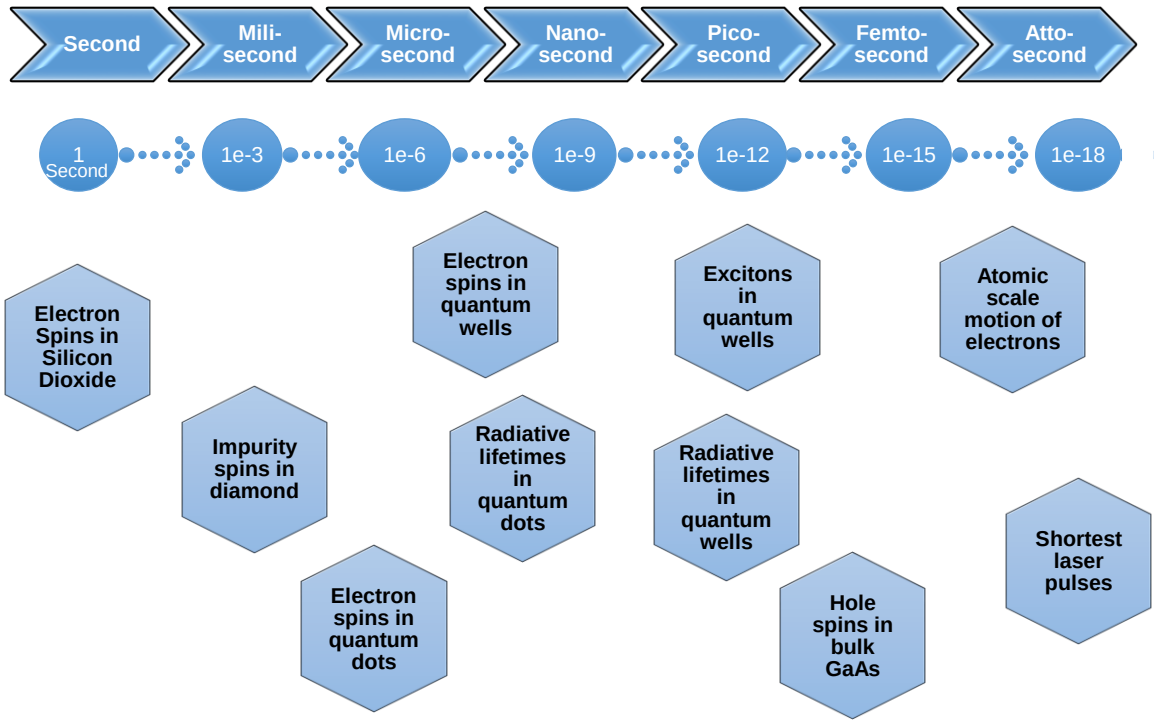

Figure 1.4: Illustration of the time scale of different physical processes in semiconductors.

LOW DIMENSIONAL SEMICONDUCTORS

In our discussions till now, we have not made a distinction between bulk and low dimension semiconductors. The physics in these two cases is very different. For example, the spin lifetimes of holes in quantum wells is larger than in the bulk. Most of these effects, as we will discuss in much detail in chapter 2, originate due to confinement of the electron (and hole) wavefunctions spatially. Additional effects arise due to reduction of screening of electronic interactions in low dimensional systems. In this section, we will

mainly look at the different systems studied and their fabrication techniques. We will mostly concentrate on bottom-up techniques.

Bottom-up techniques, as we have discussed, offer fine control on the size and shape of the structures. Compared to top-down they are much easily scalable, once the process is perfected. The most common growth technique used for bottom-up fabrication is chemical vapor deposition. The technique (illustrated in figure 1.5) involves a sealed chamber in which gases and evaporants can be introduced. The evaporant is a precursor to the material desired to be deposited. The gases can act as carriers (neutral, inert gases) or reaction agents (react with precursors). With a fine control of temperature, flow rate and choice of precursor, the desired shape and size can be fabricated [75,76]. Quantum wells and quantum dots are however also grown by a different method, molecular beam epitaxy (MBE), which has high control over the concentration of impurities. Further, quantum dots can also be created in solution and hence are inherently scalable.

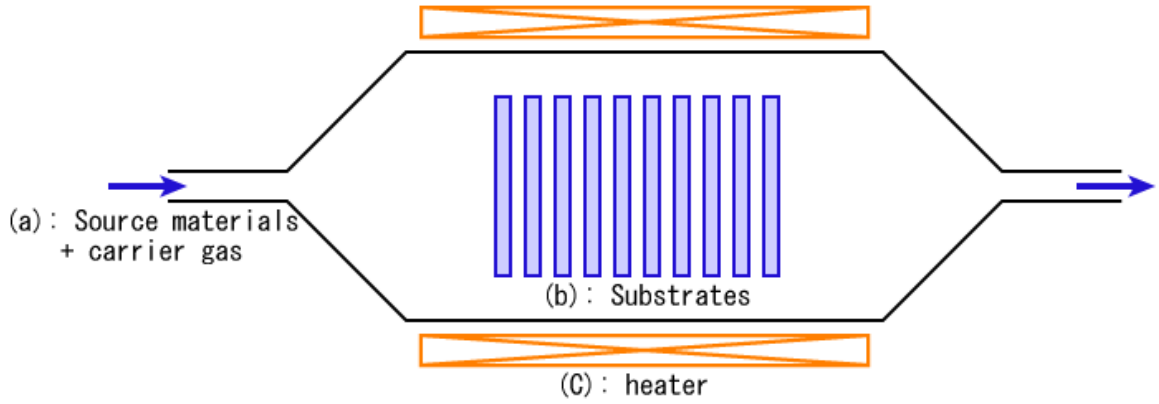

Figure 1.5: A typical Chemical Vapor Deposition setup.

Quantum wells offer two dimensional confinement of electrons (electrons are confined to move in two dimensional space). They were one of the first two-dimensional semiconductors studied and are primarily grown by MBE. Primarily, there are III-V

(Gallium Arsenide, Indium Arsenide) and II-VI (Cadmium Telluride) quantum wells, which offer different characteristics to choose from. Quantum wells consist of a thin layer (usually ~ 10 – 20 nm) of a lower bandgap material sandwiched by higher bandgap materials, which are usually lattice matched (to reduce strain). For example, a thin layer of gallium arsenide sandwiched between two layers of aluminum gallium arsenide (GaAs/AlGaAs) forms a quantum well, the thin layer offering quantum confinement. The choice of thickness of the quantum well layer, in the context of causing quantum confinement, is governed by the Bohr radius and will be discussed in chapter 2. Historically, the first quantum wells suffered from a high concentration of impurities and low quality interfaces between the barrier and the quantum well. The technology improved though, and the applications emerged, including lighting, lasers and photovoltaics. These applications resulted from a fundamental change in dynamics from bulk, including increased radiative rates and increased mobilities. Further, quantum wells are ideal test beds for studying quantum theories of confinement [77,78]. Additionally, multiple quantum wells could be grown in close proximity (variable distances ~ 10 nm) and quantum tunneling could be studied [79]. Currently, quantum wells with magnetic dopants are being used for use in spintronics, but are beyond the scope of this dissertation. Wide quantum wells (thickness of the order of Bohr radius) are especially interesting because they offer excellent transport properties and have higher spin lifetimes [80,81]. The spin relaxation mechanisms in these materials are not well understood and we will discuss these in chapter 2 and chapter 6.

It was clear from the study of the quantum wells that controlling the interface is important. Further, there was a quest to find other two-dimensional (2D) semiconductors which offer excellent transport properties and enhanced optical characteristics and at the same time, have easier fabrication processes. There was also a thrust to find

semiconductors which might be useful in flexible electronics and could possibly be strain tuned. The discovery of graphene and the excellent transport properties (high mobilities) revolutionized the field of ultrathin semiconductors. It was discovered that by sticking tape to a piece of graphite and removing it, high quality and crystalline single layers of carbon could be created (mechanical exfoliation) [82]. Graphene has interesting physical properties including a Dirac cone in its energy-momentum space, zero bandgap, high carrier velocities, a honeycomb crystal structure and great mechanical strength. The zero bandgap however posed issues in implementing graphene as a possible alternative semiconductor to silicon. As we discussed, the presence of this bandgap decides the on-off ratio of a semiconductor. Thus, there was no mechanism to switch off an intrinsic graphene transistor. There was a great move towards trying to chemically generate a bandgap by introducing intercalants, but these caused the mobilities to decrease tremendously (high mobilities made graphene attractive for applications) [83,84]. The best use of graphene was found to be as transparent electrodes and even in fuel cells. Thus, there was a need to explore the material space beyond graphene.

The pursuit to find a 2-D semiconductor persisted. Single layer graphene could be easily exfoliated from graphite because different layers in graphite were held together by weak van der Waals forces. This also gave rise to graphite's lubricating properties. The quest was narrowed to bulk materials with similar lubricating properties. In 2010, the first member of a different class of materials was discovered by two groups simultaneously [85,86]. They studied a class of semiconducting materials called transition metal dichalcogenides (TMD's), consisting of a transition metal (tungsten, molybdenum) and a chalcogen (sulphur, selenium). It was found while exfoliating bulk crystals of these TMD's to single layers (specifically molybdenum sulfide), the ensuing monolayers underwent a bandgap change. A transition from an indirect bandgap in bulk (similar to

silicon) to direct bandgap in monolayers (similar to gallium arsenide) was proposed and supported through first principal calculations and photoluminescence measurements. A number of measurements including angle resolved photoemission spectroscopy and scanning electron microscopy confirmed the wonderful thickness dependent bandgap in these materials [87,88]. Further, the bulk crystals had been shown to have strong excitonic transitions [65,89]. These excitonic transitions were enhanced in the monolayers due to the direct bandgap nature and were shown to dominate the optical response, even at room temperature. The excitonic nature of these transitions is fundamentally interesting to study and has great fundamental applications including in transport [90]. These materials have high absorption coefficients at the excitonic resonances (~ 10%) and thus can be used for photovoltaic applications. Further, a number of studies have shown increased electronic interactions in these materials (compared to GaAs and other semiconductors) [91,92]. They also show spin-valley coupling and have applications in valleytronics [93,94]. Additionally, strain tuning has shown to drastically change the optical resonances in these materials, furthering the applicability in displays and other devices [95,96]. These materials will be, along with quantum wells, the focus of this dissertation. We will specifically look at the dynamics of the interactions and characterize coupling strengths between excitonic quasiparticles. We will also investigate the spin-valley polarization and the time-scales involved in the spin relaxation in these new class of semiconductors.

Single layers of these materials have wonderful properties. The next question was whether these could be combined or stacked on top of each other to tailor response according to the applications. These has much work on combining these van der Waals systems and creating new systems with desirable properties. This is also illustrated in figure 1.6 where the van der waals materials can be considered as Lego blocks [97]. Due

to the van der Waals nature of these materials, predicting the properties of the heterostructures is possible, because they are weakly interacting. Some wonderful examples of heterostructures are ultra-sensitive photodetectors, indirect excitons and chiral light emitting diodes [98-101]. Along with different materials being used, twist angle of the stacking, as well as doping can be used as important tuning parameters [102]. This is an exciting field and is bound to expand in the coming years but is not the focus of this dissertation.

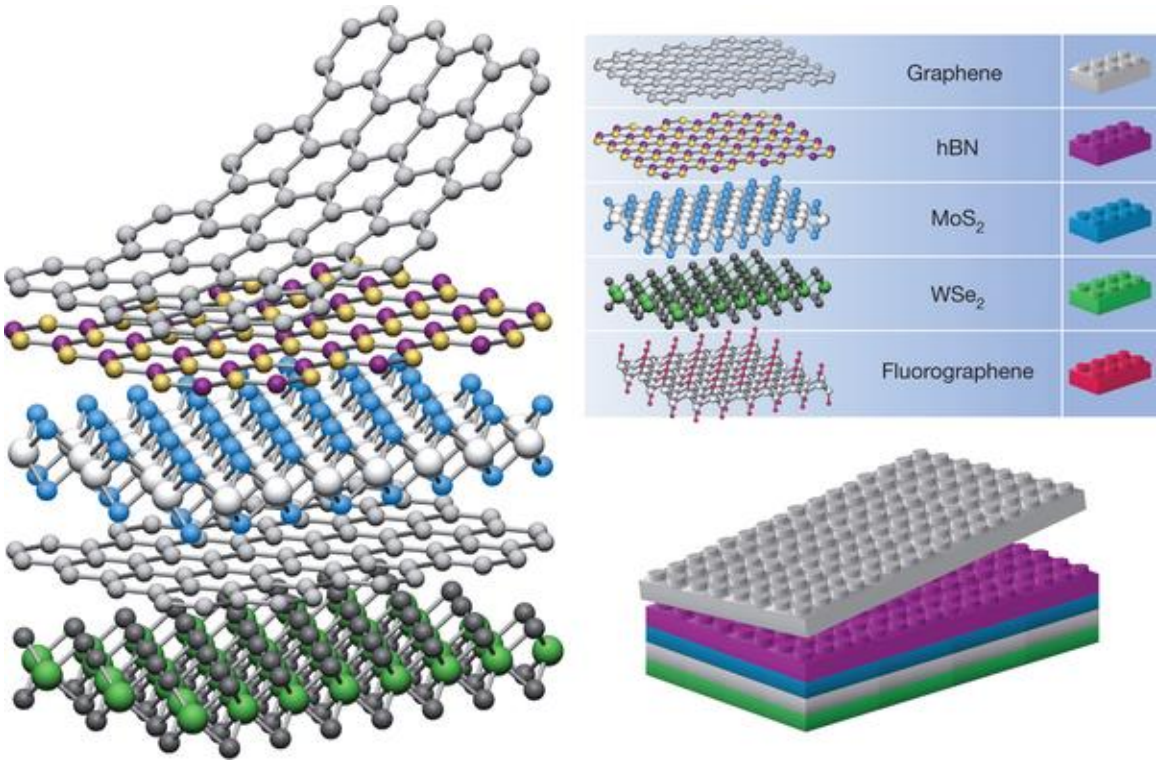

Figure 1.6: Illustration of heterostructures created, with single layers depicted as Lego blocks.

SPINTRONICS

Spintronics is simply, electronics with the spin (of an electron) being used as the information carrier. Using the spin offers a number of advantages including lower

switching powers and larger relaxation times, as we have discussed in the previous section [103]. Spintronics is not a new field and the first generation of spintronic devices have been so extensively used that it is difficult to imagine life without them. They have been used in hard-drives, MRAM's and other electronic applications. The second generation relates to the transport properties of these spins. These include phenomenon like spin valves (spin filtering) [104], spin transfer torque [105] (spin momentum transfer to magnetic domains and induced magnetization change), and spin hall effect [106] (generating spin polarized currents). Figure 1.7 shows an illustration of the basic challenge in spintronics. Consider the spin of the electron modelled as a spinning top. The challenge is to get a spinning top (up or down spin) to maintain its precession (by reducing spin-scattering or spin-flip processes) and also to study the decay processes inherent to the system.

Figure 1.7: Illustrating an ideal spinning top, which spins indefinitely, vs a real spinning top, governed by decay processes.

Current is defined as motion of charge under the application of an electric field in the direction of the applied lateral field. Spin current on the other hand, involves the motion of a spin-polarized, i.e. different density of up and down electrons (spin is the fourth quantum number of an electron and reveals itself under application of a magnetic

field, intrinsic or extrinsic). Consider a flow of electrons such that all the spin up electrons move to one side of our conducting channel and all the spin down to the other side. This would result in a spin current without any motion of charge. This current is predicted to more easily switchable giving rise to lower power electronic devices, the switching energy up to a magnitude lower than end of road CMOS devices [103].

Most of the spintronics applications we have discussed till now involve ferromagnets and other magnetic components. However, the large spin relaxation times of (impurity) spins in pure materials (silicon, diamond) can also be utilized for information storage over long time scales. Further, spins with ultrafast (picosecond) relaxation times, which can be addressed optically, could also be useful in switching and computation. In TMD's and quantum wells, the spins of the excitonic quasiparticles (excitons, trions) can be selectively addressed using circularly polarized light [23,93,107-109]. Thus an imbalance in spin population can be generated and can be used for computation and transport. In this dissertation, we will measure the spin relaxation times for excitonic quasiparticles in these materials. We will also discuss the new paradigm of spin-valley coupling in TMD's in chapter 2.

Chapter 2: Low Dimensional Semiconductors and Optical Quasiparticles

In the previous chapter we have talked about the advent of semiconductors in the world of electronics. We have also talked about the fabrication and applications of these semiconductors. Further, we introduced concepts about light and matter interaction including the concept of quasiparticles. It is important that we look into these in some detail in this chapter. We also discuss in this chapter, the two physical systems, quantum wells and transition metal dichalcogenides, which are the focus of this dissertation. The concepts of nonlinear spectroscopy are introduced in this chapter and will be extended in the experimental setup section (chapter 4).

Optical Band-Gaps and Bloch Functions

The bandgap is the most fundamental property measured in an optical analysis of the material. A semiconductor as we defined in the previous chapter, can be thought of "having an intermediate bandgap between conductors (zero bandgap) and insulators (large bandgap ~ 5 eV)." The bandgap decides the order of the magnitude of the conductivity, light absorption capabilities and imperative for all electronic applications. It is thus important to define the bandgap and its origin.

A simple way to explain the bandgap is, imagine you are sitting at the bottom of a hill of an unknown height. The only tools you have to measure the height of the hill is a ball and an apparatus to measure the launch speed of the ball. When the ball is thrown up with just the appropriate speed, the ball scales the hill and the height is determined using $height = {(speed)^2}/{2g}$, where g is the gravitational constant. In an experiment with light and an unknown semiconductor, light plays the role of the ball, the bandgap of the unknown semiconductor is the hill (of the unknown height) and the speed of the ball

is the energy of the photon (of the light). Therefore the bandgap can simply be thought of as the (minimum) energy of the photon which can be absorbed by the material. The material is transparent to photon energies below the bandgap. Thus, the bandgap is related to the absorption edge of a semiconductor (minimum photon energy the material absorbs) and is important to be measured for optoelectronic and photovoltaic applications.

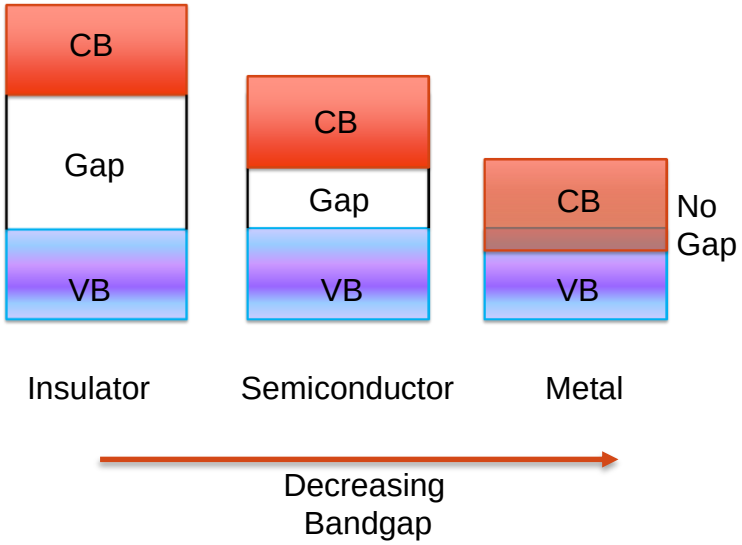

Figure 2.1: Bandgaps in different classes of materials.

We illustrate the bandgap for different materials in Figure 2.1. In this simplified figure, the conduction band (valence band) is represented by CB (VB). At absolute zero temperature, all electrons are in the valence band (also referred to as the crystal ground state). Electrons in the valence band can be thought of as electrons bound to atoms and not free to move. When the material is optically or thermally excited, some electrons jump into the conduction band. These electrons are free to move around in the material and result in a detectable current. In the figure, we classify different materials by the size

of the bandgap. For an insulator, the bandgap is large and hence there are almost no conduction electrons at room temperature. For a metal, the bandgap lies within the conduction band, in other words, the bandgap is zero. Thus there are always conduction electrons in a metal and there is no way to switch-off a metal. In between metals and insulators, with intermediate bandgaps, lie the semiconductors. This intermediate bandgap, with easily tunable conduction current makes semiconductors useful in electronics.

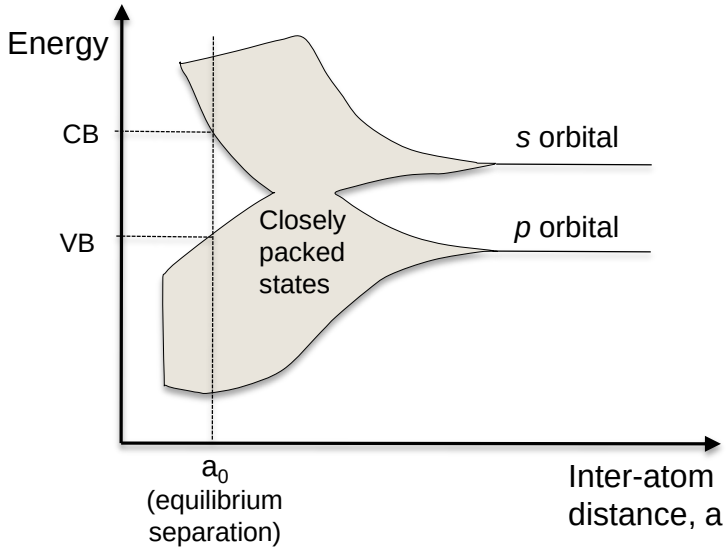

Figure 2.2: Evolution of bandgap as atoms (orbitals) are brought together in a crystal (solid).

The bandgap can be understood as a consequence of atoms and electrons arranged inside a crystal structure. The symmetry of the confining system and the repeating structure leads to profound consequences. There are a number of ways to explain the bandgap including Bloch geometry and orbital theory. The orbital theory is illustrated in Figure 2.2 and briefly explained. Stand-alone atoms can be described in terms of atomic orbitals (s, p, d etc.). When a large number of these atoms are brought together (or

arranged in a crystal), due to electrons being fermions, these atomic orbital states are not energy degenerate. The energy levels do not overlap and instead form closely packed states, or energy bands. At the equilibrium inter-atomic distance a_0, the energy of the system is minimized. At this distance, as is illustrated, there is an energy gap between the bands and thus a bandgap is created. Another important thing is the bands inherit properties of the atomic orbitals, thus the conduction band is *s*-like and the valence band is *p*-like. This is relevant in the context of optical selection rules and will be discussed in the section concerning optical quasiparticles. This simple picture is actually quite useful in explaining why certain optical transitions take place.

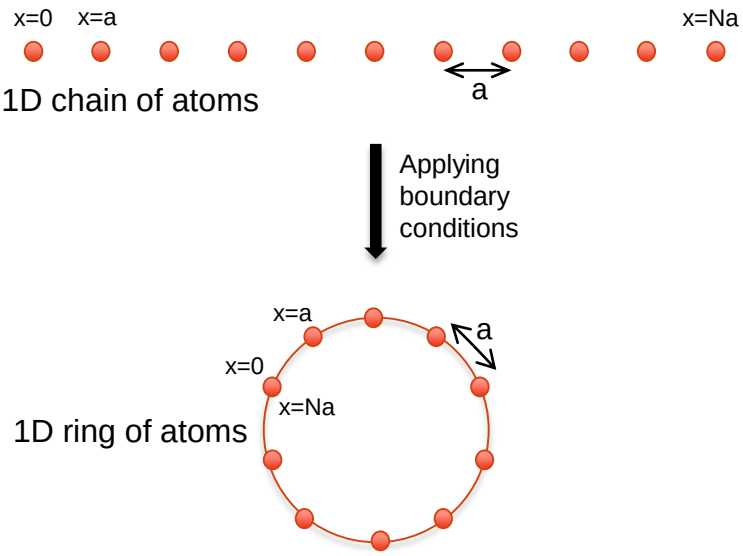

Figure 2.3: Illustration of one dimensional ring of atoms suitable for application of Bloch geometry constraints.

The simple picture of orbitals, though useful, does not satisfy the mathematical curiosity concerning the origin of bandgaps. We discuss bandgaps now in context of Bloch geometry. It is easiest to start with a one-dimensional (1D) ring of atoms. The 1D ring of atoms is a consequence of applying infinite number of atoms limit to a 1D chain

of atoms. Considering basic symmetry constraints and periodicity of the ring (illustrated in Figure 2.3), the dielectric function ϵ, is periodic in the lattice spacing a.

$$\epsilon(x) = \epsilon(x + sa), \text{ where } s \text{ is an integer} \tag{2.1}$$

Through this intrinsic translational symmetry, we then expect the wave-function to have the form

$$\psi(x + a) = C\psi(x), \text{ where } C \text{ corresponds to a phase factor.} \tag{2.2}$$

Through one trip of the ring containing N atoms, a phase C^N is accumulated. Since the wavefunction of the zero'th and the n'th atom should be the same (geometry of the ring), we have

$$\psi(x + Na) = \psi(x) = C^N\psi(x) \tag{2.3}$$

$$\Rightarrow \quad C = \exp(i2\pi sx/Na) \tag{2.4}$$

This leads to Bloch function

$\psi(x) = u_k(x)\exp(i2\pi sx/Na)$, where $u_k(x + a) = u_k(x)$ is the periodic part (2.5). This leads to the dispersion relation relating (angular) frequency and momentum

$$\omega(k) = \omega(k + G) \tag{2.6}$$

, where $G = 2\pi/a$ (reciprocal wave vector), k is the wave-vector. The consequences of equation 2.6 are illustrated in Figure 2.4. We draw the dispersion relation for a 1D ring

(or chain) in Figure 2.4(a) with an assumed speed (of mode) v. Here we illustrate linear bands, but the bands are actually of the form $\sin(ka/2)$ (considering nearest neighbor interactions [110]). This is of little significance in the present discussion and we can ignore the sine shape for now. We then use equation 2.6 to extend the k-space and move into the "repeated-zone" diagram (Figure 2.4(b)). We see that there are a number of band-crossings and additionally, the whole band-diagram can be represented in a reduced k-space, i.e. "reduced-zone" diagram (Figure 2.4(c)). This reduced k-space is also referred to as the Brillouin zone (B.Z.) of the crystal. Different materials have different crystal symmetries and hence the reciprocal wave-vectors are different as well. The calculation of the reciprocal wave vector can be done and hence the extent of the B.Z. can be computed. B.Z. is a convenient way to think about the crystal and the underlying structure.

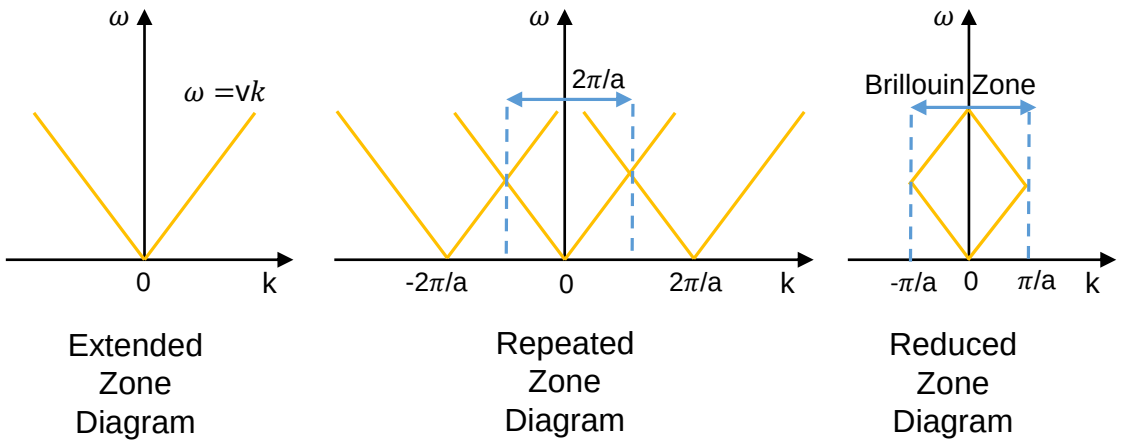

Figure 2.4: Illustration of the reduced zone diagram and the first Brillouin zone through Bloch geometry constraints.

Let us consider the 1D chain of atoms again (as illustrated in Figure 2.3). Consider a wave $\exp(ikx)$ incident on this chain of atoms from the left. All of these

atoms act as scattering centers. Consider an infinitely small reflectivity r, from each atom. Then we have the total reflected wave

$$re^{ikx} + re^{-i2ka}e^{ikx} + re^{-i4ka}e^{ikx} + \ldots\ldots = re^{ikx} * \frac{1}{1-e^{-i2ka}} \qquad (2.7)$$

This diverges if the denominator $1 - e^{-i2ka}$ goes to zero. This is also called the Bragg condition. Thus at $k = \pm\pi/a$, the wave function gets reflected. This is the physical consequence of the Brillouin zone. Thus a bandgap emerges at $k = \pm\pi/a$ and this opening of bandgap is illustrated in Figure 2.5. The size of the bandgap is related to the interaction of the electrons with the ion core of the atoms. Further explanation of the bandgap can be seen in the context of perturbation theory as well [110]. The size of the bandgap can be calculated through tight binding model (involving atomic orbitals) as well but these are beyond the scope and focus of this dissertation [111].

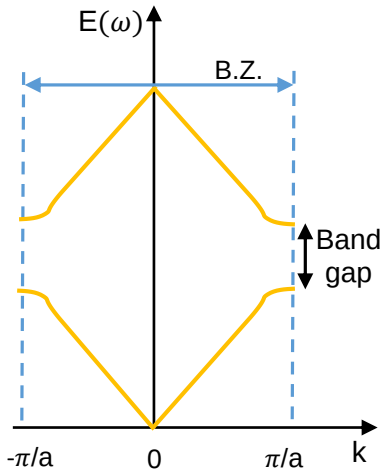

Figure 2.5: Opening up of band gap at the zone boundary.

So far we have illustrated linear bands. However, bands are of the form $\sin\left(ka/2\right)$. At low k values, these behave as linear bands since $\sin\left(ka/2\right) \sim ka/2$.

However, at the zone boundary, $\sin\left({ka}/{2}\right) \sim 1 - {(ka)^2}/{2}$. Thus at the edge of the B.Z., bands are parabolic. This will be discussed further in context of density of states. These parabolic bands can also be thought of as a consequence of the nearly free electron model, where $E \sim {\hbar^2 k^2}/{2m}$. Thus, these parabolic bands also lead to the effective mass picture, as we will see later in this chapter.

It is also important to explain the different types of bandgaps in different materials. Bandgaps can either be direct or indirect. These are classified in terms of whether light induced transitions can take place without help of phonons (quantum of lattice vibration) or impurity scatterers. This can be understood in terms of energy-momentum (E-k or ω-k) diagrams as illustrated in Figure 2.6. A photon of wavelength λ carries a momentum $p \sim 1/\lambda$, while a phonon carries momentum $p \sim 1/a$ (a is the unit cell dimension). Thus the momentum of a photon is much smaller than momentum carried by a phonon (λ~ 300 nm c.f. a ~ 0.3 nm). Thus any appreciable momentum can only be provided through a phonon. A photon (of visible light) carries no significant momentum. If the lowest energy transition occurs between two states having the same momentum (vertically aligned in the E-k diagram), and requires no extra momentum, then the bandgap is referred to as a direct bandgap. Conversely, if the lowest energy transition occurs between two bands with their maxima and minima misaligned in k-space, then phonons are needed to complete the transition. Optical transitions occurring in indirect bandgap materials are also called phonon assisted transitions. Also note in Figure 2.6, we have drawn parabolic bands, with the conduction and valence band being described earlier.

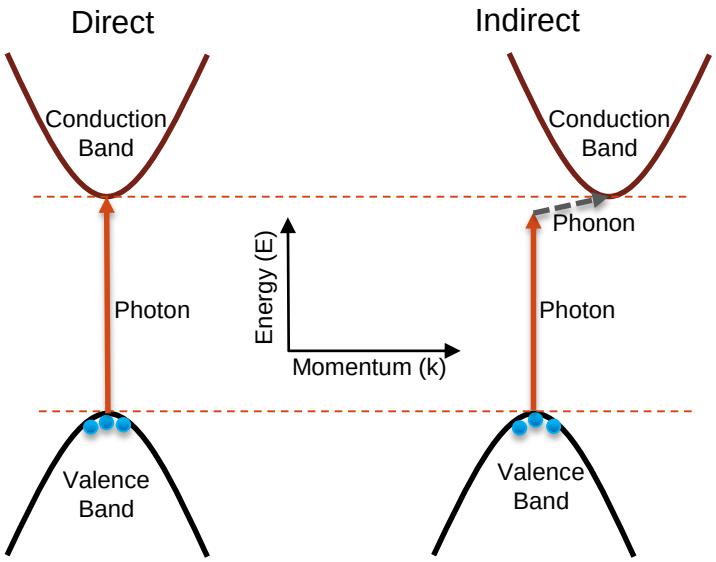

Figure 2.6: Illustration of indirect and direct bandgap through E-k diagrams. Electrons in valence band are shown through circles.

The consequences of a material having a direct or an indirect bandgap are profound. The absorption of a material with a direct bandgap is much stronger than an indirect bandgap material. This is due to the fact that direct optical transitions are first order in perturbation theory while indirect optical transitions, due to additional need of a phonon, are second order in perturbation theory. For example, gallium arsenide (a direct bandgap semiconductor) has much higher absorption than silicon (indirect bandgap). Thus, photovoltaic cells made of silicon have to be very thick (hundreds of micrometers) whereas direct bandgap materials can be much thinner (~ micrometers), to absorb all of the incident light. The same rules apply to luminescence or radiative recombination. After optical (or electrical) excitation, the electrons in a direct bandgap material can recombine with the holes (left behind in the valence band) and radiate light. This process is however, very unlikely in indirect bandgap semiconductors. Thus for use in lighting, direct bandgap semiconductors (example- gallium nitride for blue, aluminum gallium indium

phosphide for red) are almost exclusively used. Another interesting aspect is the temperature dependence of absorption. Due to the necessity of phonons in assisting indirect bandgap transitions, absorption coefficients can change with temperature much more in indirect bandgap semiconductors compared with direct bandgap materials. Therefore at low temperatures, indirect optical transitions are greatly inhibited due to a lack of considerable phonon population.

LOW DIMENSIONALITY AND QUANTUM CONFINEMENT

Confining the electron wavefunction spatially in any dimension has interesting effects. We start from the picture of a particle (electron) confined in a 1D potential well, i.e. possibility of (nearly free) motion in one direction with confinement in two directions. This is a fundamental quantum mechanical problem and we write the (familiar) energy equation

$$E_n = n_x^2 \left(\frac{\hbar^2\pi^2}{2m^*L^2}\right) + (n_y^2 + n_z^2)\left(\frac{\hbar^2\pi^2}{2m^*{L_c}^2}\right) \tag{2.8a}$$

, where L and L_c are the width of the sample and the well respectively, m* is the effective mass of the particle, which implies discrete energy levels for a particle in two directions and (almost) continuous energy levels in the other direction ($L_c \ll L_z$). For ease of calculation, we drop the second term on the right hand side. We thus get for the 1D case

$$E_n = n_x^2 \left(\frac{\hbar^2\pi^2}{2m^*L^2}\right) \tag{2.8b}$$

We can extend this treatment to two and three dimensions

$$\text{2D: } E_n = \left(n_x^2 + n_y^2\right)\left(\frac{\hbar^2\pi^2}{2m^*L^2}\right) \tag{2.9}$$

, and

$$\text{3D: } E_n = \left(n_x^2 + n_y^2 + n_z^2\right)\left(\frac{\hbar^2\pi^2}{2m^*L^2}\right) \tag{2.10}$$

There is an important concept that extends from this, the concept of density of states. Essentially the density of states is the number of states available in the system at a particular energy. It is clear from equations 2.8 - 2.10 that more the number of dimensions, more the allowed number of states available in the system. For an illustration, we derive the density of states for the 2D case.

We start from 2.9 and use the boundary condition, $k_x = \pi n_x/L$ and $k_y = \pi n_y/L$ where L is the dimension of system (L is large compared to a unit cell). Here we consider n_x to be an integer. We then have

$$E_k = \left(\frac{\hbar^2}{2m^*}\right)\left(k_x^2 + k_y^2\right) \tag{2.11}$$

Consider a Fermi surface in two dimensions, i.e. a circle with radius k_F, the fermi wave-vector. Let the fermi energy be E_F. Then,

$$E_F = \frac{\hbar k_F^2}{2m^*} \tag{2.12}$$

Within the fermi circle, each allowed state occupies k-space of area (π/L^2). Considering a total number of states N (i.e. N electrons), we have

$$\pi \times k_F \times k_F = \left(\frac{\pi}{L}\right)^2 \times N \qquad \Rightarrow N = k_F^2 L^2/\pi \tag{2.13}$$

Utilizing equation 2.11, plugging in $k_x^2 + k_y^2 = k^2$ and utilizing equation 2.13 for a general k, we have

$$E_k = \frac{\hbar^2}{2m}\left(\frac{\pi}{L^2}\right)N \tag{2.14}$$

Now, density of states $g(E)$ is defined as

$$g(E) = \frac{dN}{dE} \quad \Rightarrow \quad g(E) = \left(\frac{2m}{\hbar^2}\right)\left(\frac{L^2}{\pi}\right) = \text{constant} \tag{2.15}$$

We can account for the spin of the electron by multiplying right hand side by 2. This form of density of states is quite interesting and implies a constant number of energy levels till all states are filled. As we increase the energy of the system, this goes on till we hit a quantum transition and then there is a sudden jump in the density of states. This is represented as a staircase function in Figure 2.7. Density of states in other dimensions are also illustrated. In the Figure 2.7, density of states is zero until energy > energy bandgap (E_g). For zero dimension structures, optical transitions only occur at certain energy levels (labelled E_1, E_2) and thus density of states is of the form of delta function.

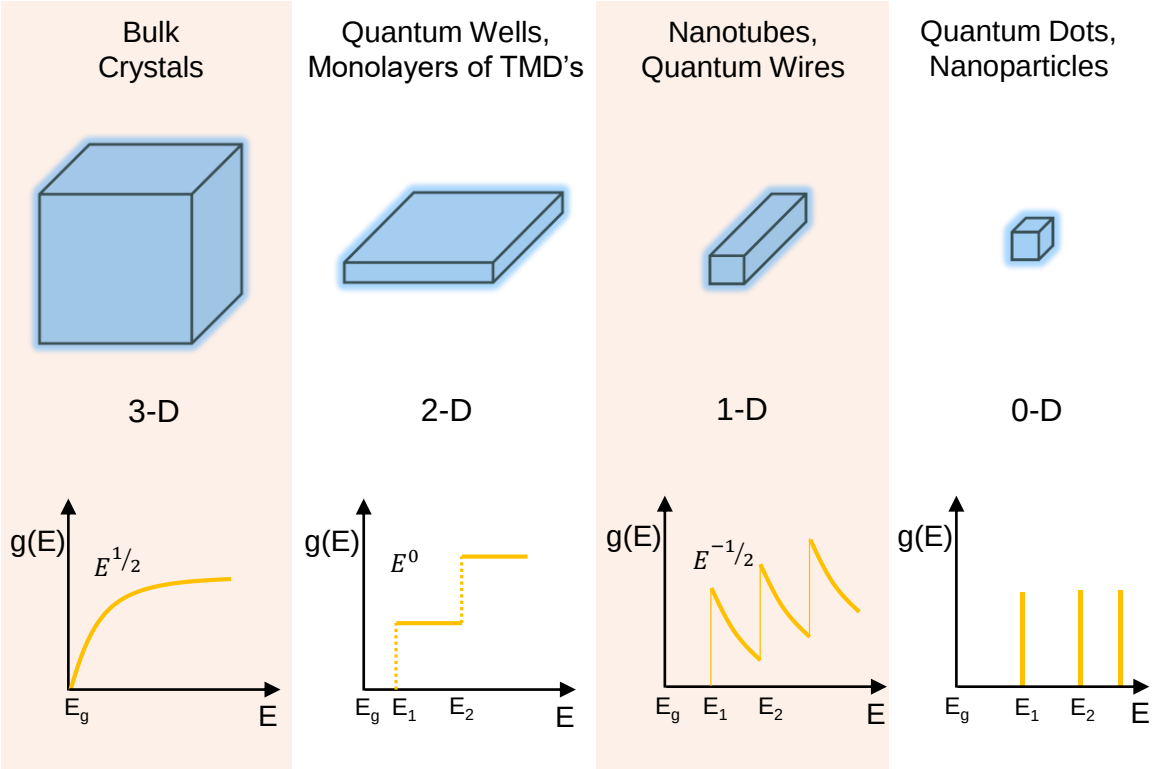

Figure 2.7: Density of states in different dimensions.

But what exactly decides whether an electron is quantum confined or not? How small do we shrink a nanostructure before it starts showing quantum effects? The answer to these questions is ruled by a parameter called the exciton bohr radius (of the particular semiconductor under study). When a spatial dimension of the system is less than the exciton bohr radius, the electron wavefunction is quantum confined in that dimension. For example, bohr radius of silicon and gallium arsenide is ~ 5 nm and ~ 15 nm respectively [112,113]. We discuss these concepts in the next section.

Optical Quasiparticles - Excitons and Trions

Excitons are the fundamental optical excitation in semiconductors. In other words, they are the optical quasiparticles. As we discussed in chapter 1, quasiparticles are essentially simplifications to the full quantum mechanical many-body problem in

semiconductors and other materials. Thus, excitons are just an easy way to think about the coulomb interactions between electrons and holes. We saw in Figure 2.7 that the absorption in a semiconductor occurs for energies $E > E_g$ (bandgap energy). However, after accounting for coulomb interactions between electron and holes, which is purely a quantum mechanical correction, we get energy levels below the bandgap at which absorption can occur. These are accordingly called the excitonic transitions. A mathematical treatment of the exciton wavefunction follows. For a direct band gap material, the exciton wave function can be constructed from a linear combination of electron and hole bloch functions

$$\psi(r_e, r_h) = u_{c,0} u_{v,0} \Phi(r_e, r_h) \tag{2.16a}$$

, where r_e, r_h are the displacement functions of electron and hole respectively, $u_{c,0}$ and $u_{v,0}$ are the atomic part of bloch functions of the conduction and valence band respectively, at the band extremum (zero momentum), $\Phi(r_e, r_h)$ is called the exciton envelope function. The atomic part of bloch functions arises from the atomic orbitals as was discussed earlier in the chapter. The exciton envelope function essentially comes through a sum of states

$$\Phi(r_e, r_h) = \sum_{k_e, k_h} \Phi(k_e, k_h) e^{ik_e \cdot r_e} e^{ik_h \cdot r_h} \tag{2.16b}$$

Thus, the exciton wavefunction described in equation 2.16 consists of an exciton envelope function being modified on the atomic scale by the electron and hole atomic bloch functions. Further, the exciton envelope function obeys the two particle Schrodinger equation

$$\left[-\frac{\hbar^2}{2m_e}\nabla_{\mathrm{e}}^2 - -\frac{\hbar^2}{2m_h}\nabla_{\mathrm{h}}^2 - \frac{e^2}{\epsilon|r_e - r_h|}\right]\Phi = E\Phi \tag{2.17}$$

, where $-\frac{e^2}{\epsilon|r_e - r_h|}$ is the attractive coulomb potential and ϵ is the dielectric constant of the material. We then transform to relative $r(= |r_e - r_h|)$, and center of mass $R\left[= \frac{m_e r_e + m_h r_h}{m_e + m_h}\right]$ coordinates. This can be used to decompose the exciton envelop function into two separable functions in r and R

$$\Phi(R, r) = g(R)\phi(r) \tag{2.18}$$

This separation of variables induces the set of separated Schrodinger equations

$$-\frac{\hbar^2}{2M}\nabla_{\mathrm{R}}^2 g(R) = E_R g(R) \tag{2.19}$$

$$-\left[\frac{\hbar^2}{2m_r}\nabla_{\mathrm{r}}^2 - \frac{e^2}{\epsilon r}\right]\phi(r) = E_r g(r) \tag{2.20}$$

, where $M = m_e + m_h$ is the combined mass and $m_r = \frac{m_e m_h}{m_e + m_h}$ is the reduced mass of the electron-hole pair. Equation 2.19 resembles a free particle kinetic energy equation. Thus, the solution of the center of mass wavefunction $g(R)$, along with the energy values E_R are

$$g(R) = e^{iK_c R} \text{ and } E_R = \frac{\hbar^2 K_c^2}{2M} \tag{2.21}$$

, where $K_c = k_e + k_h$ is the center of mass wave-vector (note that $k_h = -k_v$). $g(R)$ gives the exciton its running wave character.

Equation 2.20 is the Schrodinger equation for the relative motion of electron-hole pair (also referred to as the Wannier equation). It resembles a hydrogen atom like model, with solutions of the form

$$E_r = -\frac{m_r e^4}{2\hbar^2\epsilon^2}\left(\frac{1}{n^2}\right) = -\frac{E_B}{n^2}, \text{ where } E_B = -\frac{m_r e^4}{2\hbar^2\epsilon^2} = -\frac{e^2}{2m_r a_B^2} \quad (2.22)$$

Here, $$a_B = \epsilon\hbar^2/m_r e^2 \quad (2.22b)$$

is the exciton bohr radius and is a powerful tool to decide the size of the nanostructure to induce quantum confinement. The bohr radius seems to be proportional to the background dielectric constant, however the effective mass in the denominator (in equation 2.22b) makes the dependence slightly complicated. The binding energies E_R are useful to quantify interactions between electrons and holes. Tightly bound electron-hole pairs have large binding energies (example- carbon nanotubes, TMD's) and correspondingly small exciton bohr radii. An exciton series is shown as an example for the material cuprous oxide in Figure 2.8 [114]. However, usually such an exciton series is difficult to observe experimentally for most materials due to gradually decreasing relative strengths of transitions [115]. Meanwhile, the function $\phi(r)$ has solutions of the form of atomic orbitals of the hydrogen atom (1s, 2s, 2p etc.), which can be found in a standard quantum mechanics textbook.

Combining equations 2.21 and 2.22, we get the exciton energy expression

$$E_n = E_g + E_r + E_R = E_g - \frac{E_B}{n^2} + \frac{\hbar^2 K_c^2}{2M} \quad (2.23)$$

, and the exciton wavefunction

$$\Psi(r, R) = u_{c,0} u_{v,0} \phi(r) e^{iK_c.R} \tag{2.24}$$

Thus in summary, the exciton wave function consists of four terms. The first two terms characterize the orbital nature of the conduction and valence bands and further, decide which optical transitions will occur. The third term describes the relative motion of electron and hole and decides the binding energy. Finally, the fourth term expresses the translational symmetry of the underlying crystal structure.

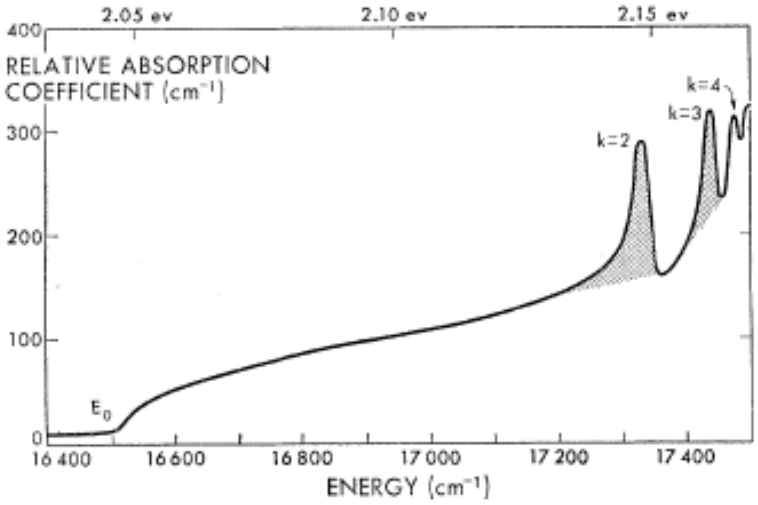

Figure 2.8: Exciton series in Cu_2O with levels represented by k (k=1 is dipole forbidden). Reproduced from [114].

Excitons are also characterized by the strength of the interactions and correspondingly, the size of the exciton bohr radius. For strong e-h interactions, as in ionic crystals or organic molecules, the electron and the hole are tightly bound to each other over length scales of a unit cell and are called Frenkel Excitons (bohr radius ~ 1 – 2 nm) [116,117]. However, in most inorganic semiconductors, the Coulomb interaction is strongly screened due to large dielectric constants (example- ε_r for silicon and gallium arsenide ~ 12). Such weakly bound electron-hole pairs are called Wannier excitons (bohr

radius ~ 5 – 15 nm) [118]. An interesting area of physics is the coupling of the Frenkel and Wannier excitons via hybrid semiconductor structures [119,120]. Such coupled structures are theoretically predicted to exhibit unique features such as splitting of the excitonic spectrum and enhancement of optical non-linearities. Excitons in gallium arsenide quantum wells, as we mentioned, are of the Wannier variety. The binding energies correspondingly are small. On the other hand, in TMD's due to the modified screening (due to the extreme two-dimensionality), the excitons have characteristics in between Frenkel and Wannier excitons. Correspondingly, the binding energies are quite large in TMD's compared to gallium arsenide quantum wells. We will see in chapter 5 how screening can affect quasiparticle dynamics.

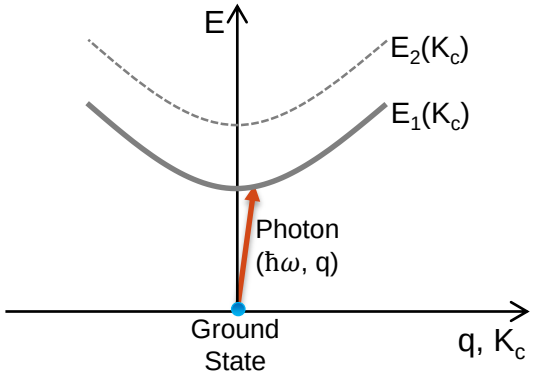

Figure 2.9: Illustration of a photon absorption and creation of exciton. Here, the energy-(exciton center of mass) momentum picture is used.

We have mentioned, while explaining the different parts of the excitonic wave function in equation 2.24, why certain optical transitions are allowed. Let us look into the "selection rules" regarding the optical transitions. A typical optical transition (absorption) is illustrated in Figure 2.9. We draw the combined electron-hole picture (compare to Figure 2.6), where the x-axis represents (center of mass) momentum of the exciton and y-axis represents the energy (as usual). The ground state consists of the crystal ground state

(electron in the valence band, conduction band is empty) and an incident photon (angular frequency ω, momentum $q = \omega/c$). Referring to equation 2.23, the smallest energy gap is $E_g - E_B$, where we have utilized $K_C = 0$ and $n = 1$ (first exciton state). We have also illustrated the second state in the exciton series (E_2). An important property of semiconductors is that the number of free carriers (electrons in conduction band, holes in valence band) are much smaller than the number of atoms. Thus, electrons occupy only a small fraction of conduction band around zone center. Therefore, optical properties of the semiconductor are mostly decided by the dispersion and spectrum around center of B.Z.. Additionally, the parabolic shape of the bands is a consequence of the $\frac{\hbar^2 K_c^2}{2M}$ term.

There are four basic selection rules, the first of which is simply momentum conservation

$$\hbar K_C = \hbar q \tag{2.25}$$

which means the center of mass momentum of exciton equals the momentum of the incoming photon. We note again that the momentum carried by a photon is much smaller compared to crystal momentum ($\sim 1/a$) and hence most transitions occur at $K_C = 0$.

The second rule corresponds to energy conservation

$$E_n(K_C) = \hbar\omega \tag{2.26}$$

i.e. energy of incoming photon must equal the energy of the exciton created. Since most transitions occur at $K_C = 0$, most transitions occur at $E_n = E_g - \frac{E_B}{n^2}$. Thus in an optical absorption experiment, there appear sharp excitonic lines as a result of direct optical transitions.

The third rule concerns angular momentum conservation.

$$\Delta l = \pm 1 \tag{2.27}$$

, and

$$\Delta l = \Delta l_{atomic} + \Delta l_{envelope} = \pm 1 \tag{2.27b}$$

As we mentioned, the ground state consists of a photon and crystal ground state. The photon, in the dipole approximation, carries an angular momentum $l = 1$ (note the dipole approximation is related to the first order interaction of light field with the electron and is of the form $e.r$). Thus the change in angular momentum of the exciton (initial state has zero angular momentum since no exciton exists) should be equal to the angular momentum carried by the incident photon. Note $\Delta l = \pm 1$, since a photon can be right ($l = 1$) or left circularly polarized ($l = -1$). Equation 2.26 is similar to the usual dipole selection rule in atomic spectroscopy. Further, we separate the atomic orbital ($u_{c,0}u_{v,0}$) and exciton envelope contributions and thus state equation 2.27b. As a consequence of equation 2.27b, we have two possibilities

$$\Delta l_{orbital} = \pm 1, \qquad \Delta l_{envelope} = 0 \tag{2.28}$$

and,

$$\Delta l_{orbital} = 0, \mp 2, \qquad \Delta l_{envelope} = \pm 1 \tag{2.29}$$

The optical transitions which follow equation 2.28 are sometimes referred to as dipole allowed first class transitions. For example, a transition can occur between a p-like valence band and an s-like conduction band. Consequently, the exciton envelope function must be s-like. The conduction band being s-like can be thought of as a consequence of an electron being able to move nearly freely in all directions and thus, having a spherically symmetric wavefunction. These first class transitions are especially relevant

in case of common direct bandgap semiconductors like gallium arsenide. On the other hand, transitions that follow equation 2.29 are referred to as second class transitions. These transitions could happen when the valence band is s-like (or d-like) and the conduction band is s-like. Consequently, the exciton envelope wavefunction is p-like. These transitions are usually weaker than the first class transitions with a further consequence being the exciton series starting at n=2 (there is no 1p orbital). An example of second class transitions is cuprous oxide with the exciton series shown in Figure 2.8.

The fourth and final optical selection rule is parity conservation. Parity is defined as

$$\text{positive parity: } \Psi(r) = \Psi(-r) \tag{2.30}$$

$$\text{negative parity: } \Psi(r) = -\Psi(-r) \tag{2.30b}$$

A photon carries negative parity ($(-1)^l = -1$) and the symmetric crystal ground state has a parity of +1. Thus the initial state is negative parity (the parities get multiplied) and thus, the created exciton should also have negative parity. This can be achieved by a combination of parity from the orbital and the envelope part. The first class transition described above, involving s-like valence band (parity = +1), p-like conduction band (parity = -1) and s-like envelope (parity = +1), follows this parity conservation. The angular momentum conservation and parity conservation laws can be slightly difficult to apply when the bands are a combination of different atomic orbitals. It is then useful to compute the complete light interaction integrals (in the dipole approximation) to make a judgement whether the transition is optically allowed [118]. Group theory arguments can also be used to make a similar judgement but these are beyond the scope of this dissertation.

So far we have not explored the effect of doping on the material. In doped semiconductors (accidental or designed), the background electrons can bind with photo-created excitons to form another quasiparticles, trions. Further, the trion energy is usually lower than the exciton due to attractive potential between the extra charge and the oppositely charged part of the exciton. A graphical representation of the trion wavefunction can be seen in Figure 5.1. We will study the relaxation dynamics of an exciton to trion, in detail in chapter 5.

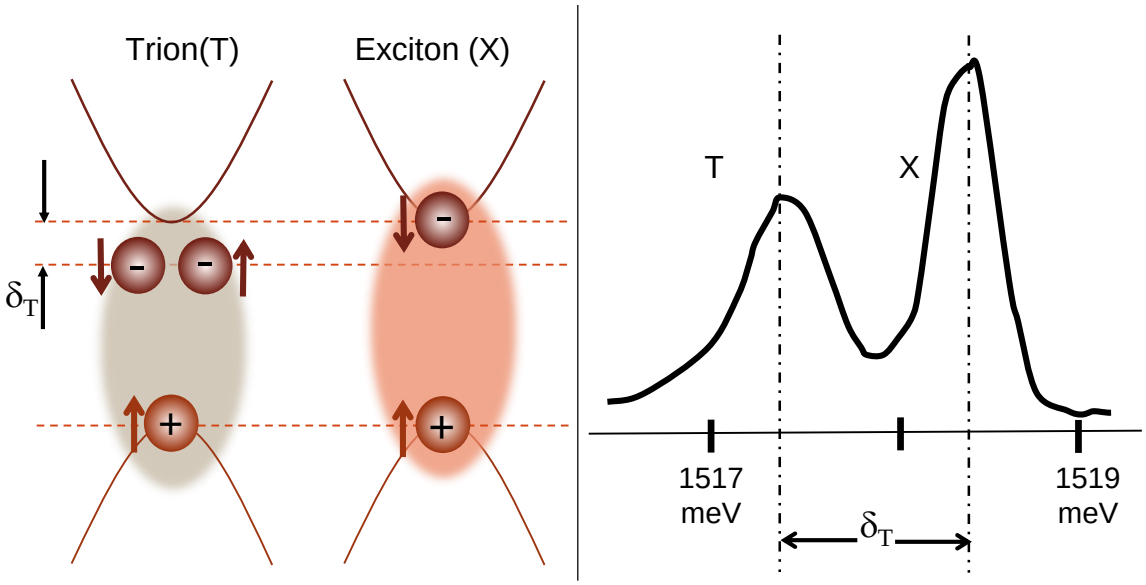

Figure 2.10: Comparison of trion and exciton energy levels. A typical spectrum of GaAs is shown.

The trion can also be resonantly generated rather than relying on the relaxation of the exciton. This trion transition is illustrated in Figure 2.10 where the trion binding energy δ_T (energy difference between exciton and trion) is also shown. δ_T is a measure of the strength of the interaction between electrons in a material, as discussed in chapter 1. As we see in Figure 2.10, the binding energy of a trion in GaAs is ~ 2 meV [73]. This binding energy is quite small and hence trions is GaAs can only be seen at low

temperatures (~ 10 K). However in TMDs', trions have large binding energies (~ 30 meV) and can be seen at room temperature, which makes them technologically relevant [121,122]. Additionally, the trions can either be negatively charged (two electrons and a hole) or positively charged (two holes and an electron). For example, in the Figure 2.10, a negatively charged trion is shown. The spin configuration of a trion is also shown and compared with the exciton. The spin of an exciton consists of an electron (in conduction band) and a hole (in valence band) having opposite spins. The spin configuration of a trion, on the other hand, consists of two electrons (having opposite spin) and a hole. Thus, the spin of the hole is what decides the spin of the photo-excited trion. Further, upon radiative relaxation of the trion, the spin can also be transferred to the background electron gas causing spin polarization [123]. An important note regarding the spin configuration depicted in Figure 2.10 is that we have shown hole spins in the valence band. In other cases and even in this dissertation (in chapter 6 and chapter 7), spins of electrons (instead of holes) in valence band are shown. They can be used interchangeably and the usage will be indicated. Another important note is that the electrons in the trion have a singlet spin configuration. The triplet state (same spin of electrons) is Pauli forbidden, has higher energy, and thus not favorable. Additionally, the spin polarization of trions has shown to be more robust than excitons in a number of material systems [124,125]. Further, the spin polarization of a trion can be transferred to the background electrons upon relaxation of the trion. Thus measuring the spin properties of trions is technologically and fundamentally important. These will be discussed more in chapters 6 and 7.

Another important technological reason behind studying trions is to go beyond diffusive transport. Excitons being neutral quasiparticles, can-not be directed by the application of an in-plane electric field. Exciton transport can be driven by changing the

potential energy landscape through strain or indirect control through applied fields but these are much harder to control [126,127]. However, trions being charged quasiparticles, can simply be driven by the application of an applied field. Thus trions drift along (or opposite) a lateral field. This behavior was seen in GaAs quantum wells at low temperatures and reproduced in Figure 2.11 [128].

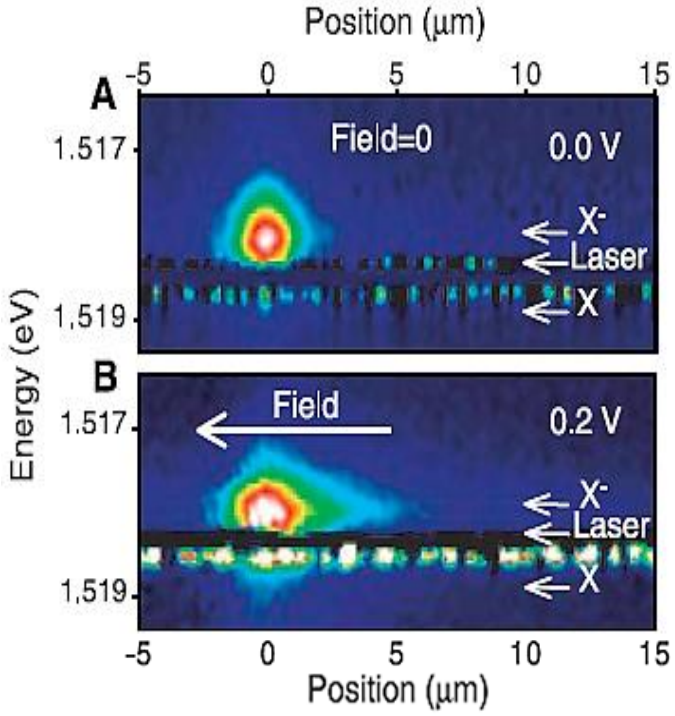

Figure 2.11: Drift control for trions upon application of in-plane electric field.

There is substantial work behind preparing the quantum wells necessary for seeing the transport of trions. The quantum wells studied in ref [128] have modulation doping, i.e. the doped layer is spatially separated from the quantum well. This ensures high mobilities in the quantum well layer even after introducing dopants. The trions thus formed are separate from highly localized trion states in quantum dots or near impurities.

These mobile trions are the focus of chapter 7. Semi-mobile trions are the focus of chapters 4-6. Additionally, what makes trion an interesting engineering and physical problem is that the exciton to trion ratio can be changed by application of a back gate voltage. An example voltage dependent spectrum is shown in Figure 2.12 and is reproduced from ref [129]. The material studied here is a molybdenum diselenide ($MoSe_2$) monolayer which is the focus of chapter 4 and chapter 5.

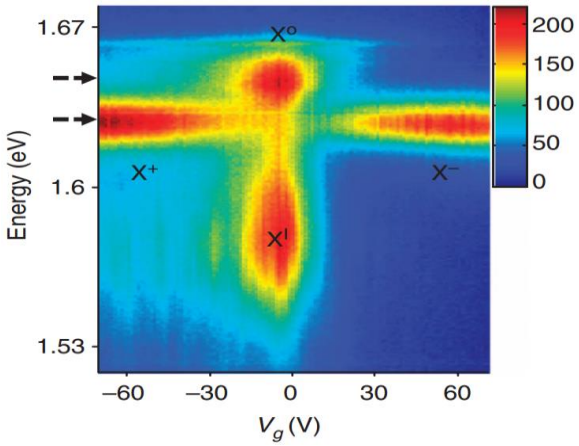

Figure 2.12: Tuning of trion (X- or X+) through application of back gate voltage.

An idea which could be explored is whether the presence of trions can modify exciton transport. The existence of coupling between excitons and trions would imply a combined treatment of the optical and electrical response. Thus there is a possible regime where exciton transport could be extended beyond the diffusive regime via coupling with the trion. This scheme is illustrated in Figure 2.13. An incident light field creates trions and excitons. An applied in-plane electric field induces the transport of trions. If the excitons are coupled to the trions, they may be transported along the electric field, boosting beyond diffusive motion. Coherent coupling, as we mentioned, can enhance

transport and is technologically interesting [39,130]. The nature and magnitude of this coupling behavior is the focus of chapter 4.

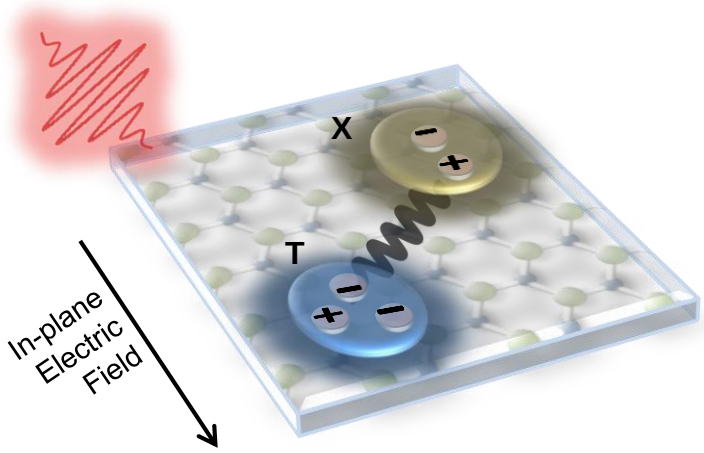

Figure 2.13: Illustration of driving of exciton (X) transport via coupling with trions (T).

QUANTUM WELLS

Quantum wells are the ideal test bed for testing quantum mechanical theories of confinement, tunneling and transport. Basically, quantum wells consist of an active layer surrounded by two confining layers. The active material is a low bandgap material and the confining layers are two higher bandgap materials (usually, the two high index materials are same). The thickness of the active layer is decided by the exciton bohr radius of the material. For example, exciton bohr radius of GaAs is ~ 15 nm, thus the width of the active layer must be smaller or comparable to 15 nm. There are profound changes in the optical response due to confinement in one direction (growth direction) with electrons free to move in the other two directions. In chapter 7, we study quantum wells with width ~ 20 nm, which afford us quantum confinement as well as excellent transport opportunities.

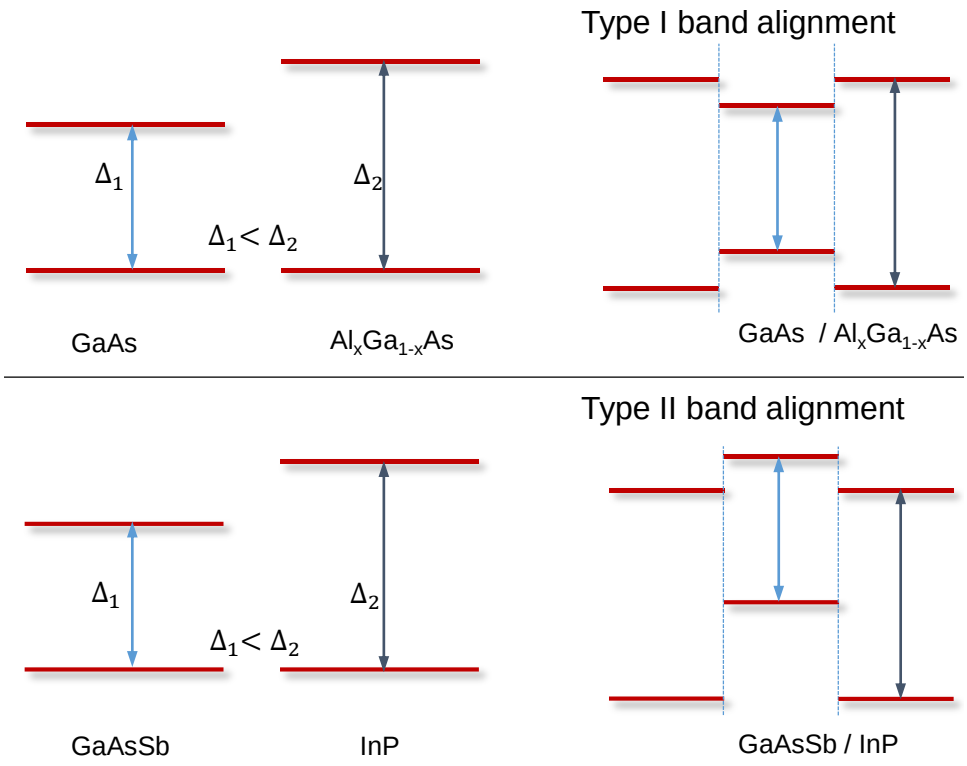

Figure 2.14: Type I and II band alignment in quantum structures.

The possible potential landscapes when the two dissimilar materials are grown sequentially are illustrated in Figure 2.14. The band alignment can be predicted through various empirical models, the prominent being Anderson's rule utilizing principles of electron affinity [118]. Two situations could arise, firstly type I, where the bandgaps lineup such that the electrons and holes reside in the lower bandgap material. Secondly, type II quantum wells arise when the bands are staggered, such that electrons are localized in one material and holes in the other material. This spatial separation has profound consequences for radiative recombination rates. Due to confinement of both electron and hole in the same layer, type I quantum wells are characterized by direct excitonic transitions with enhanced radiative recombination rates (compared to type II quantum wells) and thus are used in light emitting applications. Additionally, type II

quantum wells have larger spin and exciton lifetimes, due to reduced electron-hole spatial overlap, and have applications in infrared lasers [131,132]. Examples of type I band alignment are GaAs/AlGaAs and CdTe/CdMgTe quantum wells while examples of type II band alignment are GaAsSb/InP quantum wells [133]. Interestingly, the behavior of the hetero-structure could switch from type-I to type-II when width of the layers is changed, providing another tuning knob (example GaAs/AlAs and GaSb/GaAs [134,135]). In this dissertation, we focus on type I semiconductors, which are ideal for measuring excitons and trions due to the strong interband transitions.

Quantum wells are grown by a technique called molecular beam epitaxy (MBE). Briefly, MBE utilizes an ultra-high vacuum and slow deposition of materials, consequently epitaxial growth can be achieved. The constituent elements (example gallium and arsenic for gallium arsenide) are kept in separate containers (cells) and only react on the substrate. The growth is continuously monitored through diffraction measurements which ensure a crystalline growth. MBE ensures a high control of the uniformity and low concentration of impurities. Further, this control also provides a way to create structures of varied composition and thicknesses, provided the strain is accounted for. The fabrication technique works best for materials having similar lattice constants, thus strain while deposition is reduced and uniform layers with epitaxial growth is achieved. On the other hand, MBE does suffer from monolayer fluctuations which are especially an issue in narrow quantum wells. The MBE technique is also quite expensive and not suitable for high volume production (compared with solution processing or chemical vapor deposition). However, all things considered, MBE is the state of art in fabrication techniques, and used to grow the quantum wells we study in chapter 7.

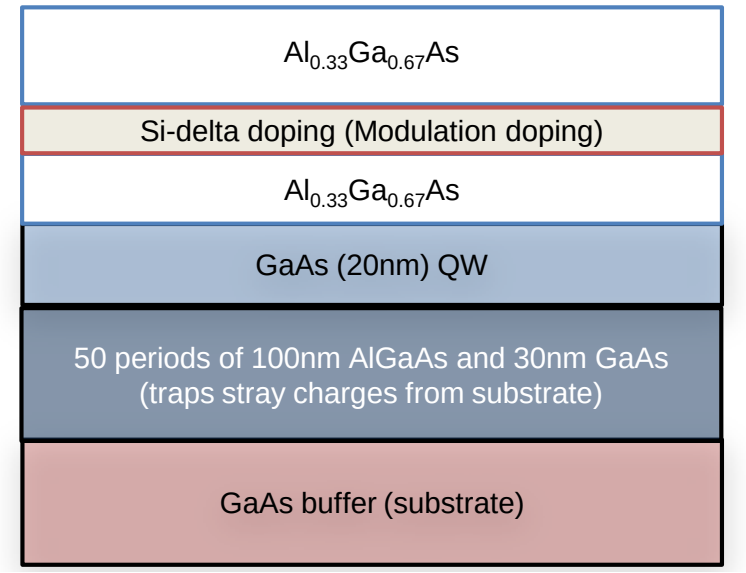

Figure 2.15: Quantum well sample with modulation doping.

The extraordinary control provided by MBE ensures quantum effects can be measured (with reduced effects from impurities) in quantum wells. Interesting phenomena relating to trion and exciton transitions can be seen in quantum wells through modulation doping, a technique in which a layer containing dopant atoms is grown. As we have discussed, this dopant layer is located away from the active quantum well layer, preserving high electron mobilities in the active quantum well layer and providing electrical tuning between excitons and trions. A typical modulation doped quantum well is shown in Figure 2.15, and is the focus of chapter 7. In the figure, we show a GaAs/$Al_xGa_{1-x}As$ quantum well ('x' controls the composition of aluminum in the barrier layer and consequently the bandgap and confinement). The modulation doped layer consists of an AlGaAs layer, doped with silicon (with controllable dopant concentration), at a suitable distance from the quantum well. The function of other layers is mentioned in the figure, for example the thick layer of GaAs acts as the substrate for epitaxial growth. Using a back-gate (vertical) voltage, electrons (or holes) can be induced to move into the

quantum well layer (from the doped layer) and hence, tuning of optical transitions is possible.

A natural consequence of electron hole confinement are the enhanced radiative rates (compared to bulk) due to increased overlap of electron and hole wavefunctions. Further, quantum confined structures have much different band structure compared to bulk crystals. The comparison is exemplified by GaAs quantum wells where the degeneracy between the heavy hole and light hole bands (sub-bands in the valence band) is lifted. The band structure is shown for GaAs bulk and quantum wells in Figure 2.16 (reproduced from ref [136,137] and ref [138]). Note that bulk GaAs has direct band at the zero momentum point, Γ, and the band gap is around 1.4 eV. For a quantum well, the nature of the bandgap does not change and GaAs still remains a direct bandgap material. However, the light-hole heavy-hole degeneracy is broken, as can be seen in the difference in energy between LH1 and HH1 in the Figure 2.16 (magnified picture of valence band in quantum well). In bulk GaAs, LH1 and HH1 are degenerate. This has consequences for hole spin polarization, wherein hole spin lifetimes are enhanced in quantum wells compared to bulk. In bulk GaAs, hole spins relax in time scales ~ 100 fs whereas in quantum wells, the lifetime is enhanced to atleast ~ 5 ps [81,139,140]. Thus the interband spin flip-flop is reduced in quantum wells. Interestingly, the trend is opposite for electrons, and electron spin lifetimes are shorter due to opening of several scattering channels [80]. Further complications arise due to importance of exciton spin relaxation mechanisms in quantum wells including exchange interactions and momentum dependent relaxation [80]. We consider these mechanisms and measure spin lifetimes in chapter 7.

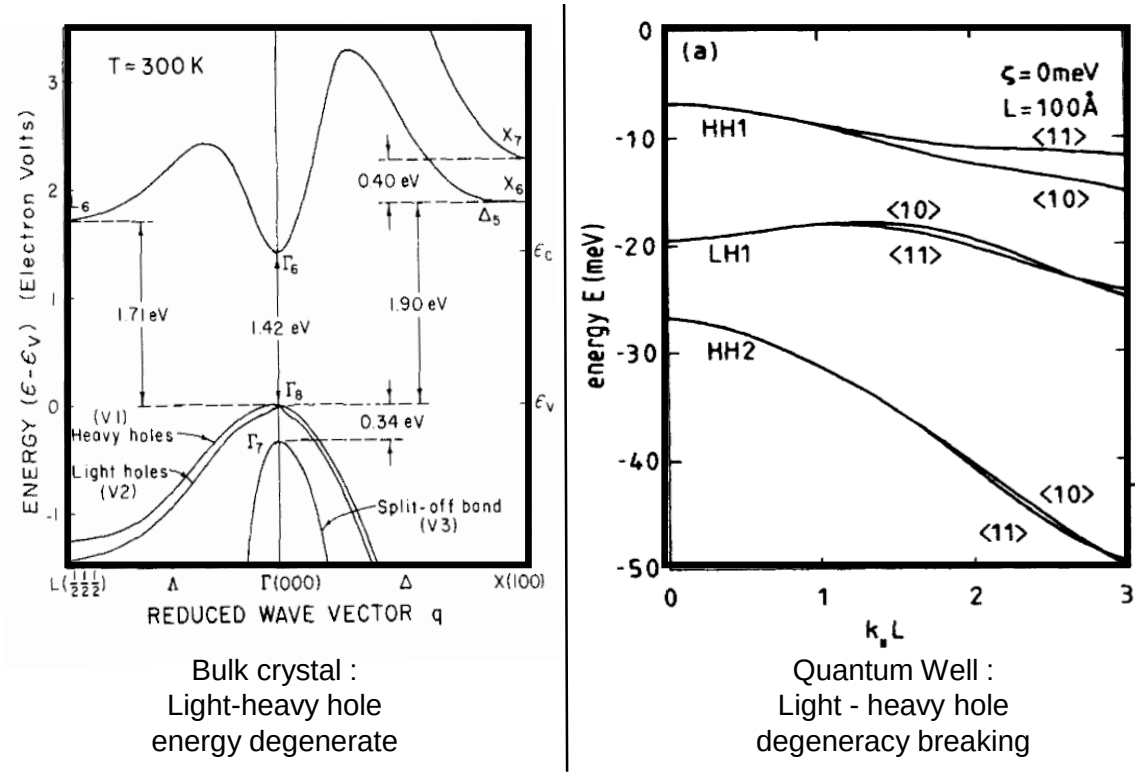

Bulk crystal :
Light-heavy hole
energy degenerate

Quantum Well :
Light - heavy hole
degeneracy breaking

Figure 2.16: Comparison of energy band diagrams for bulk (full band) and quantum well (only valence band shown). Note the different energy scales for the two graphs.

Another important note is the different effective masses for electron and hole in quantum wells. Effective mass is defined as $m^* = \frac{\hbar^2}{d^2E/dk^2}$ and is useful for treating electrons and holes as free particles, with a changed mass- the effective mass. This simplifies the mathematically rigorous treatment of crystal periodic potential and makes the calculation of material response to applied fields (electric and magnetic) straightforward. The different curvature of the conduction and valence bands in Figure 2.16 illustrates different effective masses for electrons and holes. This leads to different binding energies for positive and negatively charged trions and further, different response to an applied magnetic field [140-144]. We will discuss the effect of an applied magnetic field in the context of spin polarization, in chapter 7.

TRANSITION METAL DICHALCOGENIDES

We discussed TMDs' in chapter 1 in the context of a need to study flexible electronics and gave a small flavor of the wonderful properties they have. TMDs' consist of a transitional metal atom (tungsten, molybdenum) and two atoms of a chalcogen (sulphur, selenium, and tellurium) arranged in a crystal structure. We illustrate the crystal structure of a monolayer of $MoSe_2$ in Figure 2.17 as an example. Most TMDs' can exist in two phases- 2H and 3R, which have different crystal structure and vastly different properties including different binding energies for excitonic transitions [145,146]. Figure 2.17 shows the 2H and 3R structure. The 2H structure consists of a unit cell composed of a bilayer and is inversion symmetric upon 180^o rotation of the layers. 2H is more commonly found, being thermodynamically favorable. 3R structure on the other hand, consists of a unit cell composed of a trilayer and is not inversion symmetric. This has profound consequences on the symmetry dependent properties, especially spin polarization. For example, in 2H geometry, a monolayer has spin polarization due to broken inversion symmetry, while a bilayer restores this inversion symmetry resulting in zero spin polarization. However, in the 3R structure, due to lack of inversion symmetry, finite spin polarization exists for all thicknesses. This has applications in chiral light emitting diodes. In comparison with inversion-symmetric graphene, TMD's thus offer a tuning knob of spin polarization. In this dissertation, we concentrate on monolayers with 2H structure since these are more abundant than 3R. Further, the bilayer of a 2H structure affords the opportunity to control the spin polarization via a vertical applied field and breaking the inversion symmetry [146].

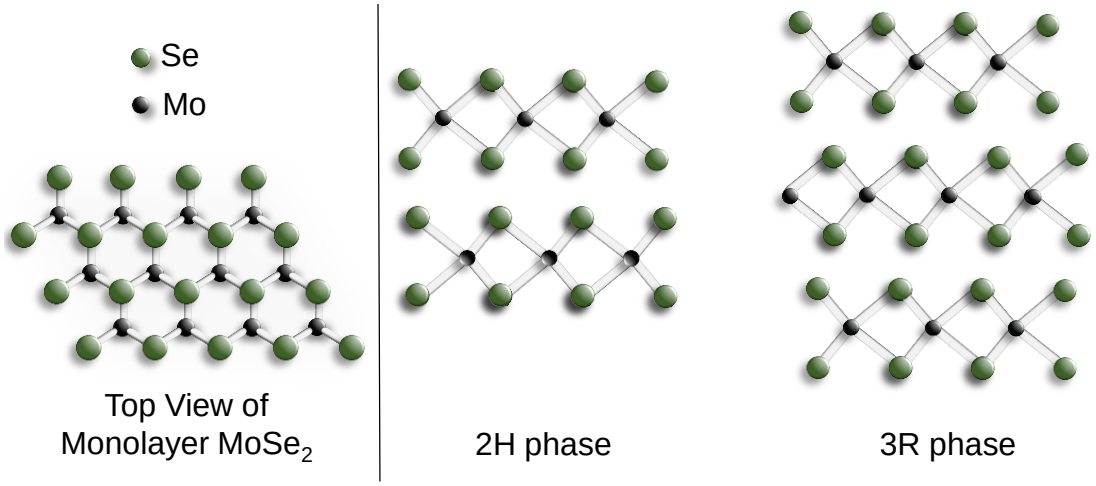

Figure 2.17- Side view of unit cell of 2H and 3R phase. Top view of a monolayer is also shown on the left side.

We have touched upon the difference in spin polarization between monolayers and bilayers of the 2H phase. This is however, not the only reason why monolayers are the basis of our study. We mentioned in chapter 1 that when TMDs' are thinned down to monolayers, they undergo a bandgap change from direct to indirect. The first measurements involved measuring thickness dependent photoluminescence (PL) [85,86]. The key observations, reproduced in Figure 2.18a, showed a large increase in PL intensity as the number of the layers was reduced, from a bulk crystal to a single layer [86]. The observations were explained through first principle calculations, reproduced in Figure 2.18b, demonstrated an evolution of bandgap towards direct gap at the K point [85]. Later, these observations were confirmed using ARPES and scanning electron microscopy [87,88].

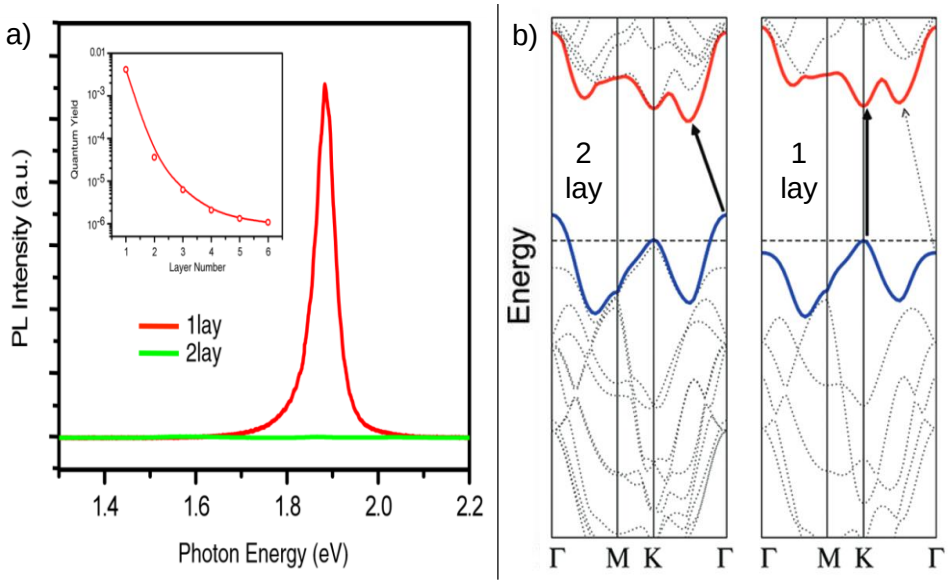

Figure 2.18: a) Thickness dependent PL b) First principle calculations showing an indirect to direct bandgap transition from bilayer to monolayer.

The thickness dependent bandgap transition (from indirect to direct) was interesting for two reasons- firstly, the large PL indicates increasing quantum yield which promised light emitting applications. The quantum yield, however, is quite poor even for the monolayer and is of the order of ~ 1%. There is extensive ongoing research in increasing the quantum yield of these materials and surface chemistry might point the way [147]. The second reason for huge interest in these materials is the location of the direct gap in the momentum space and the consequences in spin-valley coupling. As mentioned, the direct gap is at the K point, thus at a finite momentum, compared to the zero momentum Γ (gamma) point in GaAs. In figure 2.19a, we show the Brillouin zone (B.Z.) which is a hexagon with three-fold symmetric valleys (K'=-K) [93,108,109]. The valleys (K and K') are energetically degenerate but have opposite spins. Thus, a realization of spin-valley coupling is possible which provides a tuning knob in the

manipulation of the dynamics of these materials [94]. This is not possible with GaAs which has spin and energy degenerate valleys due to the direct gap at Γ point.

Further in TMD monolayers, within each valley, the spin split off band (the higher energy band with the opposite spin, located in the valence band) is ~ 150 meV away. In GaAs, on the other hand, the spin-split band (light hole) is only 5 - 10 meV away. Thus, hole spin scattering in TMDs' is strongly suppressed. Consequently, there are two excitons, 'A' (lower energy) and 'B' (higher energy), usually seen in the luminescence spectrum of a TMD monolayer. These excitons are a result of spin-split valence band and spin-degenerate conduction band. 'A' exciton is of the form $\uparrow\rangle_{K,VB_1}\uparrow\rangle_{K,CB}$ while 'B' exciton is of the form $\downarrow\rangle_{K,VB_2}\downarrow\rangle_{K,CB}$, (where $VB_1 \rightarrow CB$ is the lowest energy exciton transition; VB is valence band, CB is conduction band). Therefore, high spin polarization is achievable even with non-resonant excitation. An exemplary demonstration of this spin-valley coupling property in TMDs' is shown in Figure 2.19b (reproduced from ref [109]). A monolayer of MoS_2 is excited with circularly polarized laser ($\sigma-$) and the emission is (almost) completely the same circular polarization. Another interesting property is the presence of valley coherence, i.e. the valleys (K and K') were shown to be coherently coupled, this phenomena being unique to TMDs' [148]. The spin-valley coupling has given rise to the field of valleytronics demonstrating valley hall effect, chiral light emitting diodes and promises further applications in spin as an information carrier [100,101,149].

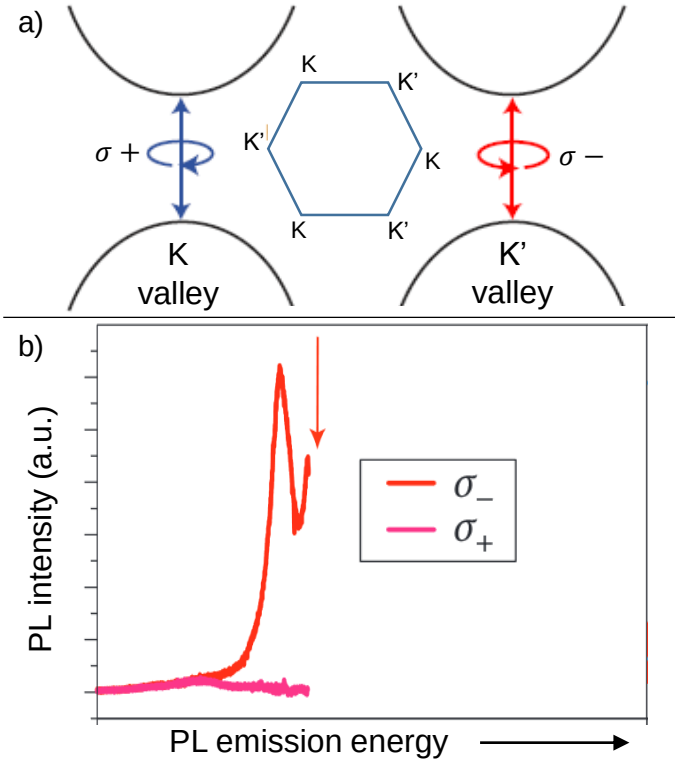

Figure 2.19: a) Illustration of spin-valley coupling and B.Z. b) Circularly polarized PL showing spin-valley coupling.

Another physically important aspect is the excitonic nature of these optical transitions. As we discussed before, the bulk crystals had been shown to have strong excitonic transitions [65,89]. However, the strength of excitonic transitions were enhanced in monolayers compared to bulk, due to the extreme confinement of electrons and hole in one dimension. Additionally, due to reduced screening in these materials, the binding energies of excitonic quasiparticles (excitons and trions) is much enhanced compared to GaAs and quantum wells. An illustration of the excitonic character of the luminescence is shown in Figure 2.20. In Figure 2.20a, a monolayer of MoS_2 was studied (at temperature = 14 K) and the PL spectrum presented (reproduced from ref [109]). Both 'A' and 'B' excitons are seen in the spectrum. In Figure 2.20b, a monolayer of $MoSe_2$

was studied at (at 30 K) demonstrating spectrally sharp and well separated exciton and trion peaks (reproduced from ref [129]). The large trion binding energy ~ 30 meV, can also be seen. Excitons and trions in these materials have been observed even up to room temperature, as we have mentioned earlier [121]. These large binding energies point to strong electronic interactions in these materials making them an interesting testbed for studying quantum effects and technological applications even at room temperature. We focus on the 'A' exciton and the associated trion in this dissertation, since they are the primary optical transitions in TMDs'. Additionally, highly localized (impurities, edges of samples) quantum emitter states were also seen in these materials recently. These quantum emitter states are interesting for applications as single photon sources but are beyond the scope of this dissertation [150-152].

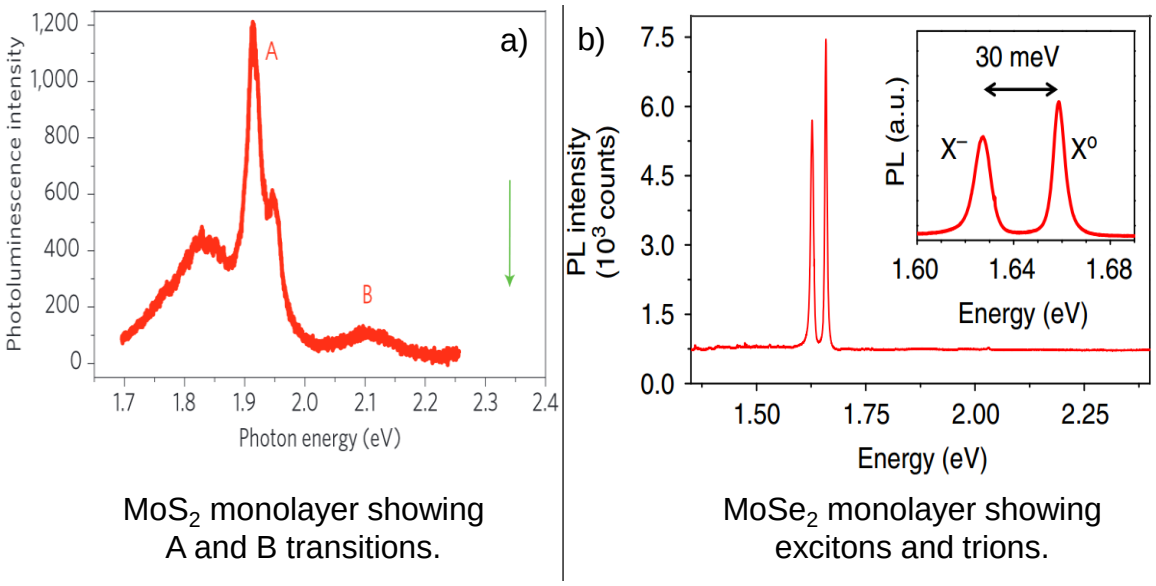

Figure 2.20: a) PL of MoS_2 monolayer b) PL of $MoSe_2$ monolayer

For these emerging systems, controlling the quality of materials is critical. Most of the spectra presented till now has been on mechanically exfoliated samples. Briefly,

tape is stuck on bulk crystals, peeled off and then deposited on the substrate of choice. The layers deposited vary from a few layers to a monolayer. This is a highly probabilistic process with the probability of finding a monolayer being quite low. There are a number of studies researching increasing the probability of a monolayer exfoliation, however these are still not scalable [153,154]. Scalability comes with solution based or gas based fabrication [155,156]. Chemical vapor deposition (CVD) has been extensively used to create high quality semiconductors, however for TMDs', these processes are still under intense research [157,158]. Mechanically exfoliated monolayers are highly crystalline and usually have low impurities, but are small in size (~ 5 μm). On the other hand, CVD fabricated TMDs' monolayers (using current technologies) usually suffer from high dopant densities and grain boundaries, but can be made larger. In Figure 2.21, we have shown a few examples of exfoliated and CVD grown samples [82,159-161]. The scale bars (5 μm vs 50 μm) give an idea of the size of typical mechanically exfoliated samples compared with CVD grown samples. However, due to superior optical and crystalline quality of exfoliated samples, they will be the focus of this dissertation.

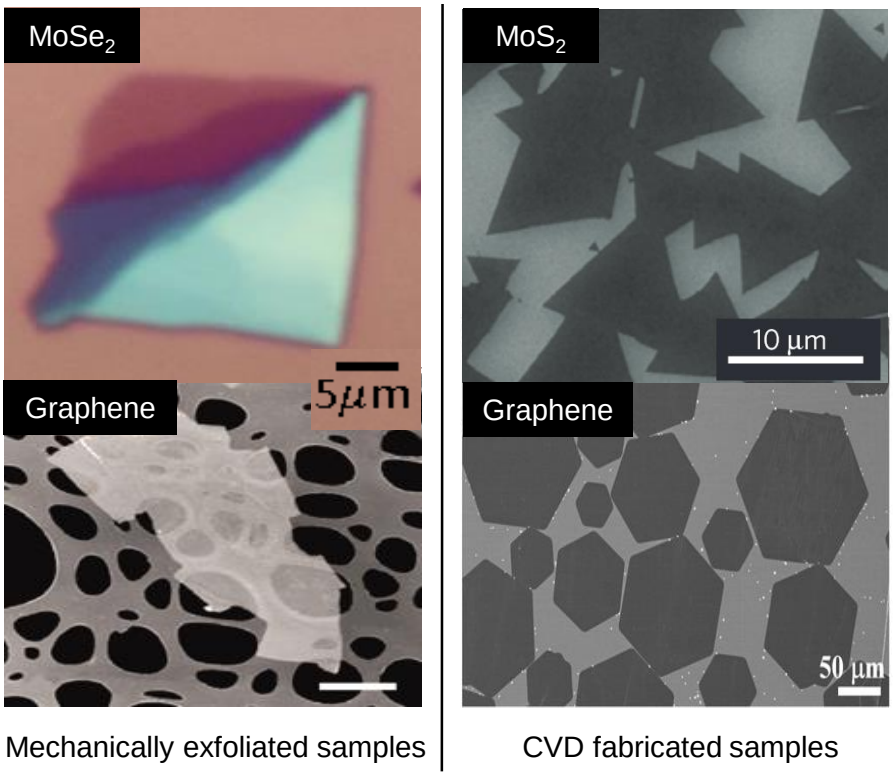

Figure 2.21: Comparison of mechanically exfoliated and CVD grown samples.

Further, the number of layers can be identified using optical contrast, with the monolayer appearing as slightly darker compared to the substrate, and the contrast increasing for increasing layer thickness [162,163]. The layer number can be confirmed with Raman spectroscopy, atomic force microscopy (AFM) and photoluminescence [164,165]. Since the thickness of a single layer is only ~ 0.7 nm, AFM is not usually the tool of choice. Mostly, Raman spectroscopy and PL are used to confirm the number of layers, after preliminary identification by optical microscopy. Raman spectroscopy is sensitive to in-plane and out-of-plane lattice vibrations, and thus is a sensitive tool to determine the number of layers [166,167]. PL, as we have discussed, increases substantially as the number of layers is decreased, as thus is also a sensitive tool to distinguish between few layer samples and monolayers.

A monolayer is highly environment sensitive, and thus care must be taken against exposure to water vapor and chemicals [168]. Any adsorbates on the monolayer can substantially affect the photo-response. Further, the choice of substrate is also important since it affects the screening and the dielectric environment [169]. We chose silicon oxide/silicon as a substrate (chapter 4 and chapter 5) for compatibility with CMOS processing. However, these necessitate reflection geometry. We chose optically transparent sapphire as a substrate, in chapter 6, for use in transmission geometry and a cleaner analysis of complex lineshapes in the optical spectrum. In the next chapter, we take a look at the different experimental techniques used to measure the dynamics and spectral response of these material systems.

NON LINEAR PHENOMENA

Nonlinear phenomena are optical effects arising due to modification of properties of matter due to light. More specifically, they are a class of phenomena going beyond the linear regime, in light matter interactions. All nonlinear phenomena are made possible only at high intensities (though still orders of magnitude lower than ionization strength). To be exact, the importance of nonlinear phenomena increases at higher light intensities, which makes them observable. In nature, that is the primary reason why most light-matter interactions are linear. It is with the advent of laser technology that we can now observe and control nonlinear optical effects. Pulsed laser systems afford high intensities and thus are primarily used for measuring nonlinear phenomena.

The first study of nonlinear optics involved second harmonic generation using an intense red laser beam focused on a quartz crystal [44]. The generated second harmonic light was very weak due to non-optimized phase matching conditions and crystal geometry [170]. However, technologies concerning both the nonlinear light generating

crystal and the driving laser have progressed rapidly [171]. Both of these in turn, have improved the other. As a result, we now have high power table top pulsed laser sources which have eased the study of nonlinear phenomena. Exotic phenomena exemplified by atto-second pulse generation have also been observed with intense laser pulses [45]. Nonlinear phenomena have applications in optical switching and optical logic gates due to the light induced ultrafast changes in the material response.

A mathematical treatment of the response of matter to light is in order. In the linear regime, upon incidence of an optical field $\tilde{E}$, a polarization $\widetilde{P}$ is generated

$$\widetilde{P} = \epsilon_0 \chi^{(1)} \tilde{E} \tag{2.31}$$

where $\chi^{(1)}$ is the linear susceptibility. Extending this to arbitrary orders in the incident field

$$\widetilde{P} = \epsilon_0 \left[\chi^{(1)} \tilde{E} + \chi^{(2)} \tilde{E}^2 + \chi^{(3)} \tilde{E}^3 + \cdots \right] \tag{2.32}$$

where $\chi^{(2)}$ and $\chi^{(3)}$ are the second and third order nonlinear susceptibilities. Generally, the susceptibilities are tensors rather than scalars. For example, $\chi^{(3)}$ is a fourth rank tensor with $3^4 = 81$ elements. Using symmetry constraints (of the crystal), the number of unique and independent elements can be reduced. For example, in an isotropic crystal, there are only 21 non-zero elements, out of which only three are independent.

The second order susceptibility, $\chi^{(2)}$ gives rise to phenomena like second harmonic generation, two-photon absorption, sum frequency generation and difference frequency generation. These phenomena are illustrated in Figure 2.22. The dashed lines represent the virtual levels whereas solid lines represent the ground state and the excited

state respectively. The second order nonlinear phenomena are useful for applications in optical parametric oscillators and high-resolution optical microscopy. Interestingly, for a centro-symmetric crystal, the second order susceptibility vanishes. However, for a centro-symmetric crystal, the surface breaks the inversion symmetry giving rise to a SHG signal. This signal is a sensitive tool to measure phenomenon on the surface [172,173]. Yet, as we mentioned, $\chi^{(2)}$ is not a general optical process and is not uniformly relevant to all material systems.

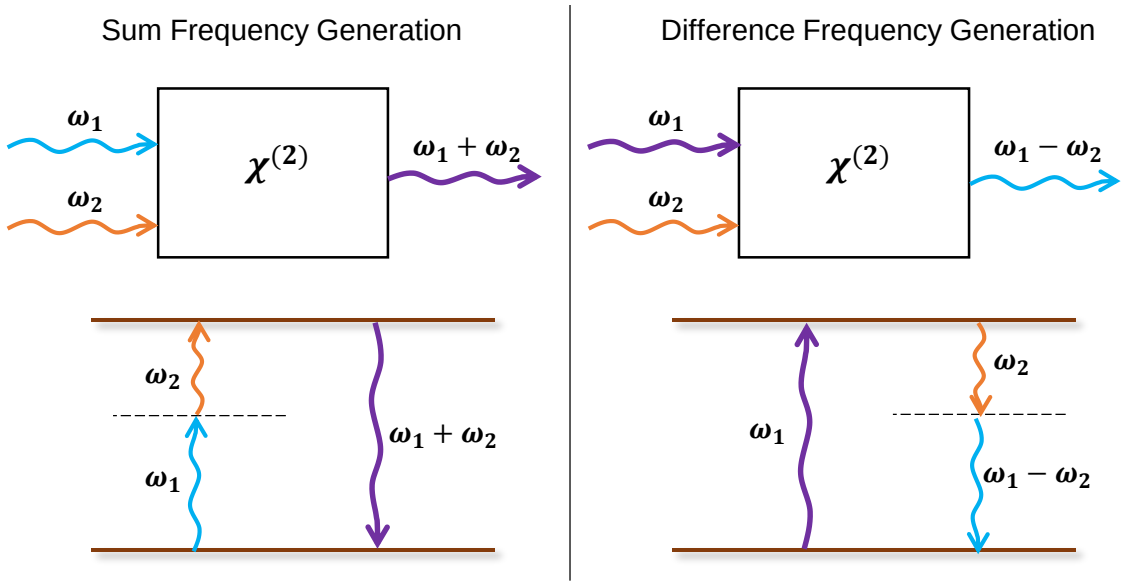

Figure 2.22: Schematic of sum and difference frequency generation processes through a $\chi^{(2)}$ nonlinear process.

$\chi^{(3)}$ on the other hand, is non-zero for all material systems and geometries. This makes the study of $\chi^{(3)}$ versatile, thus leading to measurement techniques exemplified by four wave mixing, pump-probe and third harmonic generation. Additionally, the third order non-linear process offers much flexibility in detection, where the signal field can be designed to be sent along a particular direction where background signals are minimum. This is exemplified by four wave mixing processes, where the signal field is generated in

a direction separate from the incident fields. The directions are decided by energy and momentum conservation principles [170,174]. Further, there are possibilities to increase signal-to-noise ratio through homodyning of signal with probe fields, as in pump-probe experiments. We illustrate third harmonic generation in Figure 2.23 where an incident photon is converted into a photon with three times the energy. Secondly, when three independent optical fields are incident on a $\chi^{(3)}$ material, the resulting optical field could have 44 different frequency components. These arise from a combination of the three frequencies, where they can be taken as positive or negative (complex conjugate) as well. Shortly the output frequency is of the form

$$\omega_4 = (\pm a\omega_1 \pm b\omega_2 \pm c\omega_3), \text{ where, } a, b, c \in (0,1,2) \text{ and } |a| + |b| + |c| = 3 \qquad (2.33)$$

Additionally, the three fundamental frequencies ($\omega_1, \omega_2, \omega_3$) are also emitted. Different frequency components can be generated in different directions according to momentum conservation rules and can be studied separately. The parametric frequency generation refers to the process where the initial and final states are the same and population is removed from the ground states for only brief periods of time (stays in virtual level). Importantly, there are also non-parametric processes which involve population transfer to real levels, which can be measured through pump-probe processes and four-wave mixing.

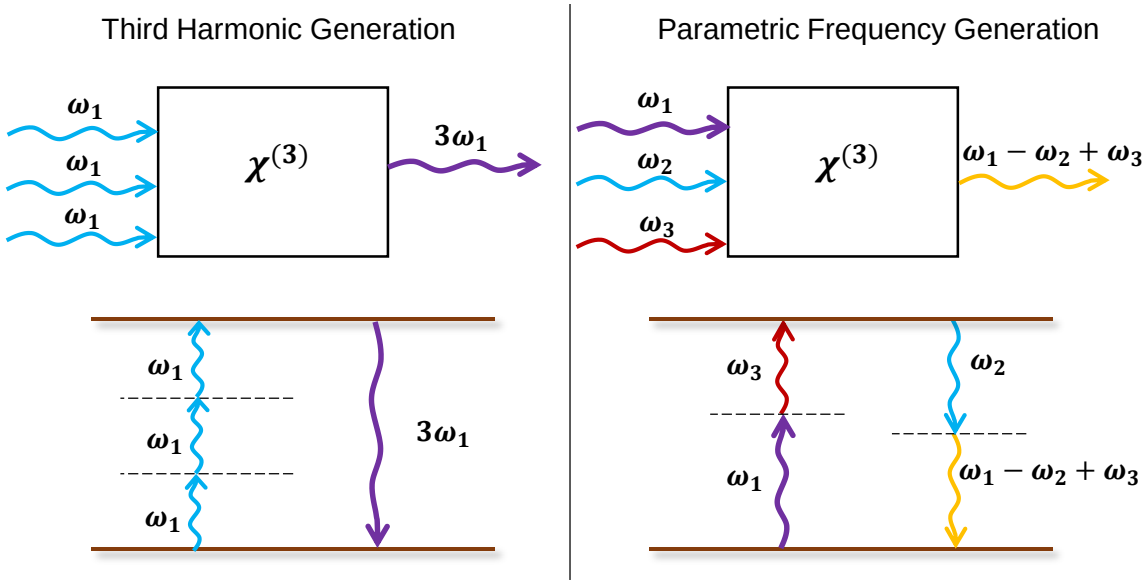

Figure 2.23: Schematic of frequency generation processes through a $\chi^{(3)}$ nonlinear process.

The frequency dependence of the nonlinear susceptibility has not been discussed yet. So far, we have assumed a uniform nonlinear susceptibility for all frequencies. For real physical systems, this is obviously not true. At optical resonances of the material under study, the nonlinear response increases due to substantial changes in nonlinear susceptibilities, $\chi^{(2)}$ and $\chi^{(3)}$ [175-177]. The primary reason is the increase in absorption and creation of real photo-excited carriers, which influence the nonlinear response [178]. An illustration of the change in $\chi^{(3)}$ is shown in Figure 2.24 [170]. The imaginary and real parts are connected through Kramers-Kronig relationship. Thus, at the excitonic transitions, the nonlinear response of semiconductors increases. We exploit this fact to measure the absorption resonances and their dynamics in our experiments through pump-probe spectroscopy.

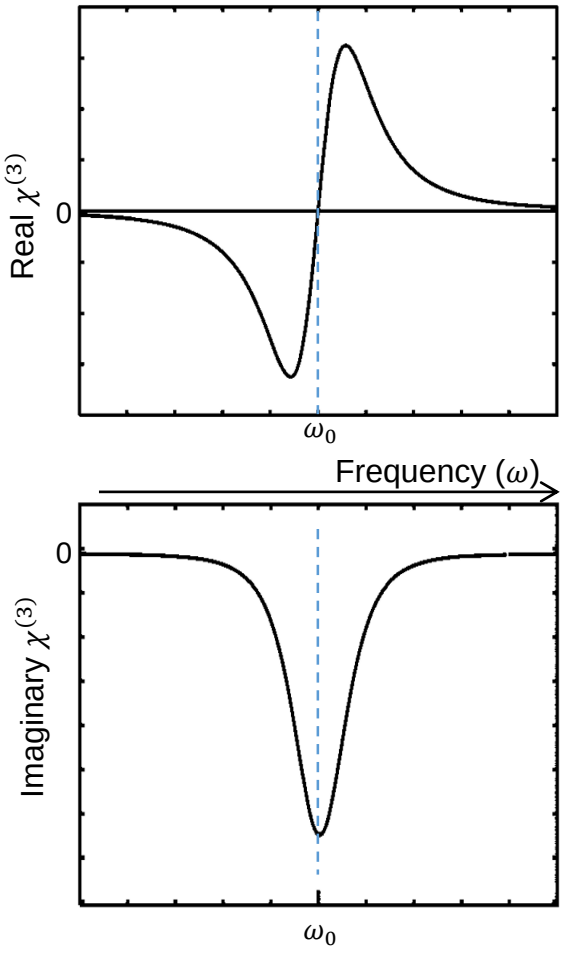

Figure 2.24: Illustration of enhancement of $\chi^{(3)}$ across a resonance.

Chapter 3: Experimental setup and Techniques

We have thus far discussed the motivation and physics behind our research in the general field of light matter interaction. The ideas behind choosing certain experimental techniques and the details need explanation. The technical aspects of the experiment as we will see, are optimized to make the physics successful.

PUMP-PROBE SETUP

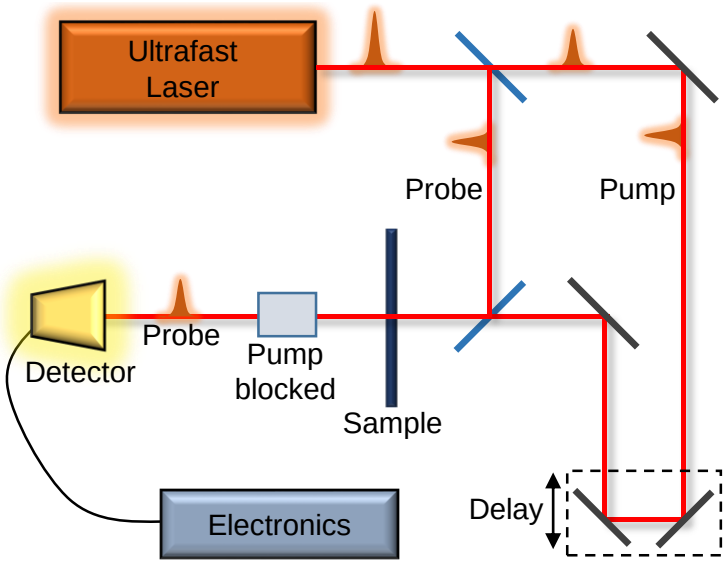

Figure 3.1: Basic Pump-probe setup schematic.

Pump-probe (PP) is the most common form of ultrafast optical spectroscopy. It is also very general and certain flavors of pump-probe spectroscopy are more popular than others. An illustration of the basic form of PP spectroscopy is shown in Figure 3.1. In its simplest form, i.e. degenerate PP spectroscopy, the output pulse train of an ultrafast laser is split into two optical paths. The path lengths can be changed with respect to each other, using a controllable mechanical delay stage, and the two pulses are incident on the

material under investigation. The first pulse, called the pump pulse (excitation pulse) excites the sample (or generally induces some change in the material). The second pulse, called the probe pulse, is then incident on the sample. The relative arrival of the pump pulse, with respect to the probe pulse (on the sample), can be tuned via the delay stage. Changes in the probe (absorption, spectral changes) are measured as a function of the position of the delay stage, thus measuring the dynamics of the material. Importantly, this scheme only works if the material has a nonlinearity. If the material is linear, then the pump can induce no change in the probe absorption.

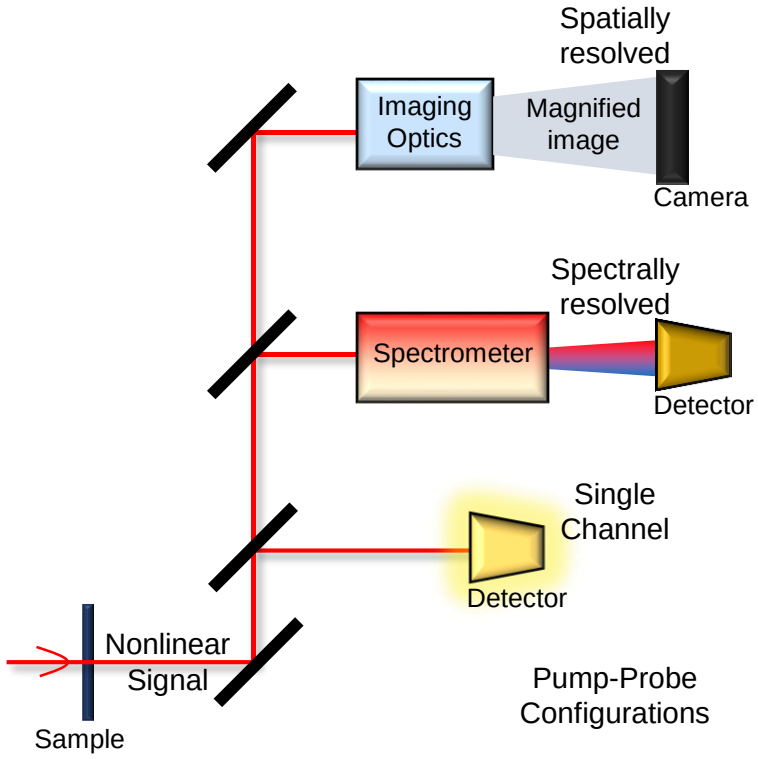

Figure 3.2: Different types of pump-probe measurement techniques.

Pump-probe (PP) can be configured to measure different physical phenomena. We illustrate a few different configurations of pump-probe in Figure 3.2. Briefly, the

nonlinear signal generated by the sample can be detected in a number of ways. In PP measurements, the nonlinear signal is carried by the probe. The probe can be directly sent to a single channel detector. Note that the pump is blocked from going into the detector through spectral, polarization or spatial filtering. The single channel detection configuration is useful for degenerate PP spectroscopy as well as single wavelength probing, and is referred to as spectrally integrated detection. The second technique utilizes a spectrometer which splits the probe into its constituent wavelengths, which can subsequently be detected by a wide bandwidth detector or a charge coupled device (CCD). This spectrally resolved technique can be used to measure and differentiate between different optical transitions of the semiconductor. The third technique utilizes imaging optics (a combination of lenses) to spatially resolve the image. Thus the sample can be imaged on a camera or, on a detector employing a pinhole. Spatially resolved PP can be used to measure the dynamics of electronic transport in a semiconductor. Another iteration of spatially resolved PP utilizes spatial scanning of the pump spot across the probe, while both (pump and probe) are incident on the sample [179]. Additionally, there are many more PP configurations including Kerr rotation and thermal transport. Kerr rotation PP spectroscopy is the technique of choice for measuring spin and is the focus of chapter 7. Another configuration, involving circularly polarized pump and probe pulses with a combination of spectral filtering is used to measure spin dynamics in chapter 6.

The pump-probe signal is the difference in intensity of probe transmitted (or reflected) through the sample, when the pump is on and when it is off. The PP signal is usually depicted as a differential signal. Specifically, the differential PP signal is

$$\frac{dT}{T_0} = \frac{T - T_0}{T_0} \tag{3.1}$$

, where $T(T_0)$ is the probe intensity detected when pump is on (off). The probe intensity signal is detected through a single channel detector, and sent to a lockin amplifier for higher sensitivity. We discuss details of the lockin technique later in this chapter. The delay between the pump and probe can be changed, through a mechanical delay stage, to measure the dynamics. Thus even a slow detector can be used for this technique. The time resolution is limited mostly by the temporal widths of the pump and probe pulses. Further, the pulse width affects the intensity of pump and probe pulses.

Pump-probe is a nonlinear technique and is thus intensity dependent. For agreement with equation 3.1 and meaningful scaling with pump and probe powers, it is important for the experiment to be performed in the $\chi^{(3)}$ regime. Consider the basic PP configuration, the pump pulse is incident on the sample, exciting a population of carriers. The density matrix formalism (described in Appendix A) indicates that the pump field acts twice to create this population of excited carriers. The probe pulse is then incident on the sample generating a polarization in the sample. The polarization field, referred to as the signal field, is then homodyned with the probe field and detected. Thus,

$$E_{signal} = \chi^{(3)} E_{pump} E_{pump}^{*} E_{probe} \tag{3.2}$$

Homodyning signal field with probe field leads to

$$dT = E_{signal} E_{probe}^{*} \tag{3.3}$$

Utilizing equation 3.1, 3.2 and 3.3, we get

$$\frac{dT}{T_0} = \frac{\chi^{(3)}|E_{pump}|^2 E_{probe}E^*_{probe}}{T_0} = \frac{\chi^{(3)} I_{pump} T_0}{T_0} = \chi^{(3)} I_{pump} \quad (3.4)$$

where we have utilized $E_{probe}E^*_{probe} = T_0$, i.e. probe intensity. Thus, the differential PP signal is directly dependent on the pump intensity in the $\chi^{(3)}$ regime. Hence, the signal can simply be increased by increasing the pump intensity. However, it is extremely important to limit the powers incident on the sample such that $\chi^{(3)}$ regime is maintained (and also to avoid damage to the sample). If intensities of pump and probe are increased, beyond a certain power (which is sample dependent), higher order optical effects are enhanced and become important. Thus performing a power dependence experiment, where PP signal is measured for a range of increasing pump powers and signal checked for linearity with pump power, is important for each material and sample geometry.

TWO COLOR PUMP-PROBE

Excitons and trions have different dynamics and physical properties, as we have discussed extensively in chapter 2. Degenerate PP spectroscopy can be used to measure the dynamics of excitons and trions separately. However, measurements of interactions between these quasiparticles can-not be performed since we are limited to only one dimensional spectroscopy. Degenerate PP spectroscopy, though powerful, thus has limitations in inability in measuring interesting coupling phenomena.

Two-color pump-probe spectroscopy (TCPP) circumvents the issues facing degenerate PP spectroscopy and helps in measuring coupling phenomena. The extra dimension provides by TCPP spectroscopy is illustrated in Figure 3.3. Consider two states, $|1\rangle$ and $|2\rangle$, at transition energies ω_1 and ω_2. Using degenerate PP spectroscopy (one-color pump-probe), we can only extract the information represented on the diagonal line. Thus, we can measure the dynamics of the individual states, but not the interactions

between the states. We can-not even say whether the two states are coupled. However, as pump and probe energies are tuned independently and across the transition energies in the TCPP scheme, we measure interactions as represented by the off-diagonal peaks. The dynamics of these off-diagonal peaks provides useful information about the various coupling phenomena between the quasiparticles. Further, in a coherent two-dimensional fourier transform spectroscopy experiment, the width of the diagonal peaks measures the inhomogeneous linewidth while the cross-diagonal width specifies the homogeneous linewidth [180,181]. These measurements thus provide valuable information about the intrinsic physical mechanisms in the system. The measurement of the homogeneous linewidth, for example, provides a measure of the quantum efficiency of the physical system and intrinsic broadening mechanisms [180]. Since a two-color pump-probe experiment does not operate in strictly coherent regime, it measures both coherent and incoherent dynamics. We can distinguish between these using density-matrix calculations described in chapter 4 and Appendix B. Additionally, TCPP dynamics can be used to probe relaxation pathways, as described in chapter 5.

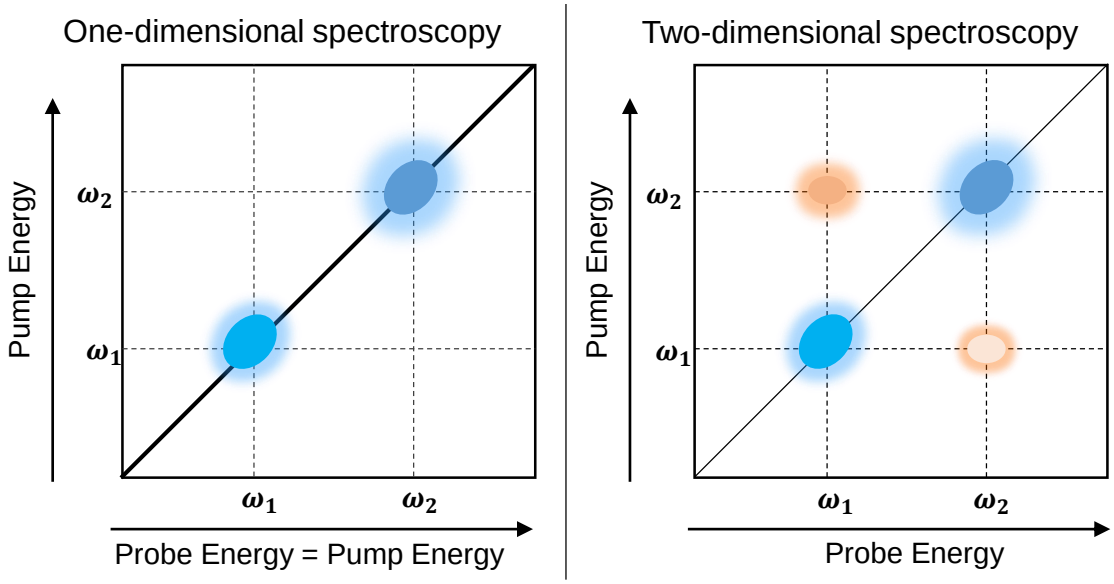

Figure 3.3: Comparison of 1D and 2D pump-probe spectroscopy.

To measure coupling phenomena, it is thus imperative to perform two-color pump-probe (TCPP) spectroscopy. It is also important to distinguish between this scheme and spectrally-resolved pump-probe (SRPP) as described in Figure 3.2. In SRPP experiments, the pump energy is held constant and the probe energy is spectrally dispersed (using a spectrometer), after interacting with the sample. In a TCPP experiment, the pump and probe are both tuned separately through independent pulse shapers. The TCPP setup is illustrated in Figure 3.4. Thus, the pump and probe energies are chosen separately, before interacting with the sample. The difference between SRPP and TCPP is thus subtle but is important to distinguish. TCPP allows constant powers at different probe wavelengths (through additional optics) but SRPP is limited by the available laser spectrum. Further, lower probe powers can be used in TCPP, thus causing less perturbation to the system and staying in the $\chi^{(3)}$ regime. Additionally, TCPP provides more information via pump wavelength tuning which can measure excitation

energy dependent effects such as spin polarization and relaxation pathways. Thus TCPP is superior to SRPP and will be used in this dissertation.

The building blocks of TCPP are illustrated in Figure 3.4. Each of these components are important and we will discuss them in detail. The ultrafast laser utilized in most of the experiments, is a Titanium-Sapphire laser (Ti-Sapph) producing ~ 20 nm band-width (pulse-width ~ 100 fs) pulses. The specific model used is a Griffin-5 oscillator laser manufactured by KM Labs. This laser uses passive Kerr mode-locking and produces pulses at a repetition rate of ~ 80 MHz [170,182]. The laser is pumped using a continuous 532 nm laser (Coherent Verdi V-6) generating broadband light ~ 400 mW (average power), at a center wavelength of 750 nm. The center wavelength and the bandwidth can be tuned by a pair of prisms and a tuning slit inside the cavity. The center wavelength can be tuned through 710-840 nm and thus provides capabilities to study dynamics of a range of physical systems. The mechanism of the laser will be discussed in the later part of this chapter.

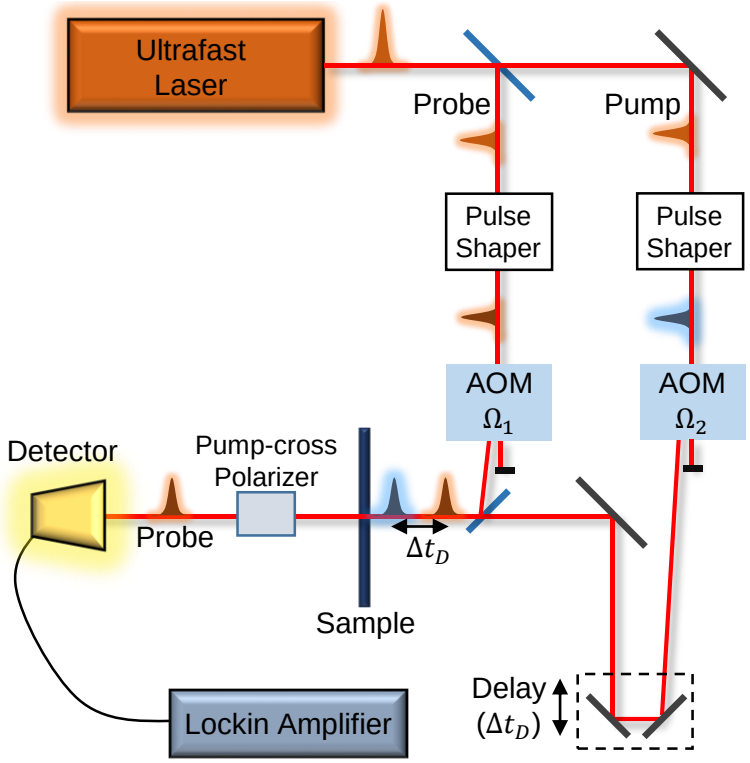

Figure 3.4: Detailed two-color pump-probe setup.

The pulse train of the ultrafast laser is subsequently split into two optical paths using a beam-splitter. Thus, the pump and probe pulses can be controlled separately. The two pulses pass through independent grating based pulse-shapers. The pulse-shaper employs a metallic grating which separates the constituent colors of the ~ 20 nm bandwidth laser. A sharp slit, with controllable width and mechanically controlled position, subsequently selects the desired spectral-width and wavelength. The advantage of the metallic grating, over a prism, is the smaller optical path required to separate closely spaced wavelengths. Thus a resolution of ~ 0.5 nm can be achieved using these grating based pulse shapers. The spectrally shaped pulse is sent back to the grating to remove spectral dispersion of the light spot (compressed 4-f geometry [183,184]). The pulse then passes through a single-mode fiber which acts as a spatial filter, and improves

the spatial mode. The efficiency of light coupling through the fiber is ~ 60% but we get a much cleaner spatial mode. The separate tuning of wavelengths of the pump and probe pulses is illustrated through different colors in the Figure 3.4.

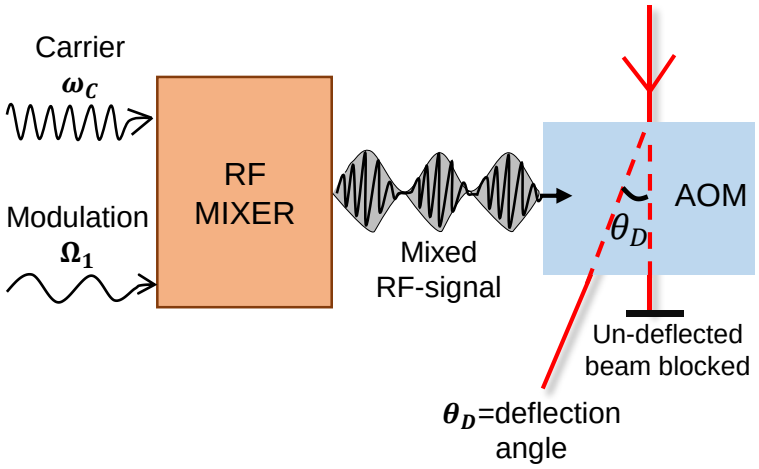

Figure 3.5: Schematic of RF frequency generation and AOM modulation.

The spectrally shaped pulses subsequently pass through acousto-optic modulators (AOMs'). The AOMs' (manufactured by Gooch-Housego) are made of crystalline tellurium dioxide and offer high-frequency modulation. Briefly, a RF carrier wave (ω_C ~ 80 MHz, dependent on the phonon frequency of crystal used) input on the crystal creates a diffraction grating inside the AOM crystal. The incoming laser photon absorbs gets diffracted by this grating, or in other words, the incoming photon absorbs a phonon and gets deflected (momentum conservation). This is referred to as the acousto-optic effect. The deflection angle θ_D, can be adjusted through an adjustment of ω_C, i.e. $\theta_D \propto \omega_C$. This property can be also used for fast spatial scanning across the sample. Importantly, a RF mixer can be used to mix this carrier wave with a modulation wave (Ω_1 ~ 1 MHz). The carrier wave and modulation wave are of the form $A_1\cos(\omega_c t)$ and $A_2\cos(\Omega_1 t)$

respectively. They are combined using an arrangement of RF multipliers and adders to create the RF input (into the AOM) of the form

$$Acos(\omega_c t)[1 + \cos(\Omega_1 t)] \tag{3.5}$$

, where A is the amplitude of the mixed wave. The mixed wave involves the modulation wave acting as the envelope, with fast oscillations of the carrier wave, and is illustrated in Figure 3.5. The deflected wave is, as a result, modulated at the modulation frequency and can be used for lockin detection. The un-deflected beam is blocked. The pump and probe beams are modulated through independent AOMs' at modulation frequencies Ω_1 and Ω_2. This independent control provides enhanced signal-to-noise ratio, as will be discussed in the context of lockin technique.

The pump and probe pulses are delayed, with respect to each other, using a retro-reflector mounted on a mechanical delay stage. The resolution of the stage is ~ 10 nm, and thus the maximum achievable resolution through the stage is 0.06 fs. The time resolution is however limited by the pulse duration. Further, the temporal and spectral resolution of a light pulse are related to each other through $\Delta t \Delta v \geq \hbar$, referred to as the time-bandwidth product. Thus the temporal resolution in our case (~ 1 ps), is limited by the high spectral resolution (~ 1 nm) that we need. However, it can be optimized for the particular experiment and range of dynamics being studied (tens' of fs or ps scale). Importantly, these ~ 1 nm pulses suffer very little pulse broadening when passing through optics, thus no pulse compression techniques are needed. For compression of pulses to minimize the time-bandwidth product, a single prism in a compressed 4f prism geometry can be used [185].

The TCPP setup utilizes collinear geometry, where pump and probe beams overlap before entering the focusing optics. The pump and probe beams are focused on the sample using a 50-X or a 100-X objective (Mitutoyo long working distance) to achieve high spatial resolution and ~ 2 μm spot size. Importantly, as a result of the collinear geometry, the pump travels the same optical path as the probe and gets detected at the detector. To prevent this, we use crossed linear polarizers for pump and probe beams, and in the detection path, place a linear polarizer crossed with the pump polarizer. This polarizer blocks the pump and lets the probe through and thus, only the probe is detected at the detector. This configuration is ideal for measuring carrier dynamics, and will be utilized in chapter 4 and chapter 5. For measuring spin (or valley) polarization experiments, this scheme can-not be used since the linear polarizer destroys all spin information. We then use slightly off-resonant pump excitation (spectrally ~ 1 nm away from probe) and further spectral filtering (using a spectrometer), for measuring spin in chapter 6 and chapter 7.

Generally, the PP signal is two orders of magnitude less than the probe, thus filtering techniques are needed to separate PP signal from the large probe signal. The detection of the PP signal involves the probe being detected by a single channel silicon detector (one detection arm of the Newport balanced photo-receiver). The electrical signal generated contains the PP and probe signal, as well as background noise. For separating PP signal, modulation techniques are employed, which improve the sensitivity by electrical measurement at the modulation frequency only. Consider the probe and pump beams modulated at Ω_1 and Ω_2 respectively, i.e. probe $\propto \cos(\Omega_1 t)$ and pump $\propto \cos(\Omega_2 t)$. Then, the PP signal is of the form (utilizing equation 3.4)

$$dT = \chi^{(3)} I_{probe} I_{pump} \propto \cos(\Omega_1 t)\cos(\Omega_2 t) \propto \cos[(\Omega_1 \pm \Omega_2)t] \qquad (3.6)$$

Thus, the PP signal is modulated at the sum and difference frequencies of probe and pump modulation. The double modulation of PP signal improves the signal-to-noise ratio since the 1/f noise decreases for high frequencies (Ω_1, Ω_2), while the PP electric signal sent to a lockin-amplifier (referred to as lockin) is within the lockin frequency operating range. The working of a lockin (Stanford Instruments SR830), used for demodulation, is illustrated in Figure 3.6. A lockin can extract a signal up-to a million times smaller than the noisy background and works by demodulating the signal at the chosen frequency. The frequency (of demodulation) at which the desired signal is oscillating, is input into the lockin, which subsequently generates a reference signal at the same frequency (but spectrally purer). The reference signal (R) is generated through the internal digital oscillator of the lockin. We choose the difference PP frequency in our experiment since it is of the order ~ 50 KHz (Ω_1 ~ 1.05 MHz, Ω_2 ~ 1 MHz), and is in the operating range of the lockin. The reference frequency wave is multiplied by the total signal and integrated over a chosen time interval t_0 (integration time constant). Consider the total signal $S(\Omega_1, \Omega_2, \Omega_3 \ldots.)$ input into the lockin. The desired (PP) signal oscillates at the difference frequency ($\Omega_1 - \Omega_2$). Then

$$dT \propto \int_0^{t_0} [S(\Omega_1, \Omega_2, \Omega_3 \ldots.)]\, R[(\Omega_1 - \Omega_2)t]\, dt \tag{3.7}$$

, where $R[(\Omega_1 - \Omega_2)t]$ is the reference signal. The result is a DC signal with contributions only from signal components oscillating at the reference frequency. Signal components at all other frequencies average out to zero. Additionally, the integration time constant is chosen as small as possible, but high enough to average over slowly varying noise, i.e. to average out components varying at frequencies above $1/t_0$. These

components usually arise due to low frequency mechanical vibrations (~ 100 Hz) and can affect the signal-to-noise ratio if not averaged. Further improvement can be achieved using passive bandpass filters. For example, to detect a ~ 50 Khz signal, we use bandpass filters (inbuilt the detector) from 10 KHz – 100 KHz, which improves source signal (into the lockin) tremendously. This also helps in preventing overload of lockin internal filters by blocking the ~ 1 MHz probe signal from getting into the input of the lockin. In the experiment, we measure dT and T_0 separately, and subsequently calculate the differential PP signal. Note that the silicon detectors have a responsivity range of 400 – 1100 nm. The quantum efficiency of these detectors is particularly high in the range 700 - 1000 nm, and are thus ideal for the measurement of optical transitions in TMDs' and quantum wells.

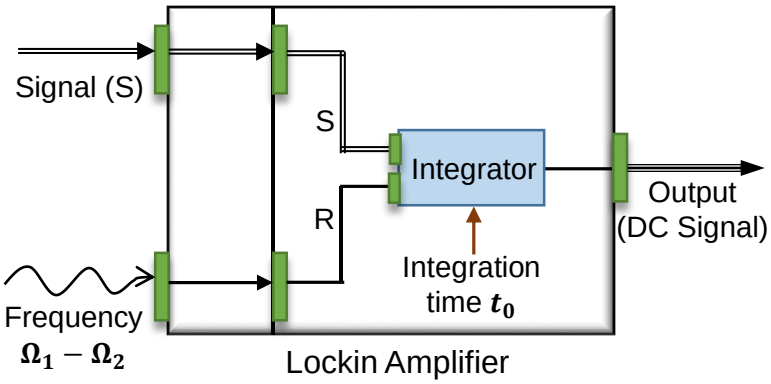

Figure 3.6: Schematic of lockin-amplifier illustrating signal (S) and reference frequency (R) convolution using the integrator.

DRIFT CONTROL AND HIGH SPATIAL RESOLUTION

Mechanically exfoliated monolayer TMD samples are high quality and crystalline. However, they have spatial dimensions ~ 5 μm and thus are quite small. Additionally, the edges of the samples have shown to exhibit different properties from the rest of the crystal. The edges could have metallic nature and also have higher density of

impurity states [88,152,186]. Even within the crystal, due to the extreme two-dimensionality of the monolayer and importance of the surface, small regions have different behavior from the rest due to presence of adsorbates. These different regions can have physical properties separate from each other and thus, it is important to limit studies to a particular region of the sample. Further, the thermal drift due to temperature variations in the cryostat and, mechanical creep due to optical components, causes a relative motion of the laser spot on the sample. Hence, it is imperative that we utilize a mechanical drift control protocol that minimizes the relative motion of the laser spot and the sample.

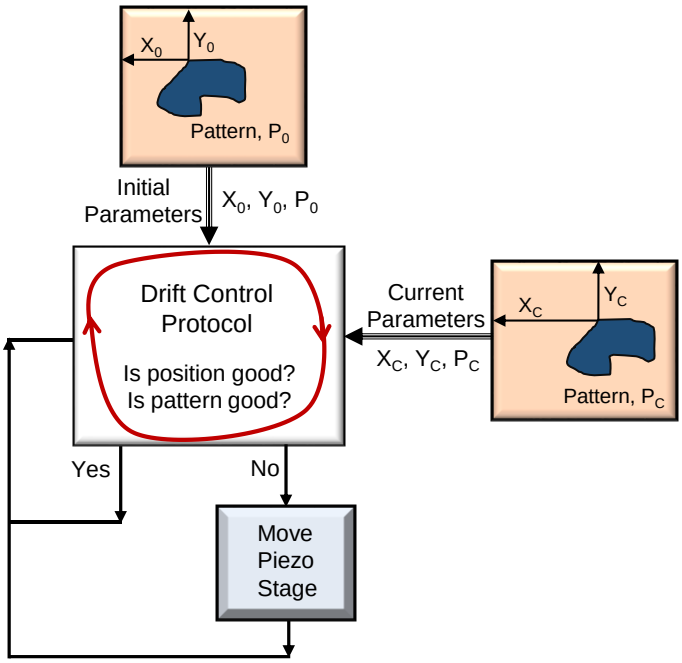

Figure 3.7: Schematic of drift control protocol implemented via labview.

The drift control protocol that we utilize, can correct for sub-micron motion of the laser spot on the sample. The protocol is illustrated in Figure 3.7 and is implemented via a combination of imaging devices and piezo-controlled mechanical stages. LabVIEW is

used to control these different devices and implement the control procedure. Briefly, the sample is continuously imaged through a high resolution microscope objective and a white light source. The image is sent to a camera with pixels 576 X 576 and a field of view of 20 μm. Thus each pixel is ~ 0.04 μm. Hence, using this method, and fitting the selected portion of the image, we can get sub-micron spatial resolution ~ 0.1 μm.

The selected portion of the image is referred to as the initial pattern P_0. The pattern shape and position is identified using the in-built labview imaging sub-vi. The sample is continuously imaged, as mentioned, and the current pattern parameters are compared with the initial parameters. In case of any change in position (X or Y), the microscope objective mounted on the piezo stage (resolution ~ 0.01 μm) is moved accordingly, according to calibrated pixel to μm conversion (pixel ~ 0.04 μm). A similar protocol is employed for monitoring the focus (Z position) by monitoring the width of the laser spot and adjusting the piezo stage focus. Thus we get a fine control of all three spatial dimensions with this drift control protocol, and can keep the sample within ~ 0.1 μm of the initial position. Note that the control is also dependent on the quality of the image and the contrast of the sample compared to the substrate. If the stage moves out of range, or the quality of the image degrades due to ambient light, the setup stops taking data and asks the user to take corrective measures. With this continuous drift control protocol and complete computer control of the setup, we can take measurements for a day continuously (or even more). Further, this tremendously improves the data quality and removes human (grad-student) error.

LASER

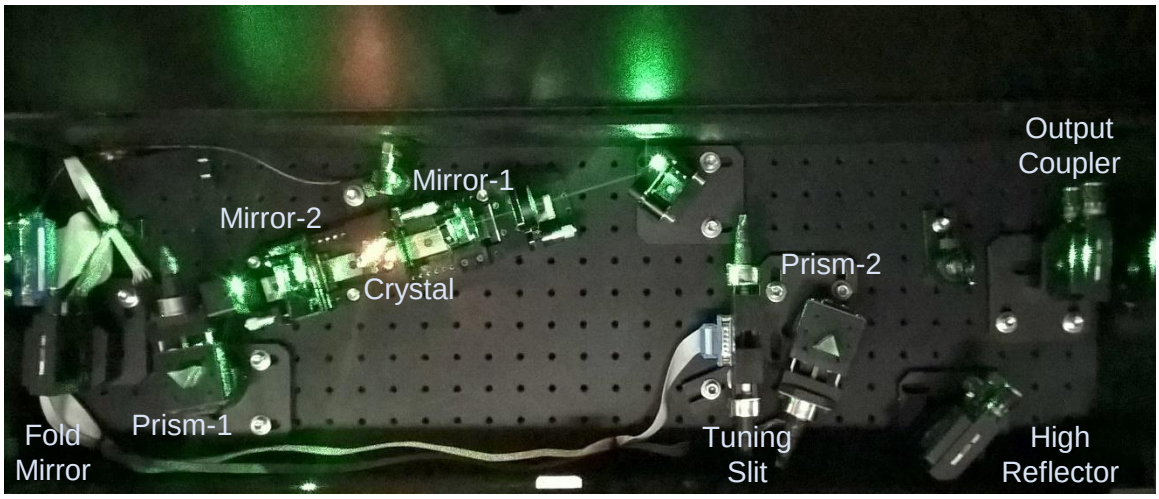

Figure 3.8: Picture of the Griffin-5 laser cavity.

For doing these time-resolved PP experiments we employ a Griffin-5 oscillator laser manufactured by KM Labs. The components of the laser cavity are illustrated in a photograph of the laser cavity. A green laser (532 nm) can also be seen, which pumps the nonlinear Titanium-Sapphire (Ti-Sapph) crystal, and has an average power of 4 – 6 W (depending on the wavelength of the ultrafast laser output desired), in a clean TEM_{00} mode. A Verdi V-6 laser, utilizing a diode-pumped neodymium-doped yttrium-orthovanadate crystal and subsequent second harmonic generation (using lithium triborate, LBO), is an extremely stable single frequency continuous wave source. This green laser is also used for photoluminescence experiments, useful for measuring optical resonances in a single-shot.

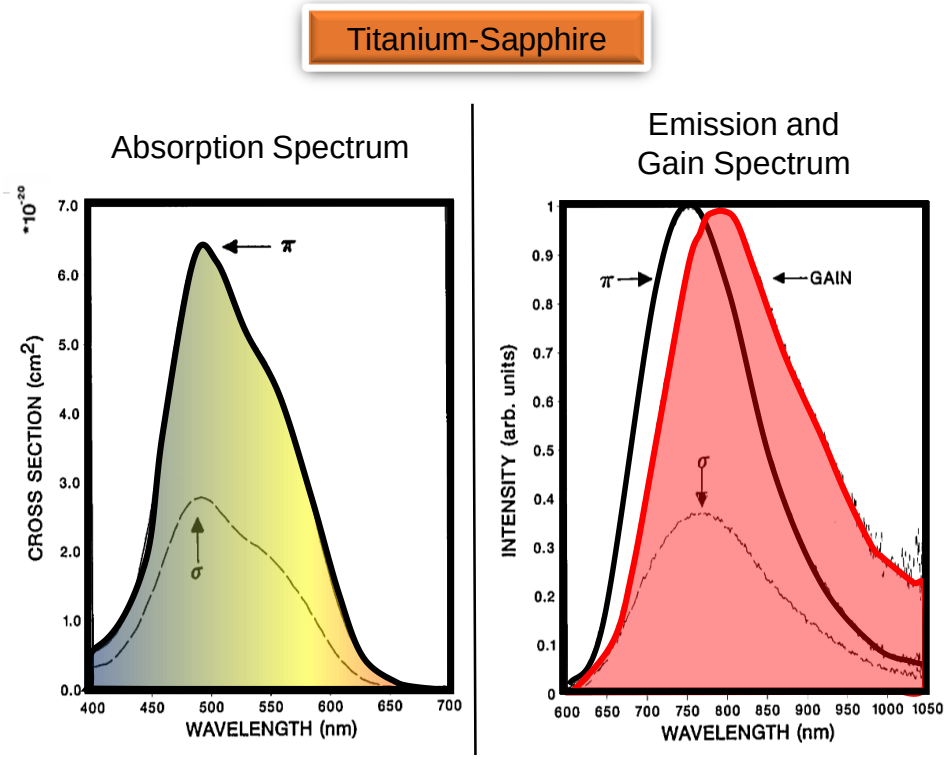

Figure 3.9: Absorption, Emission and calculated Gain spectra of Ti-Sapph (modified from [187]).

The Ti-Sapph crystal acts as the active non-linear crystal producing luminescence, as well as the Kerr-lens effect enabling the pulsed operation. Ti-Sapph refers to a crystal of sapphire doped with Ti^{3+} ions, which act as the lasing medium. The absorption and emission of Ti-Sapph is shown in Figure 3.9 (modified from [187]). Note that the absorption of 532 nm pump laser is quite high. Additionally, the absorption and emission of the Ti-Saph are highly (linear) polarization dependent (represented by σ, π), thus maintaining the correct pump-polarization is important. The range of lasing using a Ti-Sapph crystal is 675 nm – 1050 nm (due to significant overlap of absorption and emission profiles around 650 nm), as also illustrated by the calculated gain spectra [187,188]. Inside the laser cavity, the emission (luminescence) of the crystal is collected by the two

curved mirrors (Mirror-1 and Mirror-2) and goes around the cavity folded by the fold mirror (Figure 3.8). The two prisms are involved in dispersion control and the tuning slit is useful for choosing the center wavelength and bandwidth of the output laser. The output coupler and high reflector are broadband mirrors which act as the end-mirrors of the laser cavity.

The nonlinear process involved in pulse generation is Kerr-lens-modelocking, a type of passive modelocking. Briefly, the Ti-Sapph crystal has an intensity dependent refractive index

$$n = n_0 + n_2 I \tag{3.8}$$

, where n_2 and I are nonlinear refractive index and intensity respectively [170]. This causes self-focusing of propagating light, and is referred to as Kerr-lensing. This focusing causes saturable absorption of the active medium, due to the increasing intensities of modes above a certain intensity while causing loss for modes below it. After a round trip of these resonator modes, when a number of these resonator modes are in phase, this saturable absorption ultimately results in short (~ 20 fs) pulses of light. The consequence of using a single component for lasing and mode-locking is a simple cavity design, and ~ 80 MHz repetition rate laser output which is stable for hours. The center wavelength of the output can be tuned through 710-840 nm. The output power is highest at 800 nm, but with installation of an additional blue optics set inside the laser cavity, the output power at 710 – 760 nm can be enhanced.

CRYOSTAT

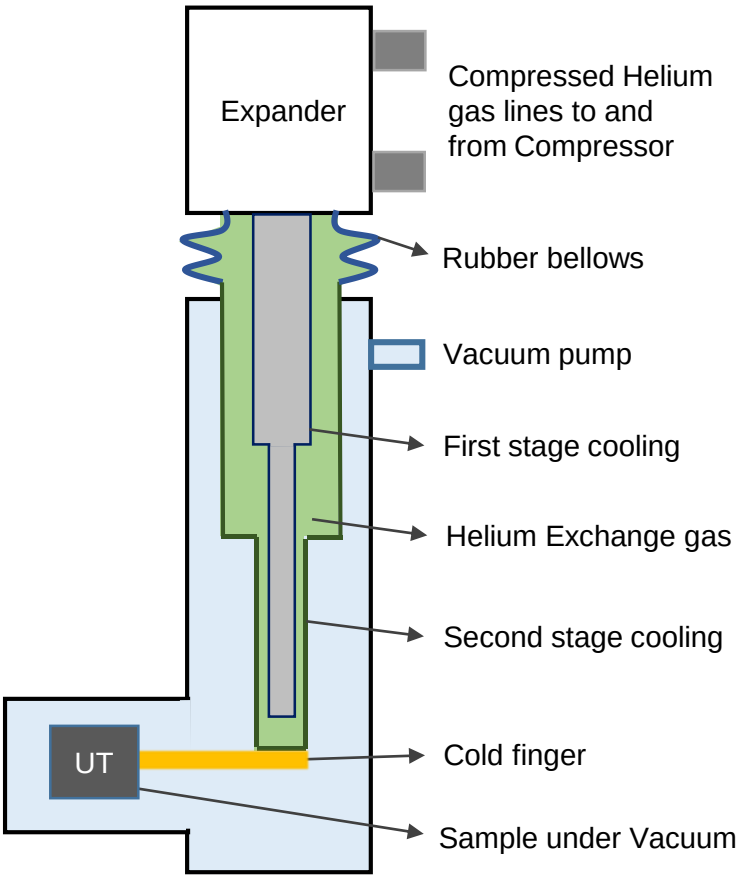

Figure 3.10: Schematic of the inner components of the closed loop cryostat.

Optical quasiparticles (excitons, trions) are essentially quantum transitions. The interaction between them, which is the focus of this dissertation, can be seen without the effect of phonons and temperature related effects at cryogenic temperatures. Therefore we utilize a cryostat operating at 13 K to measure these quantum phenomena. Specifically, we utilize an ARS closed loop cryostat (combination of ARS-4HW compressor and DE-204 expander), equipped with vibration isolating DMX-20 (rubber bellows) interface. The components of the cryostat are illustrated in Figure 3.10. Briefly,

the closed loop cryostat operates on the principle of Gifford-McMahon refrigeration cycle [189,190]. It consists of a compressor, expander and a two-stage cold station. The compressor compresses high-purity (99.999%) Helium gas at 250 psig which is subsequently transported to the expander through high-pressure gas lines. The gas expands in the expander and as a result, cools down. The low pressure gas is sent back to the compressor. The first stage of the cooling station is directly connected to the expander and is the coolest part of the system. However, due to mechanical motion of the expander, there is around ~ 30 μm motion of this first stage of the cooling station, and hence vibration control is necessary. For this, a second cooling stage is used, which is mechanically isolated from the first cooling stage. For the purpose of vibration isolation, rubber bellows are used, which damp the vibrations. Helium gas (input into the bellows, separate from gas in the expander) acts as an exchange gas between the first and second stages, and cools the second stage through convection. The sample (labelled UT) is mounted on a copper cold finger directly attached to the second cooling stage. A minimum temperature of ~ 10 K can be reached at the sample, and the temperature can be monitored through thermocouples. Temperature can also be changed using resistance heaters coupled to the thermocouple, enabling temperature dependent measurements. We optimized the stretching of the rubber bellows and gas flow into the bellows to minimize vibrations. By doing this, we get no observable vibrations at the sample (monitored by an optical microscope). Thus, all the components of the setup were optimized to make the observation of the delicate quantum phenomena possible.

Chapter 4: Coherent Electronic Coupling in Transition Metal Dichalcogenides

INTRODUCTION*

Monolayer transition metal dichalcogenides (TMDs) represent a new class of direct band gap semiconductor materials at the two dimensional limit [85,86]. As we have discussed in chapter 2, they also exhibit intriguing coupled spin-valley physics [93,94,108,109]. Additionally, the exciton and trion binding energies in TMD's are an order of magnitude larger than those in quasi-2D systems (e.g., GaAs quantum wells), making these quasiparticles relevant for optoelectronic devices [122,129,191]. These binding energies are a result of strong Coulomb interactions arising from strong quantum confinement and reduced screening due to the monolayer thickness. The electric field lines leak into the vacuum environment and thus there is reduced screening due to the ultrathin material nature. Studies have demonstrated control of these quasiparticles through strain, doping, and applied electrostatic field [129,165,192]. Further, interaction effects have been studied such as exciton-carrier broadening, inter-excitonic scattering, exciton valley relaxation dynamics, and biexciton formation [179,193-196].

It is reasonable to speculate that enhanced Coulomb interactions responsible for the large exciton and trion binding energies should also lead to strong coupling among these quasiparticles. A study of the nature of coupling between these excitons and trions is however lacking. The presence of coupling would necessitate a combined treatment of material response to applied electric and optical fields. In other words, excitons and trions cannot be treated independent of each other. Further, discerning the nature of coupling,

* This work was published as A. Singh, G. Moody, S. Wu, Y. Wu, N. J. Ghimire, J. Yan, D. G. Mandrus, X. Xu, and X. Li, *Coherent Electronic Coupling in Atomically Thin MoSe2*, Phys. Rev. Lett. **112**, 216804 (2014). I (A. Singh) was responsible for the experimental measurements, data analysis and manuscript preparation.

i.e. whether these are coherently or incoherently coupled, is important for applications including transport and photodetection [130,197,198]. It is imperative to understand the properties of these intrinsically many-body states in TMDs. Additionally, since these many-body states are also coupled to valley (K or K'), they shed light on valley depolarization and scattering phenomena.

We demonstrate that monolayer TMDs exhibit strong exciton-trion coherent coupling. We perform two-color pump-probe spectroscopy on a high quality monolayer $MoSe_2$ sample with spectrally well-resolved exciton and trion resonances. Cross peaks in the two-dimensional spectrum reveal electronic coupling between these quasiparticles. We specially focus on the TX peak, i.e. pump (probe) tuned to the trion (exciton) transition. Density matrix calculations reveal that the unique line shape of the TX peak results from coherent exciton-trion many-body interactions. While incoherent population relaxation partially contributes to the coupling, we see that coherent coupling dominates the response. We model the optical response using density matrix formalism and incorporate the many-body effects through phenomenological parameters such as excitation induced shift and excitation induced dephasing.

EXPERIMENTAL SETUP AND SAMPLE INFORMATION

The experimental setup is described in chapter 3. Briefly, the output of a mode-locked Ti:sapphire laser is split into two beams, modified independently using two grating-based pulse shapers, producing ~1 ps pulses (~2 nm bandwidth FWHM). The pump and probe beams are collinear and focused to a ~3 μm spot on the sample using a 100-X Mitutoyo microscopic objective. The two beams are cross-linearly polarized to suppress scattering from the pump into the detection optics. Because cross-linear polarization is used to suppress pump scattering, we do not distinguish between the valley

or spin degrees of freedom of the quasiparticles. We instead focus on the coupling mechanisms between these quasiparticles. The average power is kept below 10 μW to ensure that the signal remains in the $\chi(3)$ regime and ensuring no power dependent phenomena are activated. The pump-induced change in the probe reflectivity is recorded using a lock-in amplifier while the pump and probe wavelengths are systematically varied. The differential reflectivity spectra is given by $^{dR}/_{R_0} = (R - R_0)/R_0$, where R ($R_0$) is probe reflectivity with (without) pump on the sample.

The monolayer $MoSe_2$ was obtained via mechanical exfoliation of a bulk $MoSe_2$ crystal (created by collaborators in Oak Ridge National Laboratory). The monolayer was exfoliated onto a 285-nm- thick SiO_2 on an *n*-doped silicon substrate, thus primarily we would be sensitive to negatively charged trions. Isolation of a single layer was verified through optical and atomic force microscopy. An optical microscope image of the sample is shown in Figure 4.1. The monolayer can be clearly seen on the bare silicon substrate. The sample was mounted in a closed-loop cryostat cooled to 13K. At this temperature, we avoid phonon-mediated broadening of the resonance linewidths and other phonon-mediated processes (thermal relaxation). The linewidths at this temperature are dominated by inhomogeneous broadening [180].

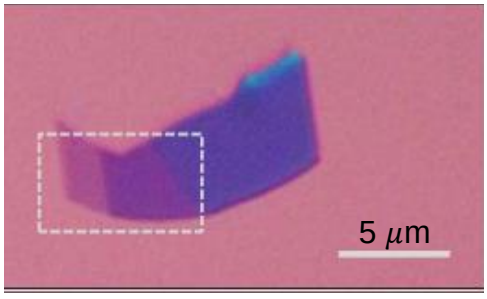

Figure 4.1: Monolayer $MoSe_2$ on silicon substrate.

To extract the spectral positions of exciton and trion transitions, we perform a degenerate pump-probe experiment in which both beams are derived from the same pulse shaper. The degenerate pump-probe spectrum, shown in Figure 4.2 for a fixed time delay = 0.7 ps, was used to identify exciton (X) and trion (T) resonances at ~ 1650 meV and ~ 1619 meV respectively. The trion optical response in this sample is much weaker compared to the exciton and has been increased by 10X in the figure to enhance visibility. Additionally, the spectral positions of the peaks and trion binding energy (~ 30 meV) are consistent with values obtained from photoluminescence spectra of similarly-fabricated samples [129]. However, as the name suggests, one-dimensional pump-probe spectra cannot provide information regarding coupling between excitons and trions.

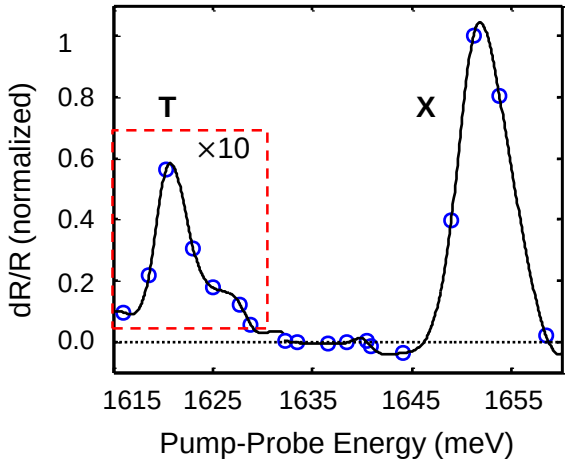

Figure 4.2: Degenerate pump-probe spectrum.

Two-color pump-probe spectroscopy provides the coupling information between the quasiparticles. We show the normalized differential reflectivity spectrum in Figure 4.3. The spectrum was acquired for a delay t_D = 0.7 ps. The choice of this delay is important as we want to minimize relaxation behavior and incoherent population transfer, while still working in the positive time delay regime. The spectrum in Figure 4.3 features

four peaks– two diagonal peaks corresponding to the exciton (X) and trion (T) respectively, a cross-peak when pumping at the trion and probing at the exciton (TX), and vice versa (XT). We will investigate the dynamics of these peaks in detail in chapter 5.

The cross-peaks are a signature of coupling processes between excitons and trions in these materials. A differential probe spectrum for resonant pumping at the exciton and trion is shown by the upper and lower horizontal slices, respectively, where the curves serve as a guide-to-the-eye. Clearly, there are differences in the probe spectrum when the pump energy is switched from exciton to trion. The different line shapes of the XT and TX coupling peaks, dispersive vs mostly negative, suggests that the coupling is not simply due to incoherent population transfer. We will explore the possibility of the difference originating from exciton-trion many-body interactions.

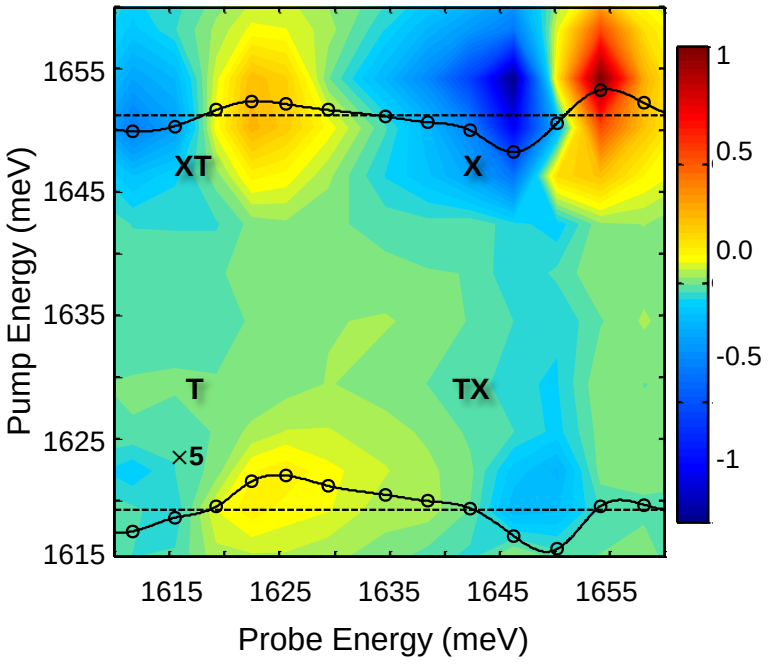

Figure 4.3: Two-color pump-probe spectrum at delay = 0.7 ps.

HILBERT TRANSFORMATION AND CONSTRUCTION OF PHENOMENOLOGICAL MODEL

We construct a phenomenological model to explain the coupling mechanism. We utilize a Hilbert space transformation to map two two-level systems into a four-level system, as illustrated in Figure 4.4. This is a general transformation and does not make any assumptions about coupling of the exciton and trion states. If the states are not coupled, the four level diagram collapses back into two two-level diagrams. The two two-level diagrams are $|g\rangle \leftrightarrow |T\rangle$ and $|g\rangle \leftrightarrow |X\rangle$, where $|g\rangle$, $|T\rangle$ and $|X\rangle$ represent the crystal ground state, trion and exciton respectively. After transformation into the four level diagram, state $|0\rangle$ refers to the crystal ground state in the absence of any optical excitation; states $|1\rangle$ and $|2\rangle$ represent the trion and exciton, respectively; and state $|3\rangle$ represents simultaneous excitation of the exciton and trion.

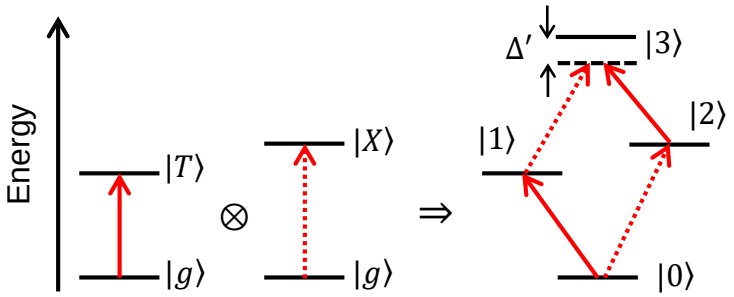

Figure 4.4: Illustration of a Hilbert space transformation relevant to the phenomenological model.

The density matrix and corresponding optical bloch equations (OBEs), as we have discussed in chapter 2, are ideal to elucidate the dynamics of the system, including population relaxation and dephasing [199]. The third order nonlinear signal can be calculated through third order OBE's. We solve the OBE's perturbatively up to third order in the excitation (and detection) field to calculate the nonlinear signal detected (or emitted) in the pump-probe experiment. The total nonlinear response can be generated

through a combination of various different physical processes. The different processes can be accounted for using a combination of double-sided Feynman diagrams, illustrated in Figure 4.5 [200]. Each diagram represents a distinct quantum mechanical pathway that contributes to the nonlinear signal. For each diagram, the first two arrows indicate interaction of sample with the pump field and the third arrow indicates interaction of the probe field after a delay t_D. We have applied a number of rules to generate the relevant Feynman diagrams. Firstly, we have implied pulse ordering, i.e. the pump pulse comes before the probe pulse. Secondly, we consider the pump field acts twice (field and its conjugate). Thirdly, we have taken in account that the signal field is homodyned with the probe field for detection. Thus, we have considered the signal and the probe field to have same energy and direction. Thus we get a total of 16 diagrams, four for each of the four peaks. From each diagram, one can generate an expression for the perturbative evolution of the density matrix [23]. Details of this calculation are explained in Appendix B. We briefly present the important physical parameters involved in the calculation.

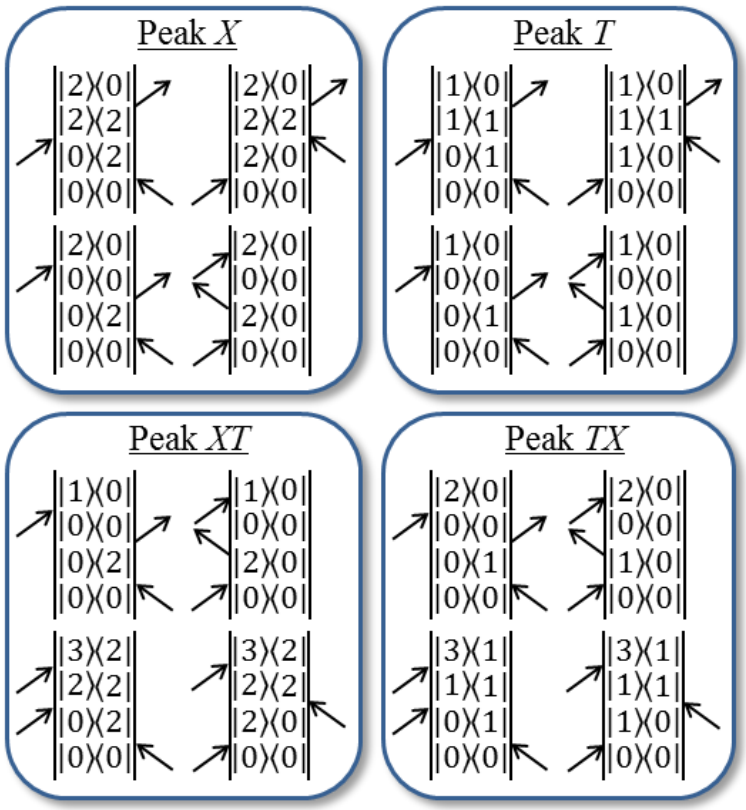

Figure 4.5: Double sided Feynman diagrams relevant to two-color pump-probe experiment.

Many-body interactions are included in this four-level energy scheme in a simple and intuitive manner. The lower transitions ($|0\rangle \leftrightarrow |1\rangle$ and $|0\rangle \leftrightarrow |2\rangle$) are excited by the optical field to first order in perturbation theory, while the upper transitions ($|1\rangle \leftrightarrow |3\rangle$ and $|2\rangle \leftrightarrow |3\rangle$) contribute to third order only if the lower transitions have been excited. Thus, the interactions between $|1\rangle$ and $|2\rangle$, or specifically, trion and exciton, are governed by the properties of the upper transitions [201]. To uncover the nature of the upper transitions, we consider excitation-induced energy shift (EIS) and excitation-induced dephasing (EID) effects. These effects have been invoked to explain coherent exciton coupling phenomenologically in semiconductor quantum wells and quantum dots

[202-205]. EIS and EID arise from a renormalization of energy when interaction effects are considered and correspond to the real and imaginary part of the renormalization energy. Thus both effects must appear simultaneously, in principle. In our calculations, EIS effects are taken in account by considering an energy shift Δ' of state $|3\rangle$ that breaks the energy equality of the lower and upper transitions. This energy shift is illustrated in Figure 4.4 and breaks the energy degeneracy of, for example, $|0\rangle \leftrightarrow |1\rangle$ and $|2\rangle \leftrightarrow |3\rangle$. On the other hand, EID effects are taken in account by increasing the dephasing rate of either (or both) of the upper transitions with respect to the equivalent lower transition by an amount γ'.

We now give an example of how the density matrix is calculated from the Feynman diagrams via OBEs. We show an expression of $\rho_{13}^{(3)}$, which is the third order polarization connected to the bottom two Feynman diagrams for the peak TX. We also include phenomenological parameters related to the many-body effects.

$$\dot{\rho}_{13}^{(3)} = \left\{-i\left(\omega_{20} - \frac{\Delta'}{\hbar}\right) - (\gamma_{20} + \gamma')\right\}\rho_{13}^{(3)} + \frac{i\mu_{13}}{2\hbar}\hat{E}\rho_{11}^{(2)} \tag{4.1}$$

Here, $\dot{\rho}_{13}^{(3)}$ represents the time derivative of the third order polarization $\rho_{13}^{(3)}$. The dipole moment, resonance energy, and dephasing rate of the transition are given by μ_{13}, $\hbar\omega_{13} \sim \hbar\omega_{20} - \Delta'$ and $\gamma_{13} = \gamma_{20} + \gamma'$, respectively. $\hat{E}$ is the electric field, $\Delta'$and γ' are the EIS and EID parameters for this pathway. We describe how we have chosen the parameters for all pathways in detail in Appendix B. However, the precise values do not affect the line shape qualitatively. We discuss these parameters in the next section.

ANALYSIS OF SPECTRAL LINE-SHAPE AND MANY-BODY EFFECTS

The role of coherent many-body interactions can be modelled by carefully analyzing the line-shape of each peak in the 2D map. We stress that the entire 2D spectrum has to be analyzed at the same time. This is critical since the lineshape of each peak is sensitive to a phase shift between the reflected signal and probe. The origin of this phase shift is a relative path difference between the probe and signal. A large percentage of the probe is reflected from the silicon oxide and silicon substrate, while the signal is only emitted by the monolayer. We explain and calculate this phase shift further in Appendix C. However, this phase shift is nearly constant across the entire 2D spectrum, and thus can be accounted for. Thus the relative amplitude and lineshape of the peaks provides critical information that enables us to distinguish between the coupling mechanisms. We note that the exciton and trion relative amplitudes are related not only to quantities that characterize these transitions (dipole moments and dephasing rates), but also to the background charge density determined by the *n*-doping in the material. Thus the amplitude ratio between TX/T and XT/X is the key parameter for evaluating the role of incoherent population relaxation and coherent effects. Thus comparing (experiment vs simulations) both the amplitude ratio and the line-shape is important.

The interaction effects are brought out in the calculation in three steps. The first step is to simulate the spectrum considering no exciton-trion interactions and is presented in Figure 4.6(a). The absence of interactions is modeled by using the same parameters (dipole moment, dephasing rate, and resonance energy) for the corresponding lower and upper transitions. Following our discussion, the use of same parameters for upper and lower transitions causes the quantum pathways responsible for coupling between the lower transitions to be completely cancelled by pathways involving the upper transitions. This is due to the completely general Hilbert transformation discussed in section 4.3.

Thus, no cross-peaks appear in the spectrum. The X and T peaks do appear in the simulated spectrum and resemble the experimental data quite closely.

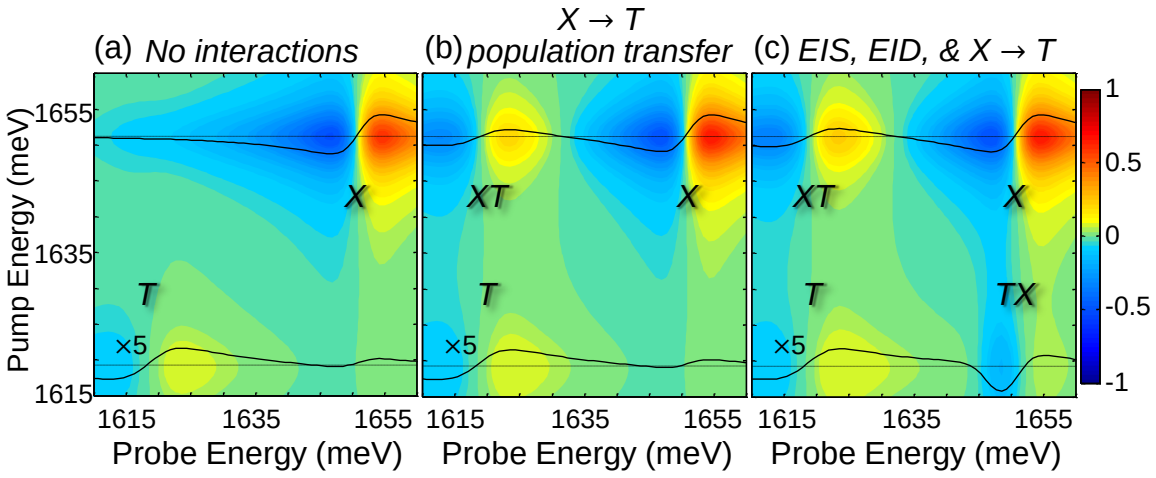

Figure 4.6: Simulation results considering a) no interactions, b) incoherent relaxation, c) relaxation and many-body effects.

In the second step, we consider only population relaxation between the exciton and trion states. We include population relaxation by including the parameter γ^{pop}. As shown in Figure 4.6(b), the 2D map features highly asymmetric cross-peaks. The XT peak resembles the data seen in the experiment but the TX peak in the simulated spectrum is very small. Further, the line-shape is also very different for the TX peak. Coming back to the XT peak, we know that the formation of the XT cross-peak requires the capture of an extra electron by the photo-excited exciton, which is energetically favorable due to the lower energy of trion (compared to exciton). In other words, the relaxation of the exciton to trion is thermodynamically favorable. For a sufficient background density of electrons, the XT peak will have an appreciable amplitude. The dynamics of this process will be studied in detail in chapter 5. Conversely, the formation of the cross-peak TX requires additional energy from other mechanisms, such as

annihilation of a phonon with an energy equal to the trion binding energy ≈ 30 meV. The phonon energy in this system is around 30 meV, however due to the low temperature (~ 13K), no significant phonon population can be expected. We then expect a small amplitude ratio between TX and T. Clearly, incoherent population alone cannot explain the large amplitude of the TX peak in Figure 4.3. Therefore, our simulation till step 2 demonstrates that incoherent population transfer alone cannot reproduce the lineshape for TX as well as the amplitude ratio TX/T.

Finally, in the third step, we include many-body effects (EIS and EID) in addition to incoherent relaxation (as discussed in step 2). The role of coherent coupling mechanisms is thus examined in this step. The term "coherent" is used to distinguish these mechanisms from incoherent population relaxation processes discussed in step 2. We see that the simulated spectrum shown in Figure 4.6(c) compares very well with the actual experimental data (Figure 4.3). The line-shape and the amplitude ratio of both the cross peaks look similar to the experimental data.

We make a more quantitative comparison between the simulated and measured spectra by taking two horizontal cuts through the 2D maps, pumping at the exciton resonance and pumping at the trion resonance. The comparison of the three calculation steps and the experimental results are summarized in Figure 4.7. The pump energy (indicated by the arrow) was tuned to the exciton and trion resonance in the top and bottom panel respectively. The experimental data points, step 1 (no interactions), step 2 (incoherent relaxation), step 3 (many body effects and relaxation) are represented by blue dots, red curves, blue curves and black curves respectively. Best agreement between simulation and experiment is obtained when including EIS and EID effects (black curves), particularly for the TX peak.

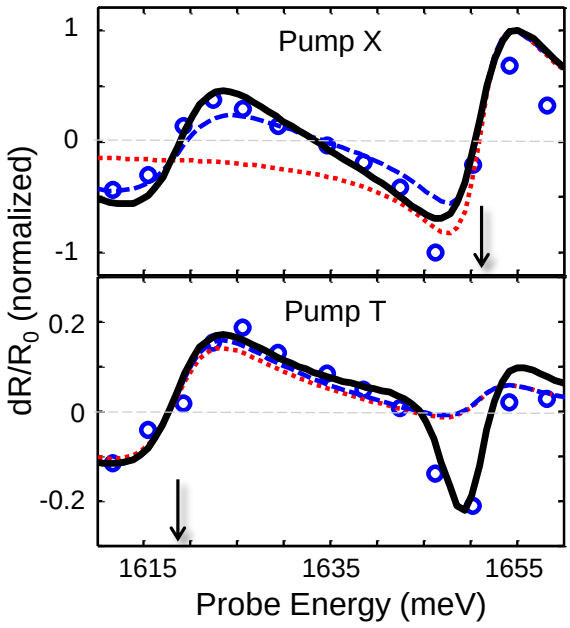

Figure 4.7: Comparison of the three steps in the simulation, with the experimental data.

This fitting suggests a binding energy for the exciton-trion correlated state of $\Delta' = 4 \pm 1.5$ meV for the excitation conditions used in the experiment. The parameters used for the black curve are summarized in Table 4.1. The details of fitting have been discussed in Appendix B. The exact value of Δ' depends on the specific phenomenological model used. Inclusion of additional states to model exciton-exciton and trion-trion correlations reduces Δ' by approximately a factor of 2. However, we emphasize that the distinct line-shape of peak TX, namely, a negative peak rather than the dispersive line-shape for the other three peaks, can only be reproduced by including the EIS effect. This distinct line-shape cannot be replicated through the addition or alteration of any other parameters. Only by including EIS, we can get good agreement for both amplitude ratio and line-shape for the peak TX. Further, EID is necessary to enhance ratio of XT compared to TX. The large value of EID indicates fast dephasing of the

correlated state [203]. Therefore, the coherent coupling mechanism is robust in these materials.

	$\|0\rangle \leftrightarrow \|1\rangle$	$\|2\rangle \leftrightarrow \|3\rangle$	$\|0\rangle \leftrightarrow \|2\rangle$	$\|1\rangle \leftrightarrow \|3\rangle$
μ	0.85		1	
γ (meV)	6	$\gamma_{01} + \gamma'$ $\gamma' = 25$ **(EID)**	4	4
γ^{pop} (meV) (population relaxation)	1	-	0.1	-
E (meV)	$E_1 =$ 1619	$E_1 - \Delta'$; $\Delta' = 4$ **(EIS)**	$E_2 = 1651$	$E_2 - \Delta'$;

Table 4.1: Parameters used to simulate many-body effects in Figure 4.7.

IMPLICATIONS OF COHERENT COUPLING

These experiments establish that strong coherent coupling exists between the excitons and trions in TMD's. For example, $\Delta' \approx 4$ meV observed here is at least an order of magnitude larger compared to exciton-trion coupling in a 20-nm-wide *n*-doped CdTe/CdMgTe quantum well [203]. The primary reason for this large interaction strength is due to the reduced screening in these materials as well as the quantum confinement of the exciton (and trion) wavefunction. Interestingly, a general scaling law seems to be applicable here wherein the exciton binding energy is also large in these materials (compared to GaAs etc.).

These results have several consequences. Firstly, coherent coupling between the quasiparticles suggest new approaches for manipulating spin and valley degrees of freedom associated with each quasiparticle. This is especially relevant for valleytronics

since different valley coherence and polarization dynamics were recently demonstrated for excitons and trions [124,148]. For example, optical initialization in valley Hall experiments could be performed through the trion resonance, which exhibits a (spin) valley polarization more long-lived than the exciton. Second, coherent coupling between excitons and trions may allow efficient exciton transport beyond the diffusive regime [128]. Quantum coherence has been shown to drive efficient exciton transport in photosynthesis and similar principles may apply for charge and energy transfer processes in TMDs [39,130,206]. Finally, our results should motivate the development of a microscopic theory for the optical response in TMD's and specially the interaction between quasiparticles [207]. Specific quantum pathways can be probed through advanced spectroscopic techniques such as coherent multi-dimensional Fourier-transform spectroscopy [208,209]. Further, dynamics of this TX peak will also be discussed briefly in chapter 5, which corroborate the coherent nature of the TX peak.

Chapter 5: Formation Dynamics of Excitons and Trions in Transition Metal Dichalcogenides

EXCITON TO TRION FORMATION†

In the presence of residual charges, excitons interact with the surrounding free electrons, ultimately binding to electrons to form trions [63,210,211]. The ultrafast formation time for these quasiparticles has not been measured in TMDs. Yet, it is critical for evaluating and improving performance of optoelectronic devices based on this emerging class of materials [85,86,97,122,129,191,212-214]. Additionally, measuring ETF dynamics is an important fundamental problem due to distinct exciton and trion wavefunctions and properties. First, as we have discussed, trions can drift in an applied electric field [128]. Second, ETF is important for understanding exciton decay dynamics and the relative spectral weight of trions and excitons in photoluminescence [129,168].

As we have discussed in this dissertation, excitons and trions in monolayer TMDs are stable at room temperature due to the large binding energies of the order of a few hundred meV and tens of meV, respectively [85,86,91,121,122,129,215-217]. The exciton to trion formation (ETF) process is thermodynamically favorable due to lower energy of trion (c.f. exciton), leading to a characteristic trion wavefunction as shown in Figure 5.1. In the figure, the positions of a hole and an electron are fixed and chosen to be separated by 1 nm, corresponding approximately to the exciton Bohr radius for this material [218,219]. The probability to find a second electron is then calculated to be highest near the hole due

† This work was published in A. Singh, G. Moody, K. Tran, M. E. Scott, V. Overbeck, G. Berghäuser, J. Schaibley, E. J. Seifert, D. Pleskot, N. M. Gabor, J. Yan, D. G. Mandrus, M. Richter, E. Malic, X. Xu, and X. Li, *Trion formation dynamics in monolayer transition metal dichalcogenides*, Phys. Rev. B **93**, 041401(R) (2016). I (A. Singh) was responsible for experiments, data analysis and manuscript preparation.

to the attractive Coulomb force. The details of this calculation can be found in [159]. In the presence of a disordered potential, we anticipate the trion formation time to be modified. It will be thus interesting to study the effects of disorder on the formation time.

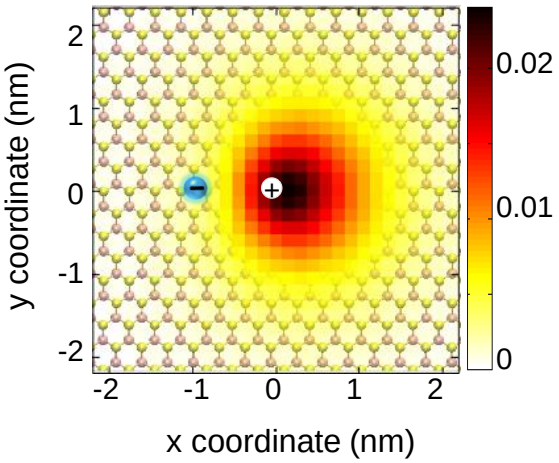

Figure 5.1: Calculated trion wave function in monolayer $MoSe_2$.

We again choose the two-color pump-probe spectroscopy method (described in chapter 3) to study the naturally n-doped monolayer MoSe2. The experimental details are similar to chapter 4 and are again illustrated in Figure 5.2. Here we concentrate on the XT peak, i.e. resonantly pumping the exciton and probing the trion transitions, in the two-color spectrum. We see the ETF process is manifested as a finite rise time τ_f in the differential reflectivity signal, as a function of the delay time between the two pulses [107,143,220,221]. As the pump energy is tuned through the inhomogeneously broadened exciton resonance, moving from high energy to low energy side, the trion formation time τ_f increases. An effective exciton "mobility edge" is suggested. A mobility edge can be described as the energy below (above) which the center of mass motion of the excitons is

localized (delocalized). Our measurements explain the role of disorder providing a more accurate picture of the complex quasiparticle dynamics present in TMDs [124,180,222] . Our studies also differentiate between different quasiparticle (exciton and trion) dynamics in these materials.

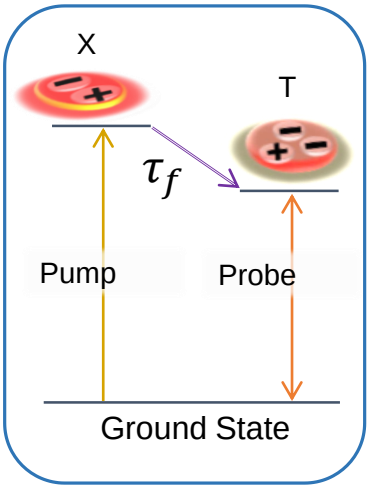

Figure 5.2: Schematic of XT excitation and detection scheme.

TWO-COLOR PUMP-PROBE SPECTRUM

The sample temperature is held at 13 K for all experiments to reduce phonon interaction induced resonance broadening. The narrow spectral linewidths in combination with large trion binding energy lead to spectrally well-resolved exciton and trion resonances in this high quality sample. For this experiment, we utilize ~ 0.7 nm (~ 1.5 ps) full-width at half-maximum (FWHM) pulses. These pulses are carefully chosen to get the necessary spectral resolution while still maintaining temporal resolution required to resolve the ultrafast dynamics. The pump and probe beams are collinear and are focused onto the sample with a spot size of ~ 2 μm. We use cross linearly polarized pump and

probe pulses to suppress pump pulse scatter reaching the detection optics. This ensures only probe detection on the detectors and having a clean measurement.

The diagonal peaks (XX, TT) in the two-color pump-probe spectrum (Figure 5.3) are associated with the trion and exciton resonances at 1631 meV and 1662 meV respectively. The diagonal line is shown with a dotted line. The spectrum is normalized so that the maximum of (absolute of) negative signal is set to 1. The cross-diagonal peaks (XT, TX) are related to exciton-trion coupling and conversion processes. This spectrum is similar to the spectrum discussed in chapter 4, however, the energies of the exciton and trion are shifted slightly. This occurs due to sample to sample variation. The energy separation between the trion and exciton (~ 31 meV), however, is the same (as in chapter 4) and agrees well with the trion binding energy from previous studies [129,223,224]. The line-shapes (absorptive or dispersive) of the different spectral peaks are due to the interplay between the relative phase of the reflected probe, the nonlinear signal and many-body effects as shown in the previous chapter [225]. For example, lineshape of the TX peak was studied in chapter 4 and attributed to coherent coupling between the exciton and trion.

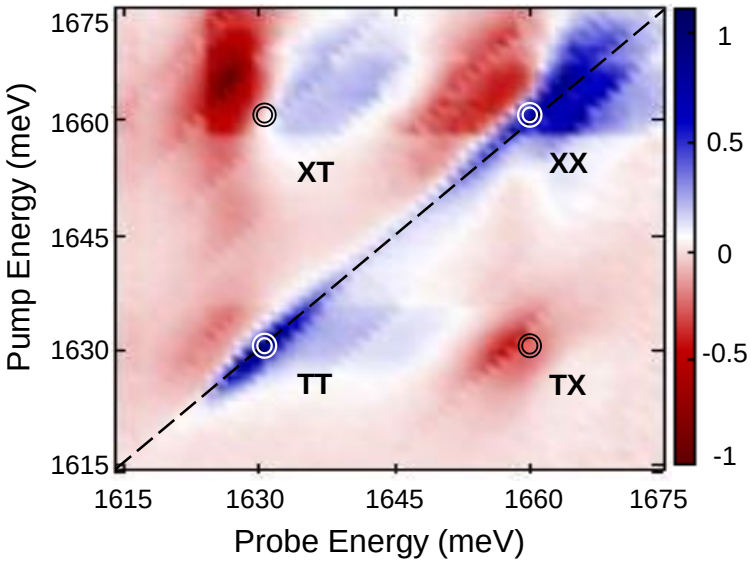

Figure 5.3: Two-color pump-probe spectrum on monolayer $MoSe_2$.

Our focus shifts to the quasiparticle ultrafast dynamics. We take delay scans (Figure 5.4) while pump and probe are tuned to measure each peak in the 2D map. The pump/probe energies chosen for each peak are indicated by the circles in Figure 5.3. Firstly, we look at resonant delay scans, i.e. pump and probe energies are chosen to be equal to the exciton (XX) and trion (TT) transition energies. The rise dynamics are ultrafast. This indicates that these quasiparticles form rapidly within the pulse width (~ 1 ps) and relax on the order of tens of picoseconds [124,193,226]. This evolution of dR/R signal is complicated and includes a change in sign as the delay time changes, which has been ascribed to higher order optical processes and/or energy renormalization in earlier studies [193,226]. Additionally, the slower decay of the TT signal compared to the XX signal suggests a longer relaxation time for trions consistent with earlier experiments [124].

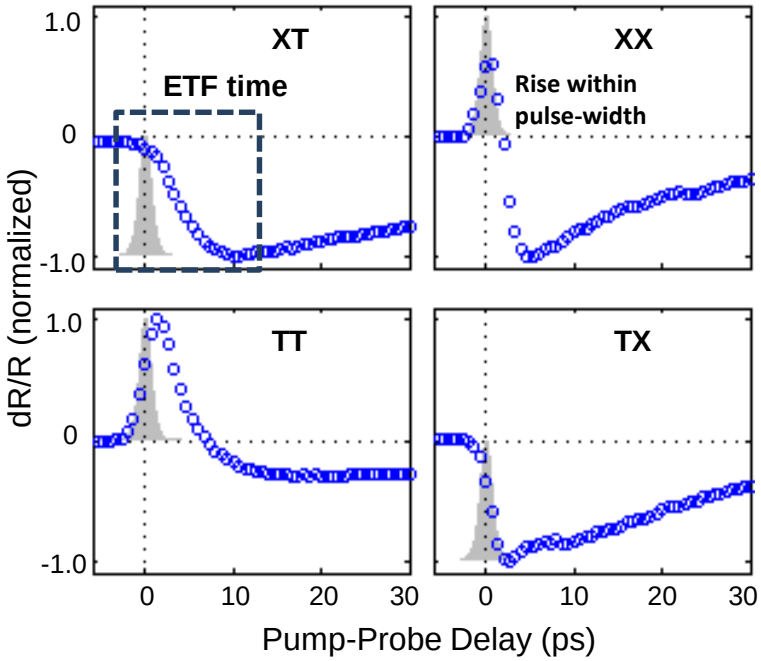

Figure 5.4: Delay scans for the four spectral peaks.

Further, considering the TX peak, i.e. pumping at the trion resonance and probing at the exciton resonance, we again see a fast rise in the dR/R signal, limited by the temporal resolution in our experiments. This ultrafast behavior is consistent with instantaneous coherent coupling between the exciton and trion as discussed in chapter 4. The trion to exciton (formation or relaxation) process is energetically unfavorable (the exciton is higher in energy by ~ 30 meV while kT ~ 1 meV). This points to coherent coupling processes being much more important than relaxation processes for the TX peak.

DYNAMICS OF THE XT PEAK

We focus now at the XT peak, i.e. pumping at the exciton resonance and probing at the trion resonance, which has distinctly different rise dynamics as can be clearly seen in Figure 5.4. In contrast to the other peaks, a finite rise time in dR/R signal, beyond the pulse temporal width was observed. As we have discussed, this finite rise time in the delay scan behavior indicates the ETF process [220,227]. We analyze this process in more detail by carefully choosing the pump and probe energies. The pump ($\hbar\omega_{pump}$) and probe ($\hbar\omega_{pr}$) energies are shown in Figure 5.5 overlaid with the degenerate spectral scan. We also fit lorentzian curves to the exciton and trion response. The curves are indicated by dotted lines and illustrate the slight overlap of the exciton and trion spectral responses in the energy range 1631 – 1660 meV. Thus, we choose the probe energy carefully to avoid this overlap region. We fix the probe to the lower energy side of the trion (1627 meV) to avoid measuring the exciton and trion resonances at the same time. Further, to improve the signal-to-noise, we integrate the differential reflectivity signal over different probe energies within a ±2 meV window, i.e. 1625 – 1629 meV. Pump-probe delay scans focusing on the initial rise dynamics of peak XT for two pump excitation energies are shown in Figure 5.5b. Interestingly, the rise dynamics are modified depending on the choice of the pump energy under the exciton resonance. The dynamics for the pump excitation at 1656 meV, are observed to have a slower rise to maximum dR/R signal compared to the delay scan corresponding to 1662 meV.

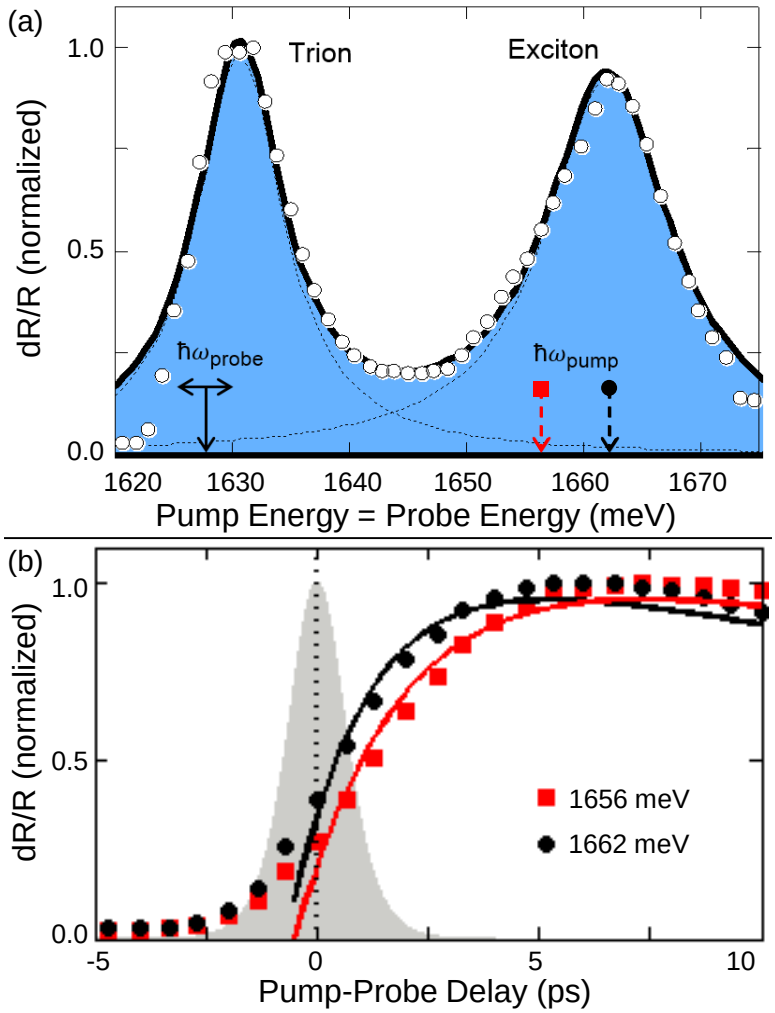

Figure 5.5: a) Degenerate pump-probe spectrum. b) Delay scans for two pump energies showing different rise behavior, indicated in (a).

To quantify these ETF dynamics and explore the pump energy dependence, we use a simple fitting function that takes in account both the rise and decay components associated with the ETF and trion relaxation processes, respectively,

$$dR/R \;=\; A_1\,[1 - A_2\,exp(-\Delta t/\tau_f)\,] \;\times\; exp(-\Delta t/t_d) \qquad (5.1)$$

, where A_1 and A_2 are fit amplitudes, τ_f is the trion formation time, and t_d is the trion relaxation time. In this model, we have assumed there is no pump energy dependence on the exciton formation. This assumption can be realized by near-instantaneous exciton formation, which is supported by the time evolution of the XX peak shown in Figure 5.4.

We measure a trion formation time τ_f = 1.6±0.1 ps from the fit to the data corresponding to pump excitation at 1662 meV (black dots in Figure 5.5b). A precise and direct comparison between different material systems is difficult due to different conditions under which experiments are conducted (e.g. doping density and excitation conditions). However, we strive to compare the formation time measured in this material with other physical systems. τ_f for ETF has been previously measured in different physical systems and contrasts from tens of picoseconds in GaAs and CdTe quantum-wells [73,107,227,228] to few femtoseconds in carbon nanotubes [220,221]. An intermediate trion formation time measured here is consistent with the a general scaling of the exciton properties in these different classes of materials [229]. In Table 5.1, we compare the exciton Bohr radius, trion binding energy and ETF times from three different groups of materials. We discern that the ETF time depends on the dimension of the physical system (1D, 2D) as well as the trion binding energy, which is determined by strength of the Coulomb interactions, which in turn depends the screening. The formation time decreases with increasing trion binding energy. Further, it is faster for lower dimension systems, due to a change in the nature of screening. The ETF time depends on several other factors, including excitation power, doping density, temperature, and exciton localization length. However, our comparison indicates that the order of magnitude of ETF time is governed by strength of the screened Coulomb interactions. It would be interesting now to explore the nature of the exciton states in a disordered potential.

Physical System	Exciton Bohr Radius, Dimension	Trion Binding Energy	Trion Formation Time
Carbon Nanotubes	1 nm, 1D system [230,231]	60- 130 meV [221,230]	60- 150 fs [220,221]
TMD ($MoSe_2$)	1 nm, 2D system [218]	30 meV [129]	2 ps (this study)
Quantum Wells (GaAs, CdTe)	15 nm, 2D system [232]	2, 3 meV [73,107,227]	100ps, 60 ps [73,107]

Table 5.1: Formation time dependence on physical system.

DISORDER AND MOBILITY EDGE

We show that measurements of the ETF time can actually characterize exciton localization. As we have discussed, this is important for applications involving quasiparticle transport and photoconductivity. By carefully changing the pump energy across the inhomogeneously broadened exciton resonance, we find that the trion formation time increases from 1.6 ps to 2.3 ps when moving from the high energy side to the low energy side. This pump energy dependence is shown in Figure 5.6. The dependence of ETF time on excitation energy is ascribed to the localization of center of mass motion of excitons in presence of disorder potentials. This disorder can be attributed to impurities, vacancies, or strain from the substrate. For example, strain has shown to change the spectral response in these materials [95,233]. Additionally, impurities and vacancies are known to change the properties of these surface sensitive materials [168,192]. Thus, it is interesting to study ETF to characterize this disorder and indicate the nature of exciton states present in the inhomogeneously broadened resonance.

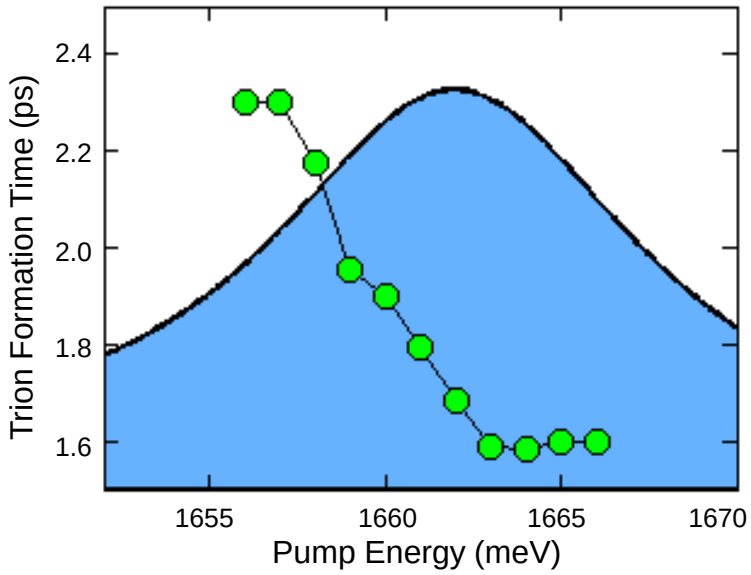

Figure 5.6: Trion formation time dependence on pump excitation energy.

We illustrate the effect of strength of disorder potentials on excitons in Figure 5.7. The strength of the disorder potential is indicated by a simple potential well, the depth indicating the disorder. For strong disorder associated with certain type of impurities and sample edges, an exciton may be strongly spatially localized. This type of strongly localized exciton has been seen in tungsten diselenide (WSe_2) recently. Careful photon emission experiments indicated quantum emitter nature of these strongly localized excitons [150-152]. Typically, these excitons are red-shifted tens of meV below the trion transition and thus do not interfere with our measurement. Thus, we do not probe these strongly localized states in our experiments performed under resonant excitation conditions.

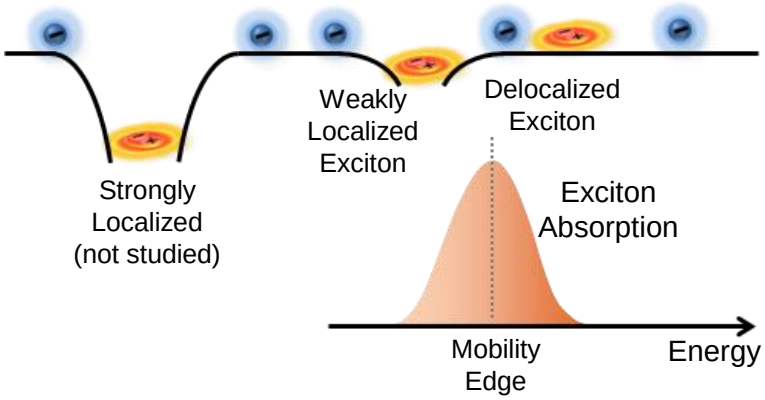

Figure 5.7: Illustration of disorder induced localization.

Kavokin realized that there could be excitons weakly localized by shallow disorder potentials as well [234]. The energy of these weakly localized states is only slightly red-shifted compared to the delocalized states, leading to inhomogeneous broadening of the exciton resonance. These states are illustrated in Figure 5.7. Thus, a measure of these states is important to characterize the nature of the inhomogeneous broadening. A "mobility edge" separates these two types of excitons in energy [72,228,234,235]. For energies above the mobility edge, the excitons are delocalized. The center-of-mass wavefunction of delocalized excitons extends across a large spatial region. This large extension increases the probability for this exciton to find a residual electron and form a trion [228], resulting in a faster ETF time for high energy excitons, as shown in Figure 5.6. On the other hand, the wavefunction of a localized exciton with energy below the mobility edge, is centered at a particular spatial location and decays away from it. This small in-plane localization of the exciton wavefunction causes a decrease of the exciton-free carrier interaction and results in a longer ETF time. While the concept of a mobility edge is theoretically hypothesized as a sharp energy that separates delocalized and localized states, the transition occurs across a spectral region

determined by the sample quality and disorder as observed in our experiments. We observe the mobility edge as an energy range of 3 – 4 meV. Further, this energy range is also governed by the homogenous linewidth of excitons, which is of the order of 2 meV for these materials [180].

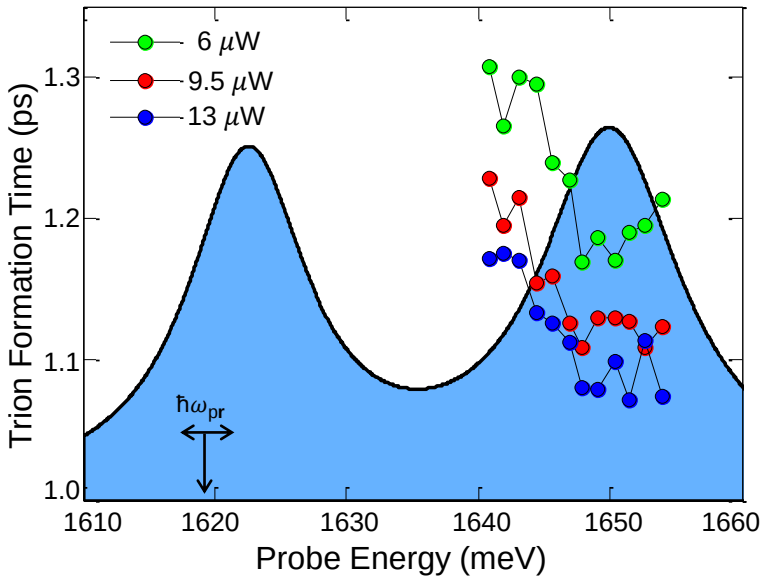

Figure 5.8: Formation time dependence on pump power.

We also investigate the ETF time dependence on pump power. The dependence is shown in Figure 5.8. These power dependence measurements were done on a different sample, and hence we see a spectrum shift. The energy difference between the exciton and trion, however, remains the same. We again see the ETF time behavior on pump energy and thus, the behavior is robust across different samples. Further, we see that the ETF time decreases for increasing pump excitation powers. This indicates the dependence of ETF time on the photo-generated exciton density. For a higher density of excitons, the probability of an exciton to find a background electron and form a trion increases. Another way to think about this power dependence is comparison with a

percolation random-walk problem. With increasing concentration of percolates, there is increasing flow through the system. Similarly, with increasing density of excitons, there is faster ETF.

The ultrafast ETF times reported here indicate that ETF process is an important pathway for exciton relaxation. Thus, ETF must be considered when interpreting ultrafast dynamics in time-resolved spectroscopy experiments concerning excitons. The existence of exciton mobility edge is particularly interesting as it is important for transport. This concept has remained unexplored in studies of quasiparticle transport in TMDs so far. We also stress that the underlying physical phenomena responsible for this mobility edge are fundamentally different in comparison to conventional quasi-2D quantum wells such as GaAs. The mobility edge in (high quality) GaAs quantum wells was attributed to well width fluctuations, a mechanism that cannot be responsible for disorder in these monolayer semiconductors. We have also measured a Stokes shift in these materials (few meV, data not shown). Stokes shift, an energy difference between spectral response measured in PL and absorption, indicates the presence of disorder. Future transport experiments combining high spectral resolution and high spatial resolution will be useful to characterize the nature of this disorder and even a way to improve the material purity [204,236].

Chapter 6: Spin-Valley measurements in TMDs'

INTRODUCTION

In chapter 4 and chapter 5, we have discussed the strong exciton – trion interactions and their dynamics. The interactions are an order of magnitude stronger than traditional semiconductors like gallium arsenide. The dynamics studied were ultrafast and result in interesting physics. But this is not the only reason why study of TMDs' is exciting.

There is a huge interest in these materials due to the possibility of spin-valley coupling [94]. The physical reason, as we discussed in chapter 2, is the location of the direct gap in the momentum space, finite momentum point K or K' (-K). These opposite momentum points are degenerate but have opposite spins, and consequently result in spin-valley coupling. Further, the valence band is spin-split, with the separation being ~ 200 - 400 meV. The spin scattering is therefore either momentum or energy forbidden. This results in large spin polarization for these materials, even for non-resonant excitation [93,108,109]. Note that the structure of the conduction band is still under intense debate and has different behavior for different materials. For example, in MS_2 (M = tungsten, molybdenum) the lowest energy transition is the bright exciton, while in MSe_2 the order is thought to be reversed, resulting in the lowest energy transition being non-radiative [237,238].

For this chapter, we specifically choose the material tungsten diselenide, WSe_2. The valence band has large spin splitting (~ 400 meV), which is the largest in the family of TMDs' [215]. Consequently, this material presents large spin polarization in time-integrated photoluminescence (PL) experiments, even for non-resonant excitation ~ 200 meV away [124]. WSe_2 has demonstrated applications in chiral light emitting diodes which will be interesting in lighting applications [101]. Further, quantum emitters have

also been observed in this material [150,151]. Thus WSe_2 could be a candidate for spin-qubit hosting material. Further, optical resonances in WSe2 have shown to be well separated and sharp. Interestingly, for $MoSe_2$ which also has sharp and well separated optical transitions (studied in chapter 4 and chapter 5), the spin polarization measured in time-integrated PL experiments is very small [223]. The reasons behind this behavior for $MoSe_2$ are under active discussion but not yet resolved [239]. Thus, WSe_2 is the ideal material to measure the strong spin-valley phenomena in TMDs' and the focus of this chapter.

Measuring the spin dynamics in TMDs' are an exciting field, with experiments utilizing kerr-rotation, spin-noise spectroscopy and time-resolved PL. These experiments present a range of time-scales, from ~ 100 fs to ~ 5 ps [124,195,240,241]. These studies are a natural extension of physics demonstrated in quantum wells, applied to these strongly interacting materials. Phase space filling, band-gap renormalization and exciton-exciton annihilation are some of the processes that have invoked to explain the complex dynamics in these materials [226,242]. The signal measured in these experiments have complicated lineshapes (spectral) and change sign as a function of time. Thus, it is important to measure dynamics in transmission geometry, to make the analysis simpler and cleaner, and to not worry about the relative phase between signal field and probe field. Further, transmission geometry also enhances the signal-to-noise ratio due to non-absorption of probe by substrate.

In this chapter, we measure spin dynamics on a monolayer WSe_2 sample, utilizing a modified spin sensitive two-color pump-probe (TCPP) experiment. Transmission geometry is employed to simplify line-shape analysis and assign physical reasons behind the observed dynamics. We measure ultrafast exciton spin-valley relaxation with residual spin polarization relaxing in ~ 5 ps. On the other hand, trion spin-valley polarization is

longer lived (~ 15 ps). An interesting negative feature is observed near the exciton resonance, with an enhanced optical signature for cross-circularly polarized probe. We assign this feature to biexcitonic transitions.

SAMPLE CHARACTERIZATION AND SETUP DETAILS

A mechanically exfoliated monolayer WSe_2 on a transparent sapphire substrate is used in this experiment. The flake is exfoliated from a commercially available bulk WSe_2 crystal (2D-semiconductors) and is identified through optical contrast and room temperature PL. The sample is cooled to ~ 13 K in the closed loop cryostat to reduce phonon-related effects. PL is measured using a 2.33 eV (532 nm) laser and presented in Figure 6.1. The PL clearly shows well separated exciton (~ 1753 meV) and trion (1719) spectral peaks, along with an impurity peaks (~ 1680 meV). The trion binding energy ~ 34 meV, and the spectral positions of the exciton and trion peaks, are consistent with previous studies [124,148,243].

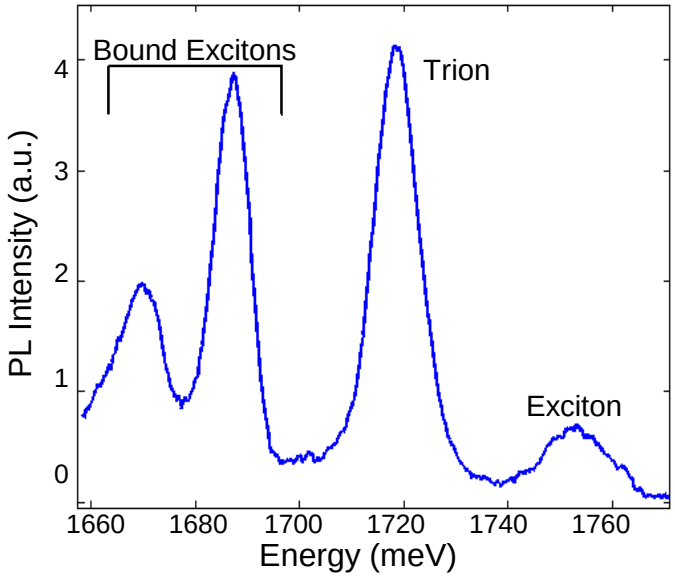

Figure 6.1: PL measured at 13K on a monolayer WSe_2 sample.

The quasiparticle dynamics can be measured through degenerate pump-probe (PP) spectroscopy, as described in chapter 4 and chapter 5. Briefly, pump and probe pulses are tuned through the quasiparticle resonances, with pump-probe relative delay controllable through a mechanical delay stage. The pump and probe pulses are cross linearly polarized, with pump being blocked in the detection path through a crossed polarizer.

For measuring the spin dynamics of the excitons and trions, we utilize a modified TCPP setup which is spin-sensitive. The details of the setup are shown in Figure 6.2. The setup works in transmission geometry. Firstly, the pump and probe pulses are linearly polarized through separate linear polarizers (to clean up the polarization). A quarter wave plate (QWP), kept just before the microscope objective, converts the polarization to circularly polarized pulses. The purity of circular polarization and linear polarization is stressed here. For this experiment, polarization insensitive cube beam-splitters are used. The pump linear polarization can be rotated to the same (or orthogonal) direction as the probe polarizer, to get the same (or opposite) circularly polarization as the probe. The circularly polarized pump and same (or opposite) circularly polarized probe are sent to the sample and focused via the 50-X microscope objective, to get a small spot size (~ 2 μm). The polarization after the 50-X objective is also monitored, and is still pure (clean). This is an important check to enable measurements of sensitive spin phenomena. The pump and probe pulses interact with the sample, and pass through it. Subsequently, these pass through a spectrometer, which spectrally filters the pump, and only allows the probe through. This spectral filtering allows pump wavelengths as close as ~ 1 nm to the probe wavelength. The reason behind changing the polarization of the pump, rather than the probe, is related to detection. By keeping the probe polarization fixed, we make sure that the setup is insensitive to changes in probe detection caused by polarization sensitive

optical components (spectrometer gratings, beam splitters). Thus, the setup is optimized to measure complex spin phenomena of the different quasiparticles.

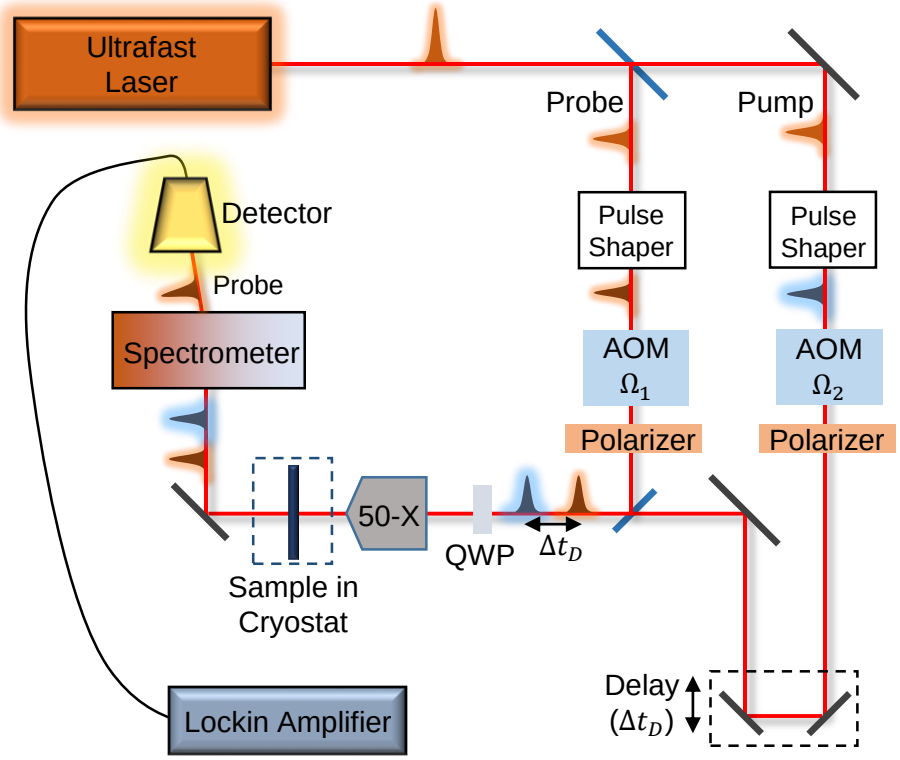

Figure 6.2: Spin-sensitive TCPP setup.

First, we measure the dynamics of the quasiparticles, without any spin information. The differential transmission signal, for different time delays, is presented in Figure 6.3. The signal is normalized for the maximum to 1. The exciton and trion peaks are measured at 1754 meV and 1721 meV respectively. Note that the signal beyond 1760 meV is too small to measure and quite noisy. Additionally, there is a very small stokes shift between the PL and PP, which signifies the high quality of the material. The exciton PP signal is much enhanced compared to trion. Interestingly, the situation is reversed from PL. This can be thought of lower lying transitions (trion) usually showing larger PL

and the higher oscillator strength of excitons resulting in larger PP signals. The time delays are chosen to present dynamics at short (< 5 ps) and long (~ 30 ps) time delays. At negative delays, the PP signal is zero, which is expected. As the time delay is increased, the exciton and trion peaks decay, and shift to higher energies. Further, a negative feature develops near the low energy side of the exciton. Importantly, the usage of transmission geometry means we can directly translate the differential transmission signal to absorption. Thus, a negative feature means enhanced absorption of the probe (due to the pump), whereas a positive feature relates to reduced absorption of probe. Even in transmission geometry, the signal has negative components which are related to energy shifts and bandgap renormalization [195,225,226,242,244]. Interestingly, the negative feature increases with increasing time delays, for delays < 10 ps, after which this feature decreases. We discuss this feature later in the chapter, with circularly polarized pulses. Further, from Figure 6.3, exciton and trion decay at a time scale of ~ 10 ps. Note, that the pulse duration is ~ 1 ps, so we are not sensitive to dynamics occurring at ~ 100 fs scale [180,195].

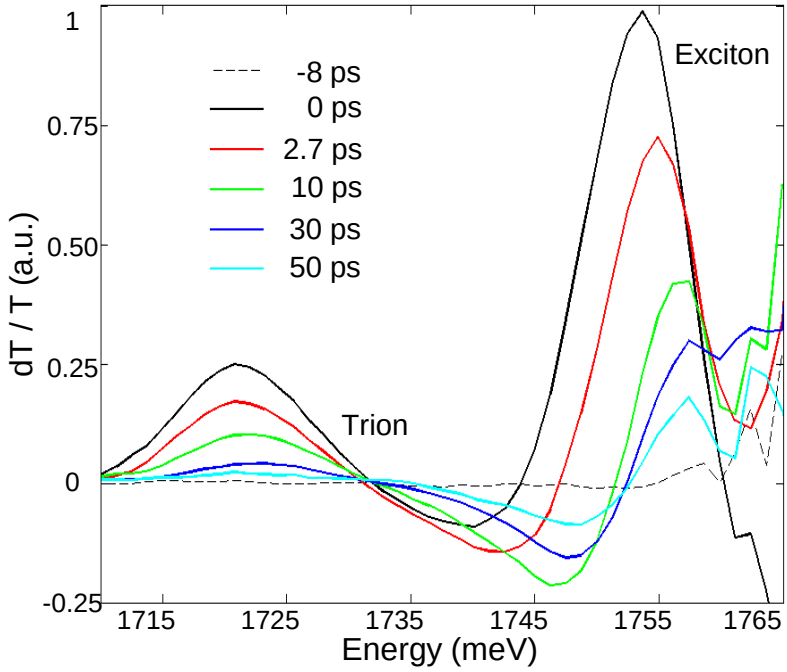

Figure 6.3: Degenerate PP for different time delays.

SPIN-SENSITIVE TWO-COLOR PUMP-PROBE

To analyze the spin characteristics of the quasiparticles, we now switch to the spin-resolved TCPP, as illustrated in Figure 6.2. The advantage of using spin sensitive TCPP is that we can distinguish between processes in different valleys in TMDs'. This is due to the spin-valley coupling in TMDs'. We generate a spin-sensitive TCPP spectrum, for both co and cross circularly polarized pump and probe pulses. The spectra for time delay ~ 0.7 ps, is illustrated in Figure 6.4. A diagonal line is drawn to illustrate points for which pump and probe are degenerate. The geometry of detection forces us to ignore the data on the diagonal line, since the pump also enters the detector when the pump and probe are degenerate. Note in figure 6.4, each data point is represented by a pixel, for which pump and probe energies are separate. We plot each data point independently, and without interpolation between neighboring points, so that the data on the diagonal line

does not influence the neighboring points. We also use a slightly saturated color-bar to enhance contrast for the TT peak (the units for the color-bar are arbitrary units).

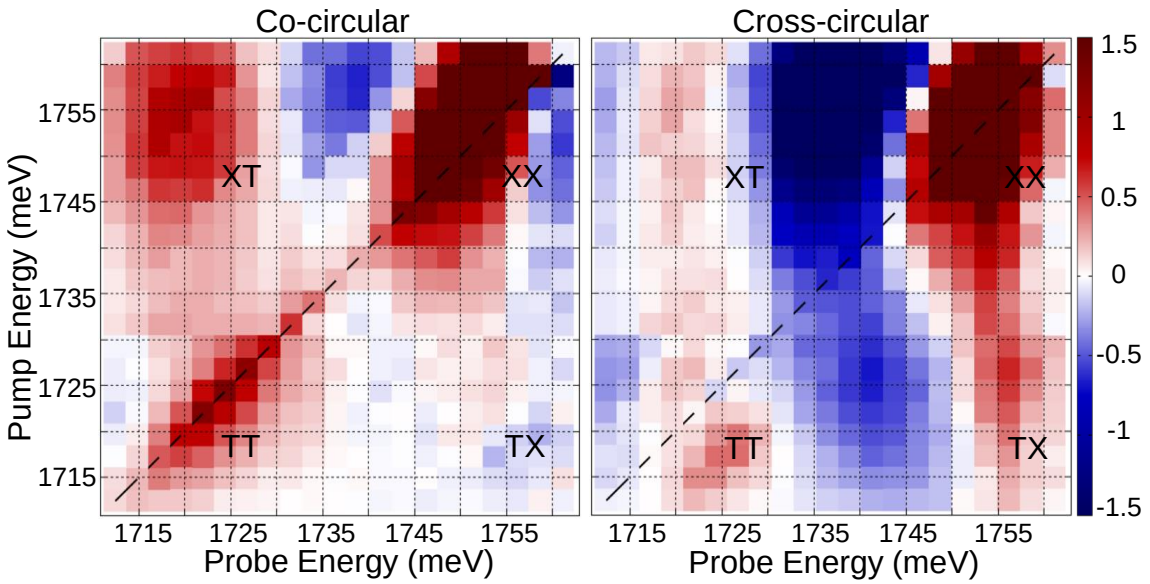

Figure 6.4: Co and cross circularly polarized TCPP spectra. The data is taken at delay ~ 0.7 ps.

A delay ~ 0.7 ps is chosen in Figure 6.4, to illustrate the different physical processes measured by co and cross circularly polarized pulses, just after (pump and probe) pulse overlap. A number of observations are in order. The naming of the spectral peaks in Figure 6.4, follow the same convention as in chapter 4 and chapter 5. The XT peak is much enhanced for co-circular polarization, compared to cross-circular which relates to efficient spin transfer from exciton to trion. The XX peak has both positive and negative features. The positive features are similar for the co and cross cases, signifying inefficient exciton initialization. Interestingly, the negative feature near the exciton (for both exciton and trion pumping), is pronounced for cross-circular circular polarization while it is not present for co-circular polarizations. Due to this unique polarization dependence, we assign it to biexcitonic transitions. Note that in TMDs' due to spin-valley

coupling, biexcitons are of inter-valley character, resulting in increased absorption for cross-circularly polarized probe. The TT peak is much enhanced for co-circular case, signifying efficient and stable polarization. The TX peak, on the other hand, has a higher signal for cross-polarized pump and probe. This signal may be related to blue shift of exciton energy level, due to the trion. However the polarization dependence of TX peak is intriguing, probably relating to coupled biexciton and trion states.

We now focus on the spectra, close to the diagonal, for both excitons and trions. Pump energies are chosen quasi-resonant (~ 2 meV away) with the probe, since we cannot look directly at resonance. The line-cut for this spectra is shown in Figure 6.5. The trion is very efficiently initialized in a particular valley, with almost no signal for cross-polarized probe. The exciton, on the other hand, shows small differences between co and cross polarization illustrating small valley polarization. This shows rapid scattering of the exciton to the other valley, while trion suffers less scattering and has larger spin polarization. Again, note the pronounced signal around ~ 1740 meV, for cross-polarized pump and probe. This polarization dependence supports the assignment of peak to the biexcitonic transition. Negative features, as we have discussed, can also arise from energy shifts but these could be similar for co and cross. The difference between co and cross circular polarization signals, is important here for the assignment to the biexciton.

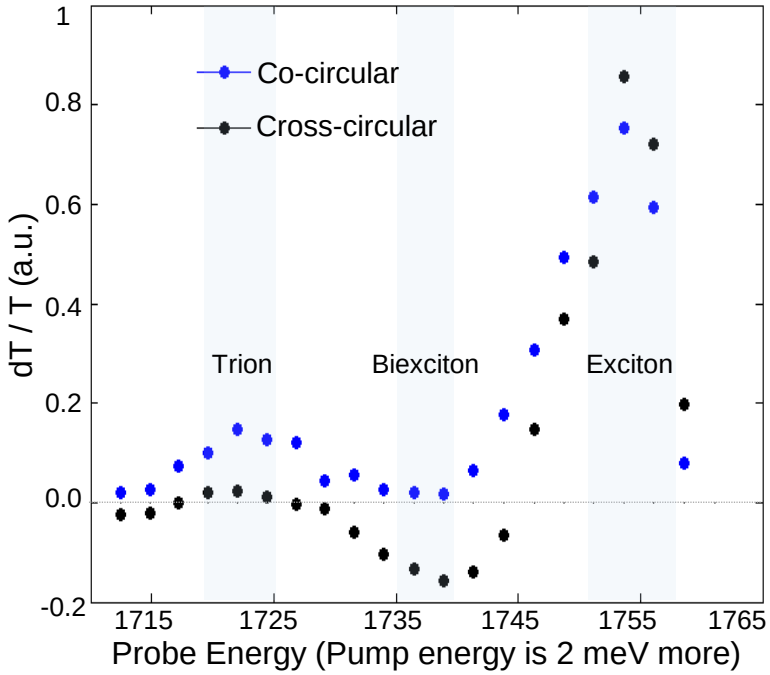

Figure 6.5: Quasi-resonant co and circularly polarized PP spectra.

Investigating the valley-dynamics of excitons, trions and biexcitons is in order. To increase signal to noise, as well as reduce effects of energy shifts, we integrate the PP signal for a range of probe energies (quasi-resonant with exciton). The range of the integrated data for the three resonances is illustrated in Figure 6.5. The spin-valley polarization data is presented in Figure 6.6. The key parameter defined here is the degree of circular polarization

$$CP = \frac{Co - Cross}{Co + Cross} \tag{6.1}$$

, where co (cross) is the situation for which pump and probe are co-circularly (cross-circularly) polarized. The CP as defined in equation 6.1, is used to define the degree of spin (valley) polarization in PL experiments [93,223]. Note that in this experiment, due to

negative and positive PP signals, CP can also be negative. We use CP as a parameter to discuss the spin-valley relaxation processes, but extracting time-scales via fits is not done here. The initial CP (around small time delays) is quite small, and then changes sign. The residual CP decays within ~ 5 ps. The biexciton CP is negative illustrating dominance of cross-circular polarized signal (over co-polarized signal). For biexciton, the CP decays rapidly within ~ 5 ps, similar to time-scales of the exciton. The trion CP is positive for all time delays and persists for more than ~ 15 ps. Thus, trion spin-valley polarization persists for much longer time scales than excitons, as seen in earlier experiments also [124,245].

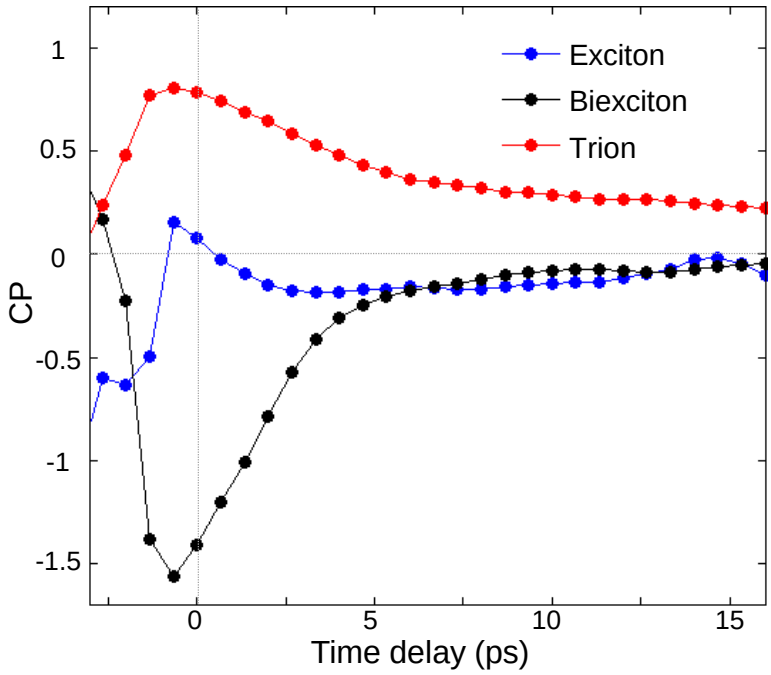

Figure 6.6: Degree of circular polarization for exciton, biexciton and trion, as a function of time delay.

The excitation (pump) energy dependence of the transitions is now expanded beyond the quasi-resonant scheme. The study can shed light on relaxation and coupling

behavior, as we observed in chapter 5. Measurements for pumping at exciton (~ 1756 meV), biexciton (~ 1739 meV) and trion (~ 1724.4 meV) energies, are presented in Figure 6.7. Again, due to geometry of pump we neglect the data point for degenerate pump probe, and illustrate the position of the pump energy with the grey region in the figure. The biexciton feature is much enhanced, when pumping at exciton compared to resonant pumping of the biexciton. This pump energy dependence of the negative feature is another evidence of the biexcitonic nature of this feature. For pumping at the exciton, the trion has higher signal for the co circular case, as we also saw while analyzing the XT peak in Figure 6.4. For pumping at biexciton, there is small signal at the exciton, but there is no observable trend. When the pump energy is tuned to the trion, interestingly, there is enhanced response at the cross-circular case, as also observed for peak TX in Figure 6.4. When probing at trion energies (and nearly resonant pumping at trion), the co-circular case is enhanced, illustrating efficient valley initialization for trion when resonantly pumped.

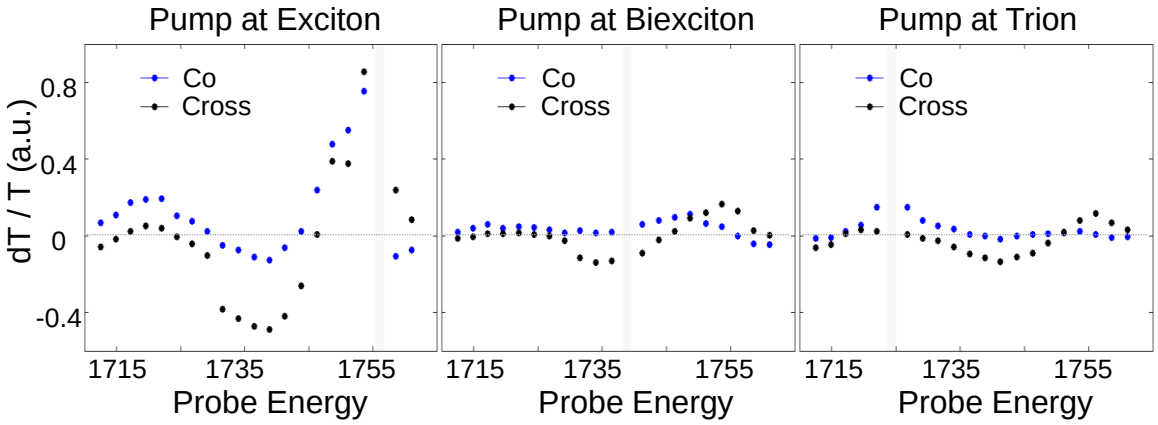

Figure 6.7: Pump energy dependence on the probe signal for co and cross-circular pump and probe.

Biexcitons have been found for a number of TMD systems including MoS_2, WS_2 and WSe_2 [196,246,247]. The biexcitons were observed through PL and characterized through power measurements. However, the biexciton binding energy for all these systems was identified of the order of ~ 50 meV. On the other hand, there is theoretical work discussing the possibility of biexcitons at an energy higher than trion and on the lower energy side of exciton [248,249]. Another theoretical work calculated binding energies of biexcitons in this material (WSe_2) ~ 20 meV, similar to ~ 17 meV we measured in this work. This agreement is indeed encouraging. The higher biexciton binding energies measured for WSe_2 in [246] could possibly due to first excited state of biexciton, as explained in [248]. Indeed for this material, for which screening is drastically reduced and non-local effects are important, work in [250] emphasizes the order (in energy) of observations in PL should be trions, biexcitons and excitons. Thus the theoretical evidence behind our observations is encouraging.

In summary, we have measured exciton and trion dynamics in a systematic manner on a monolayer WSe_2 sample. We measured longer lived trion spin (valley) polarization and a fast exciton spin (valley) scattering. A negative feature on the lower energy side was attributed to biexciton creation, and supported by polarization behavior and dynamics of spin polarization. The trion spin (valley) is efficiently initialized when resonant pumping at trion as well as exciton, and persists for more than 15 ps.

Chapter 7: Spin Polarization of Excitons and Trions in Gated Quantum Wells

INTRODUCTION

In this chapter we focus on the spin dynamics of gallium arsenide (GaAs) quantum wells (QWs'). We have thus far studied the dynamics of TMDs' and the strong exciton-trion correlations in TMD materials. However in GaAs QWs', the correlations are an order of magnitude weaker due to increased screening. The field lines are confined in the active layer or pass through the confining (barrier) layers, which have larger dielectric constants than air (and hence more screening). Also, the quantum confinement is weaker in QWs' compared to monolayer TMDs'. However, the mobility in QWs' is much higher compared to current state of the art TMD materials. The spin lifetimes of excitons in QWs' is also higher (than current TMDs') due to reduced impurity scattering events. Thus, these provide an ideal test bed to study the effect of electric and magnetic fields on excitons and trions. Additionally, the effect of these fields on the background electron gas can also be measured in QWs'.

Spin phenomenon in quantum wells including spin coherence, relaxation and transfer, have been extensively studied [81,125,141]. The basic experimental idea is the initialization of a non-equilibrium distribution of angular moments by optical excitation. These angular moments can be free carriers (electrons, holes), bosonic quasiparticles (excitons) or composite fermionic quasiparticles (trions). The distribution of these angular momenta can be modified with applied electric and magnetic fields, revealing spin structures in the quantum wells. The distribution can be studied by a variety of techniques including luminescence polarization, kerr rotation and spin-noise spectroscopy. In this chapter, we concentrate on GaAs QWs', which have higher exciton

(and carrier) spin lifetimes than CdTe QWs' (50 ps for GaAs compared to ~ 15 ps for CdTe) [107,251].

The spin structure in GaAs QWs' is much different than bulk GaAs. The valence band in GaAs QWs' is spin-split, with the heavy-hole – light-hole degeneracy being broken (c.f. bulk), as we discussed in chapter 3 [81,139,140]. The heavy hole has a projection of its orbital momentum l on the direction of helicity equal to ± 1, while the light-hole has a projection of 0. This difference in l has consequences on optical selection rules, thus heavy (light) hole bands can be excited with $\sigma +$ ($\sigma -$) light. The breaking of degeneracy has consequences for larger hole spin lifetimes in quantum wells c.f. bulk GaAs (5 ps vs 100 fs). The electron spin, however, has a smaller spin lifetime due to additional spin scattering processes [80,252,253].

Interesting quantum phenomena relating to trion and exciton transitions can be seen in quantum wells through modulation doping (delta-doping) [254]. This method of doping preserves high electron mobilities in the active quantum well layer and provides gate dependent tuning between excitons and trions. The mobility argument is especially true for wide quantum wells, whose transport properties suffer very little due to monolayer fluctuations, intrinsic to MBE fabrication. Further, trions in these wide high-mobility QWs' have shown the ability to drift in an applied lateral electric field [128]. However, the spin mechanisms concerning trions in these wide quantum wells have not been well studied. These trions are mobile, different from localized trions mostly studied in narrow quantum wells and dots. Trions, which have higher spin lifetimes than excitons in quantum wells and TMDs', offer a different paradigm for spin-qubits as building blocks for computation [107,124].

Importantly, trions have shown to efficiently initialize the two-dimensional electron gas (2DEG) in quantum wells. This behavior was also shown recently in other

two-dimensional materials exemplified by TMDs' [255,256]. The 2DEG is a semi-metallic density of electrons which can be induced in a quantum well, and controlled via a back-gate. The density can be tuned and the characteristics changed from metallic to insulating [211]. This metal to insulator transition (in QW) is important since within this regime, excitons and trions can be observed. Further, at higher density of 2DEG, the QW can be used as a channel for transistors. Additionally, the measurements of the 2DEG are technologically important due to large (~ 1 ns) spin lifetimes of the electrons in 2DEG. These electrons can be used in spintronic applications. The ability to control the relative density of excitons and trions is a valuable tool to study the effect on the 2DEG when excitons, trions or both simultaneously, are present in the system.

These gated high mobility wells can bring forth an interplay of various spin depolarization mechanisms. Applied (vertical) electric fields can change the exciton spin decay times by changing the electron-hole overlap, thus giving us a tuning knob over exciton related spin decay mechanisms including exciton-exchange interaction. The presence of trions provides a possibility to study exciton-trion complexes. Further, by applying a lateral field, we can study momentum dependent spin depolarization mechanisms exemplified by Dyakanov-Perel and Elliott-Yafet mechanisms, where momentum relaxation is accompanied by spin relaxation due to spin-orbit coupling. By applying a magnetic field, g-factors of electrons, excitons and trions can be studied separately, which shed light on the magnetic moments of these free carriers and quasiparticles. The studies of mobile trions can also be extended towards the trion spin-hall effect, via a mutual transformation of spin and charge currents. The high mobility offers a route towards using these QWs' as channels for spin carriers for logic applications.

The focus of this chapter is a gated 20 nm wide GaAs QW, fabricated via molecular beam epitaxy (MBE). In this chapter, we utilize two-color kerr rotation spectroscopy to measure spin dynamics of excitons, trions and the 2DEG. We will measure the electron g-factors by utilizing magnetic fields applied in the Voigt geometry (in-plane). We will also measure spin decay times for excitons and trions as a function of gate voltage, and the transfer of spin to the 2DEG via excitation at exciton or trion energies. This will reveal the interplay of exciton, trion and 2DEG and the relevant spin depolarization mechanisms. Further, we find an interesting spin lifetime enhancement of the 2DEG when excitons and trions are both present in the system.

SAMPLE DETAILS AND TWO-COLOR KERR-ROTATION PUMP-PROBE

We utilize a modulation doped QW, with the structure as shown in Figure 7.1. The substrate is n-doped GaAs, which is conductive and is useful for back-gating. Briefly, the hetero-structure consists of multiple GaAs/AlGaAs (3nm/10nm) QWs', a 20 nm GaAs QW with AlGaAs barrier layers and Si-delta doping with sheet density ~ 4e12 cm^{-2} at a distance of 96 nm (spacer width) from the QW layer. Silicon acts as a n-dopant in GaAs and AlGaAs [254,257]. There is another delta-doping layer close to the surface (density ~ 1e12 cm^{-2}) which is necessary to reduce strong electric field created by the surface state (of the hetero-structure). The delta-doped layers are magnified in the structure illustrated in Figure 7.1 for ease of viewing, however, they are of infinitesimal thickness. The sample is processed into a standard hall-bar geometry with six ohmic contacts (deposited on top of the hetero-structure), made of AuGeNi alloy (Gold-Germanium-Nickel). The width of the hall bar is 20 μm, and the surrounding regions are chemically etched away. Subsequent annealing is important to get good ohmic contacts between the QW and the metal pads deposited on top of the hetero-structure.

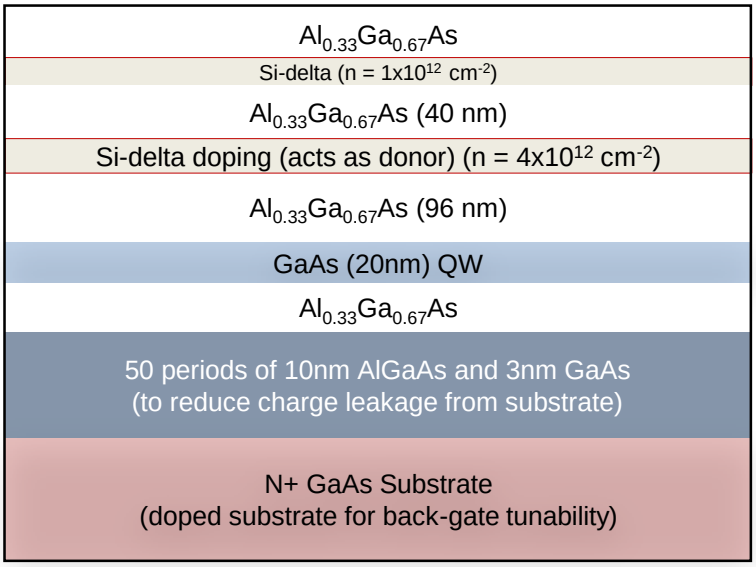

Figure 7.1: Details of QW structure under study.

The trion binding energies in these samples is expected to be ~ 1 meV, and thus they can-not be observed at temperatures (T) more than ~ 10 – 15 K (1 meV ~ 12 K). Thermal energy at T > 10K is enough to disassociate these loosely bound trions (compared to 30 meV for TMDs'). Interestingly, pump-probe signatures of trions are still visible even at T ~ 30 K (data not shown), though greatly reduced from T ~ 10 K. Thus, these samples are cooled down to temperatures ~ 4 K, in a liquid Helium-flow cryostat, to enhance the trion transition probability and optical signal.

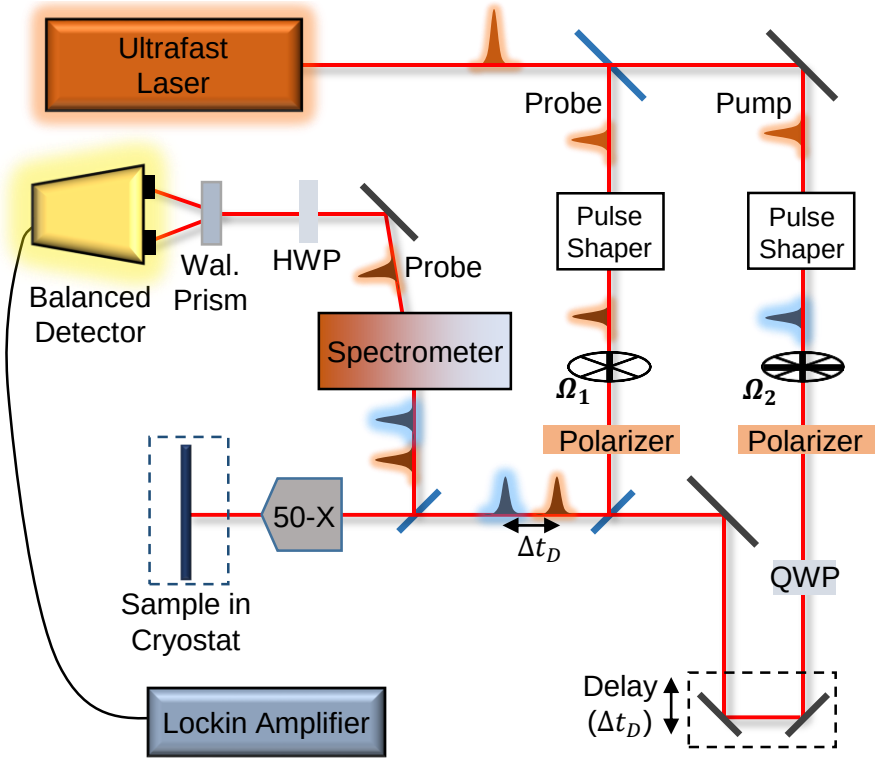

Figure 7.2: Detailed two-color kerr-rotation setup.

For measuring the dynamics of the quasiparticles, we utilize a two-color kerr-rotation pump-probe spectroscopy. The details of the setup are shown in Figure 7.2. This is a variation of the two-color pump-probe setup used in chapter 4. The Ti-Sapph laser is tuned to the wavelength range 1.49 - 1.54 eV (790 – 830 nm) for resonant probing of excitons and trions. The AOMs' are replaced by mechanical choppers in this particular experiment. The setup works in reflection geometry (similar to chapter 4 and 5) due to non-transparent (electrical) chip carrier on which the sample is mounted. The pump is linearly polarized through a linear polarizer (to clean up the polarization), and subsequently circularly polarized through a quarter wave plate (QWP), inserted after the linear polarizer. The probe is linearly polarized in the same (or orthogonal) direction as the pump polarizer. The circularly polarized pump and linearly polarized probe are sent

to the sample and focused via a microscope objective to get a small spot size (~ 2 μm). Both of the pulses are reflected from the sample and passed through a spectrometer. The spectrometer spectrally filters the pump, and only allows the probe through. Through this spectral filtering, pump wavelength as close as ~ 1 nm, to the probe wavelength, can be achieved enabling quasi-resonant spin measurements. This is important because above band excitation destroys the spin-polarization in quantum wells [81,251]. Also, the efficient spectral filtering enables us to measure the effect of excitation energy on spin lifetimes of the different quasiparticles. The linearly polarized probe pulse then passes through a half wave plate (HWP) and a Wollaston prism (Wal prism). The two linearly polarized beams coming from this sub-assembly of HWP and Wal prism (which correspond to the two circular polarizations at the sample) are sent to two arms of a balanced detector, which are balanced when the pump is off. When the pump is switched on, a change in the balanced detector signal corresponds to a rotation of the probe and a non-equilibrium spin population (imbalance in equal spin populations) in the QW system. Additionally, an-plane magnetic field can also be introduced enabling experiments in the Voigt geometry.

Photoluminescence (PL), with a 1.96 eV (632 nm) excitation laser, is used to characterize the exciton and trion transitions as function of back-gate voltage. Similar spectra is measured with 1.57 eV laser, which is below the barrier layer gap. One of the top ohmic contacts is grounded and subsequent tuning of the back-gate voltage can induce electrons from the delta-doped layer (the delta-doped layer closest to QW) into the QW. The PL spectrum as a function of back-gate voltage, is shown in Figure 7.3. The PL spectra, for different voltages, are offset (y-axis) for clarity. As the voltage is increased from -3V to +1V, more electrons are induced in the quantum well. The 0V spectra clearly shows well separated exciton (X) and trion (T) peaks. The other two weaker peaks are the

bulk GaAs luminescence (B), and the light-hole (LH). We concentrate on the X and T peaks in this chapter. Lower voltage (back-gate voltage, $V_B < -0.5V$) shows overlapping spectral responses of X and T. The energy separation (binding energy of trion) is lowest for -3V and increases steadily as the voltage is increased. This is similar to behavior seen in similarly prepared samples, and is a signature of the Fermi level shift with increasing density of electrons in the quantum well [258]. Similar measurements have also been repeated in TMDs', thus demonstrating again the general equivalence of quasiparticle physics in QWs' and TMDs' [122].

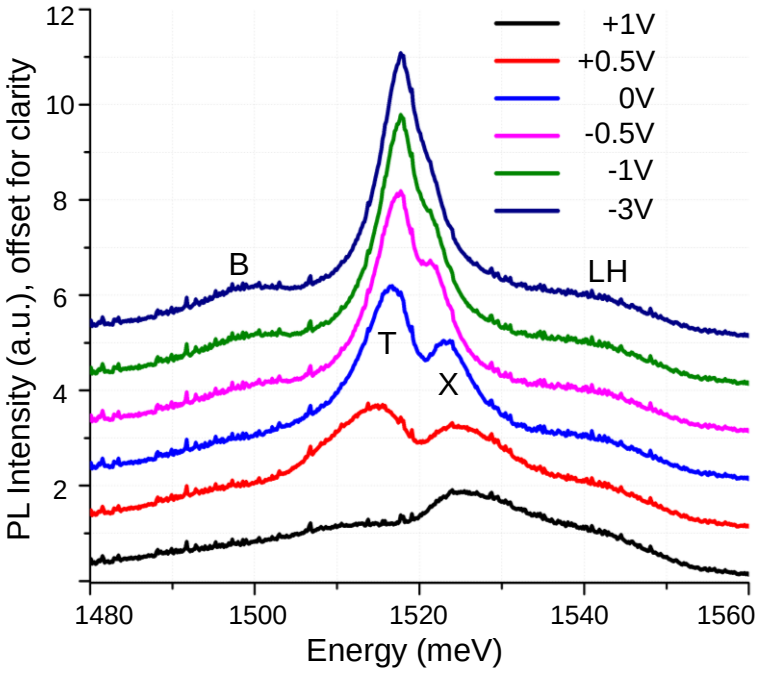

Figure 7.3: Back-gate voltage dependent PL spectra.

After identifying X and T resonances in this gated quantum well, we shift our focus to measuring the dynamics of these materials. We utilize pump-probe to measure the decay dynamics of exciton and trion. The pump is fixed at 1540 meV and the probe is varied across the trion and exciton resonances. The pump and probe are linearly polarized

and the pump is rejected through spectral filtering. The trion (exciton) is measured at a voltage of V_B = -0.5 V (0 V) and a decay time ~ 150 ps (100 ps) is extracted (data not shown).

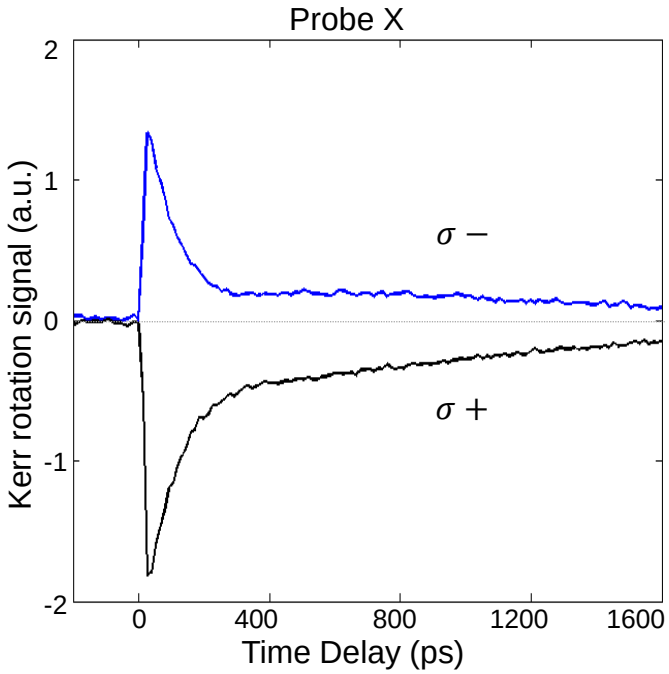

Figure 7.4: Kerr rotation measurements with probe tuned to exciton transition.

The spin dynamics of excitons and trions are measured through kerr-rotation. The pump is again fixed at 1540 meV, and probe is selectively tuned to exciton (V_B = 0 V, 1524 meV) and trion (V_B = -0.5 V, 1517 meV) transitions. The measurements for exciton is illustrated, for $\sigma+$ and $\sigma-$ pump, and linearly polarized probe, in Figure 7.4. As can be seen, the sign of the signal reverses upon change of the helicity of the pump polarization. This reversal of sign demonstrates we are measuring kerr-rotation signal correctly [229]. Further, we can enhance signal-to-noise and reduce background effects by subtracting the signals for $\sigma-$ (left circularly polarized, LCP) and $\sigma+$ (right circularly polarized, RCP) pump helicities. Note that this is standard practice in kerr-

rotation spectroscopy. The subsequent spin-decay curves are shown in Figure 7.5 and can be fit with exponentials to measure the spin depolarization time. Thus, the differential pump-probe signal (dR/R), can be fit using

$$\frac{dR}{R} = \left(A_1 e^{-\frac{t-t_0}{\tau_1}} + A_2 e^{-\frac{t-t_0}{\tau_2}}\right) \tag{7.1}$$

, where $A_1(A_2)$ and $\tau_1(\tau_2)$ are the amplitudes and spin lifetimes for the short-lived (long-lived) component respectively. A spin depolarization time (τ_1) for trion (exciton) ~ 200 ps (85 ps), at this voltage, is extracted [107]. The fits are shown in Figure 7.5. Note that the exciton and trion spin dynamics have an appreciable long-lived component, which can be attributed to spin polarization of the 2DEG [211]. This long time scale (τ_2) for probing at trion (exciton) is 1.3 ns (1.5 ns), at this voltage. The spin polarization of the 2DEG will now be studied with application of magnetic fields.

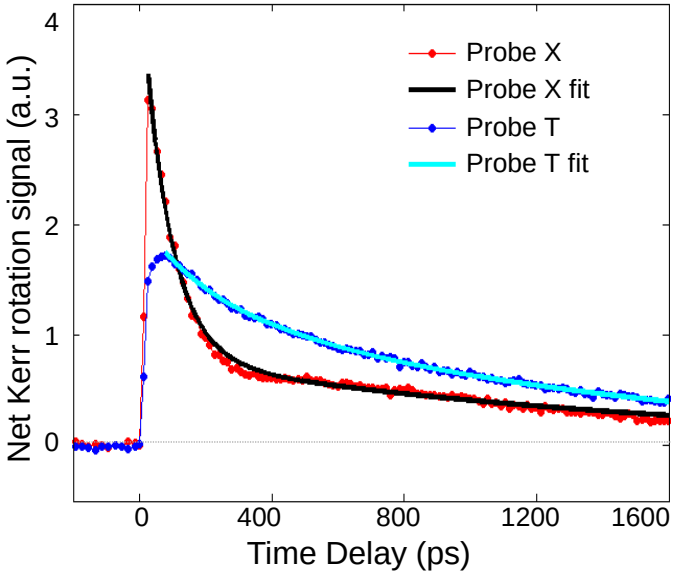

Figure 7.5: Bi-exponential fits to kerr-rotation data (LCP - RCP).

MAGNETO-OPTIC KERR-ROTATION

An in-plane (Voigt geometry) magnetic field ~ 0.3 T is applied through electro-magnets. The in-plane magnetic field induces spins, pointing in the growth axis direction (z-axis), to precess around the magnetic field at the Larmor frequency. The magnetic field thus induces oscillations in the pump-probe signal, which can be analyzed to measure spin relaxation and lande g-factors. The precession also reduces the spin component along the growth direction consequently increasing spin relaxation rates. Thus, this low magnetic field is chosen to keep the spin depolarization effect of the magnetic field small, while still inducing oscillatory behavior to measure Larmor frequencies. The Larmor frequencies can subsequently be analyzed to measure the lande-g factor.

The magneto-optic kerr measurements (MOKE) for probing at exciton and trion transition energies, are shown in Figure 7.6, at two representative voltages. The data presented here, is the difference in the signals for $\sigma-$ and $\sigma+$ pump helicities (LCP - RCP), as discussed earlier. The MOKE curves are fit with the convolution of the long-relaxation spin relaxation component and an oscillating component, oscillating at the Larmor frequency (ω_L). For the exciton and trion MOKE curves, we now incorporate a single exponential fit with the oscillating component. We do not use a bi-exponential fitting function, since the fast component does not do a full precession in the small magnetic field. We only concentrate on the time delays after 200 ps, to reduce effects of the fast component. Thus the differential MOKE delay scan is fit using

$$\frac{dR}{R} = \left(A_2' e^{-\frac{t-t_0}{\tau_2'}}\right) \sin(\omega_L t + \phi) \tag{7.2}$$

, where A_2 and τ_2' are the amplitudes and spin lifetimes for the long-lived component respectively, ω_L is the Larmor frequency of precession. ϕ is the initial phase and a fit parameter. A_2', τ_2' and other parameters can be changed from equation 7.1, due to application of the magnetic field. The fits, using the above expression, are shown with solid lines in the Figure 7.6. The times for excitons and trions are summarized in Table 7.1. The Larmor frequencies are similar, indicating we are measuring similar carriers, thus again relating the long-lived time to 2DEG state. The long time scales are slightly different for the 2DEG when exciton and trion are probed.

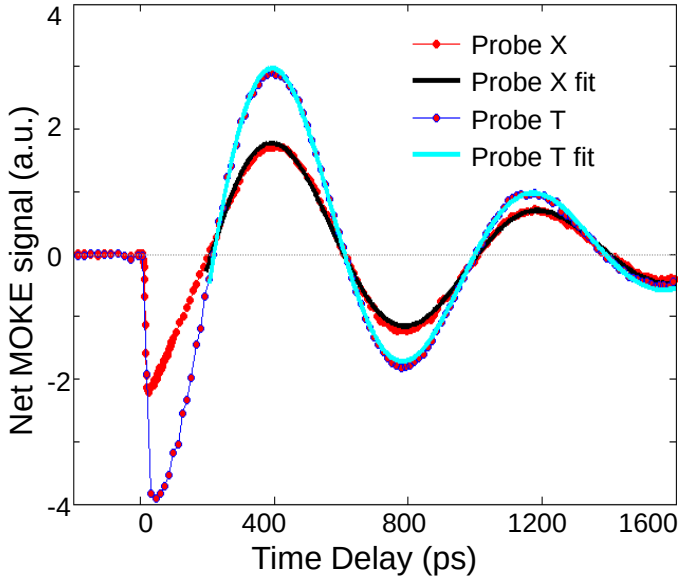

Figure 7.6: MOKE curves for probing at exciton and trion transitions, along with model fits.

	Probe at Exciton	Probe at Trion
τ_2' (ps)	866 ps	700 ps
ω_L	8 GHz	8 GHz

Table 7.1: Model fits to long time dynamics of exciton and trion MOKE curves.

The longer spin component is attributed to the 2DEG, as we have discussed. Remarkably, when this long component is measured as a function of gate voltage, interesting patterns emerge. To elucidate this, we again utilize the MOKE curves for probing at exciton energies, and again we concentrate on the regime after ~ 200 ps, where the exciton and trion spin has relaxed. The trion transition for all voltages (below 0 V), shows a large 2DEG spin polarization (data not shown). In figure 7.7, MOKE curves for two representative voltages are plotted, V_B = -0.5 V and -0.5 V. For voltage V_B = +0.5 V, we observe a complete decay in the spin response within ~ 700 ps. However, for the voltage V_B = -0.5 V, we observe two interesting temporal behaviors. Firstly, note the signal peaks at ~ 400 ps, away from the initial local maximum at shorter time delays. We attribute this to transfer of spin from the exciton to the trion state, via population relaxation, which effectively initializes the 2DEG spin polarization. Secondly, the 2DEG spin polarization persists beyond ~ 1.5 ns. The second feature is similar to the V_B = 0 V data which we displayed in Figure 7.4, 7.5 and 7.6. The two features, signal peaking away from initial delays and large 2DEG spin polarization, suggests a system in which spin scattering is minimized due to effective presence of both exciton and trions. The behavior for V_B = 0 V seems to be a combination of the behavior seen for V_B = +0.5 V and -0.5 V. The 2DEG spin polarization also persists for a long time in this case, though the magnitude is smaller in comparison to the case when V_B = -0.5 V.

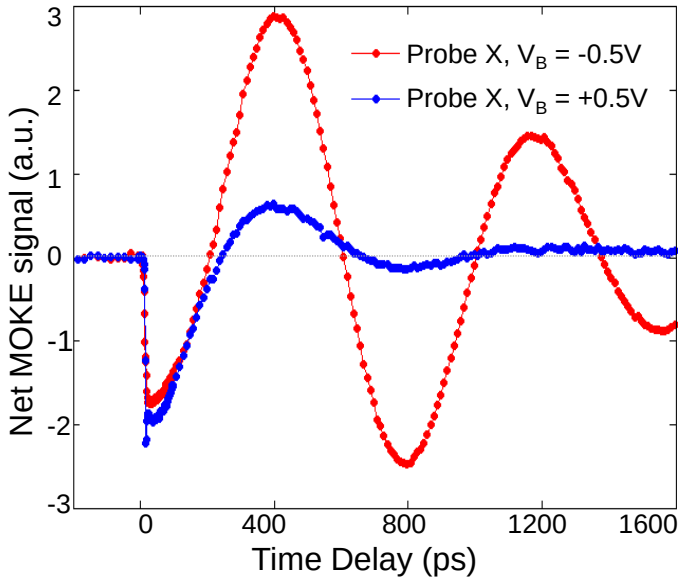

Figure 7.7: Voltage dependence of 2DEG spin initialization and spin lifetime for probing at exciton energy.

The $V_B < 0$ V voltage regime, is thus favorable for effective 2DEG spin initialization even when excitons are created. This regime can be correlated with PL where at this voltage, trions are also favorable in the system. Thus, efficient initialization of 2DEG can be done through an intermediate trion state, even when excitons are created first. Interestingly, the spin lifetime is also enhanced in this regime presenting a situation in which spin scattering events are reduced due to presence of a coupled exciton-trion state [144,211]. This presents interesting ways forward to study interactions of excitons and trions in a gated TMD sample [259]. Further, this regime is also interesting for measuring spin transport and spin diffusion. The decrease of spin relaxation is technologically interesting in spintronic applications [253].

Chapter 8: Conclusions and Outlook

The research in this dissertation was motivated by understanding the dynamics in two-dimensional systems with varying levels of quantum confinement and interactions. The first studies on TMD monolayers came out in 2010 and the field has rapidly expanded since then. There was an urgent need to study the dynamics of excitons and trions in these material systems to characterize the fundamental opto-electronic limitations of these materials.

The experiments were challenging, not just due to sample quality, but also by technical challenges. Due to small size of the samples and inhomogeneities, we could not afford motion of the sample. We developed an automatic drift correction system with continuous imaging feedback, which helped us take high quality measurements continuously for many hours. A two color pulse shaper was also devised with precise wavelength and pulse width control, enabling measurements of coupling between excitons and trions.

In this dissertation, we have successfully studied the interactions between excitons and trions in TMDs', using two-color pump-probe spectroscopy. Coherent coupling between excitons and trions is measured for the first time in these material systems, specifically $MoSe_2$ monolayers, and the strength of the coupling was measured to be an order of magnitude stronger than in traditional semiconductors like gallium arsenide. Coherent coupling between the quasiparticles suggest new approaches for manipulating spin and valley degrees of freedom associated with each quasiparticle. This is especially relevant for valleytronics since different valley coherence and polarization dynamics were recently demonstrated for excitons and trions. These measurements point

a path towards manipulating excitons and trions through one another, and utilizing desirable properties of each.

The next step in measuring the interactions (between excitons and trions) was to measure population relaxation pathways and incoherent relaxation mechanisms. We specifically focused on the exciton to trion formation process and found fast ultrafast ETF (exciton-to-trion formation) times ~ 1.5 ps. The fast time measured indicate that ETF process is an important pathway for exciton relaxation. Thus, ETF must be considered when interpreting ultrafast dynamics in time-resolved spectroscopy experiments concerning excitons. The ETF was measured for a range of exciton energies, and was found to vary across the exciton resonance. This variation is attributed to an exciton mobility edge, indicating different types of excitons present in an inhomogeneously broadened exciton resonance. The mobility edge concept has remained unexplored in studies of quasiparticle transport in TMDs so far. The mobility edge is attributed to presence of disorder (due to impurities, stress etc.) in the system. Thus, we present a way to analyze the quality of samples.

Uncovering the spin-valley coupling in TMDs' is an exciting field. We measured the spin dynamics in a monolayer WSe_2 sample, utilizing a modified spin-sensitive two-color pump-probe system. Importantly, transmission geometry was utilized, to simplify the analysis of the complex lineshapes. A fast exciton spin (valley) scattering (~ 5 ps) and longer lived trion spin (valley) polarization (~ 15 ps) is measured. A negative feature on the lower energy side was attributed to biexciton creation, and supported by polarization behavior and dynamics of spin polarization. The trion spin (valley) is efficiently initialized when resonant pumping at trion as well as exciton, and persists for more than 15 ps.

Quantum wells, with higher screening than TMDs', were measured. These quantum wells are modulation doped and provide possibilities to tune excitonic transitions using a back gate voltage. We concentrated on the dynamics of the long-lived two-dimensional electron gas (2DEG), which is interesting for spintronics. A favorable voltage regime is found for effective 2DEG spin initialization, even when excitons are created. This regime is correlated with PL and simultaneous presence of trions in the system. Thus, efficient initialization of 2DEG can be done through an intermediate trion state, even when excitons are created first. Interestingly, the spin lifetime is also enhanced in this regime presenting a situation in which spin scattering events are reduced due to presence of a coupled exciton-trion state.

This dissertation should pave a way forward into further detailed studies in the TMD materials. Our results on coherent coupling in TMDs' should motivate the development of a microscopic theory for the optical response and specially the interaction between quasiparticles. On the experimental side, specific quantum pathways can be probed through advanced spectroscopic techniques such as coherent two-dimensional Fourier-transform spectroscopy (2DFTS). Such experiments are underway in our laboratory, and are capable of measuring radiative lifetimes and homogeneous linewidths.

In these materials, the discovery of exciton mobility edge is particularly interesting as it is important for transport. Future transport experiments combining high spectral resolution and high spatial resolution will be useful to characterize the nature of this disorder and even a way to improve the material purity. Photo-current measurements with tunable excitation energy, can be utilized to measure diffusion of different quasiparticles. The nature of excitons in the inhomogeneously broadened resonance, can be independently probed for dephasing and coherent dynamics.

Spin-valley coupling in TMDs' promises a unique tuning knob for applications including chiral light emitting diodes and spintronic applications. A broadband probe might reveal still uncovered transitions in these material systems, and the polarization measurements of these transitions will be quite interesting, from a fundamental point of view. The biexcitonic feature measured here, should encourage further experiments on the nature of this transition, including coherent 2DFTS. The intriguing coupling of trions and biexcitons is a ripe ground of theoretical and further experimental investigation.

The quantum well study could be extended to interactions of excitons and trions in a gated TMD sample. Further, this regime is also interesting for measuring spin transport and spin diffusion. The decrease of spin relaxation is technologically interesting in spintronic applications employing quantum wells.

Thus, we were successful in measuring the dynamics of carrier and spin in two-dimensional systems, with varying levels of screening. Time scales were found to scale inversely with binding energy of quasiparticles in these systems. Interactions between quasiparticles was measured in TMDs' and quantum wells.

Appendices

APPENDIX – A: DENSITY MATRIX FORMALISM AND INTRODUCTION TO OPTICAL BLOCH EQUATIONS

Density Matrix

For an (isolated) closed two level system with fixed states, a complete quantum treatment is possible. These two states have well defined wavefunctions and different quantum observables can be calculated. However, real physical systems consist of interacting quantum systems. The density matrix (DM) formalism enables treatment of an ensemble of these systems. Further, real effects such as damping, dephasing and relaxation can be introduced in the DM formalism. The DM operator ρ is defined in terms of state vectors as

$$\rho = \sum_j P_j |\psi_j\rangle\langle\psi_j| \tag{A.1}$$

, where P_j is the fraction with state vectors $|\psi_j\rangle$. Here, the information about $|\psi_j\rangle$s' is usually not known, but as we will see, it is not necessary to describe certain relevant properties of the system. Certain statistical properties can be found through experiments enabling a physical description of the system. Further, the time evolution of the DM operator follows the Heisenberg formalism

$$\dot{\rho} = -\frac{i}{\hbar}[H, \rho] \tag{A.2}$$

$$H = H_0(\text{isolated}) + V(\text{interaction with incident field}) + H_R(\text{relaxation processes}) \tag{A.3}$$

For now, let us consider no relaxation processes. Thus the Hamiltonian becomes $H = H_0 + V$. Consider, the two level system depicted in Figure A.1. For a two-

level system, we denote the ground state and excited states with $|a\rangle$ and $|b\rangle$ respectively. The energies of the two levels are illustrated in the figure. The Hamiltonian H_0 is a diagonal matrix with elements given by

$$H_{0,nm} = E_n \delta_{nm} \tag{A.4}$$

Further, the interaction Hamiltonian (in the dipole approximation) has the form

$$V(t) = -\mu \cdot E(t) \tag{A.5}$$

, where μ is the dipole moment of the transition and E is the electric field of the incident light. Here, we neglect the electric quadrupole and the magnetic dipole interactions which are much reduced in the optical regime (smaller by fine structure constant ~ 1/137). The diagonal elements of the interaction Hamiltonian vanish due to definite parity, the only non-vanishing elements of the interaction Hamiltonian are the off-diagonal elements. The off diagonal elements are of the form

$$V_{ba} = V_{ab}^* = -\mu_{ba} \cdot E(t) \tag{A.6}$$

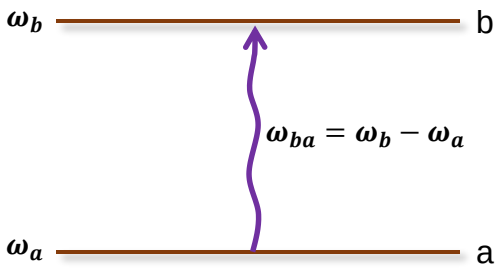

Figure A.1: Schematic of a two-level system.

The DM of this two-level system can be explicitly written as

$$\rho = \begin{pmatrix} \rho_{aa} & \rho_{ab} \\ \rho_{ba} & \rho_{bb} \end{pmatrix} \tag{A.7}$$

, where $\rho_{ba} = \rho_{ab}^*$. The diagonal elements of the DM represent the probability of finding the system in the two energy eigenstates ($|a\rangle$ or $|b\rangle$). The off-diagonal elements represents the superposition between the eigenstates induced by the incident field. In other words, the off-diagonal elements represents the coherence of the quantum superposition state. The induced dipole moment, $\hat{\mu}$, is related to the off-diagonal elements

$$\hat{\mu} = trace(\rho\mu) = \begin{pmatrix} \rho_{aa} & \rho_{ab} \\ \rho_{ba} & \rho_{bb} \end{pmatrix} \begin{pmatrix} 0 & \mu_{ab} \\ \mu_{ba} & 0 \end{pmatrix} = \rho_{ab}\mu_{ba} + \rho_{ba}\mu_{ab} \tag{A.8}$$

The time evolution of the density matrix is then given by (utilizing equation A.2)

$$\dot{\rho}_{nm} = -\left(\frac{i}{\hbar}\right)[H, \rho]_{nm} = -\frac{i}{\hbar}\{(H\rho)_{nm} - (\rho H)_{nm}\} \tag{A.9}$$

For this two-level system we then have a set of coupled equations

$$\dot{\rho}_{ba} = -i\omega_{ba}\rho_{ba} + \frac{i}{\hbar}V_{ba}(\rho_{bb} - \rho_{aa}) \tag{A.10a}$$

$$\dot{\rho}_{bb} = -\frac{i}{\hbar}(V_{ba}\rho_{ab} - \rho_{ba}V_{ab}) \tag{A.10b}$$

$$\dot{\rho}_{aa} = -\frac{i}{\hbar}(V_{ab}\rho_{ba} - \rho_{ab}V_{ba}) \tag{A.10c}$$

, where $\omega_{ba} = \omega_b - \omega_a$. Note that, $\dot{\rho}_{aa} + \dot{\rho}_{bb} = 0$, thus the total population $\rho_{aa} + \rho_{bb} = 1$, is a conserved quantity. We have discussed systems with no relaxation behavior. The DM treatment until now, is relevant for ultra-short pulses where the pulse temporal width is much shorter than the material relaxation times. Now, we extend the DM formalism to physical systems with relaxation mechanisms.

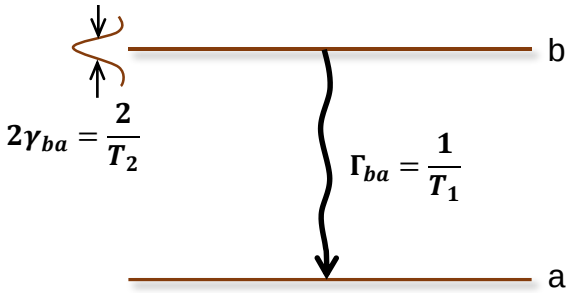

Figure A.2: Relaxation processes in a two-level system.

In real physical systems, due to collisions with carriers and lattice, relaxation mechanisms are intrinsic. These mechanisms can be grouped into population relaxation (spontaneous emission, radiative relaxation) and dephasing (elastic collisions) mechanisms. We illustrate the time-scales of these mechanisms in Figure A.2. The lifetime of the upper level is governed by the relaxation rate (Γ_{ba}) and is depicted by T_1. The T_1 time governs the behavior of the diagonal elements in the DM. The dipole moment (related to the off-diagonal elements), on the other hand, can relax due to pure

dephasing (elastic collisions with electrons or atomic point scatterers) or population relaxation, in a time scale T_2. This T_2 time is related to the linewidth of the transition ($|a\rangle \rightarrow |b\rangle$) given by $\gamma_{ba} = 1/T_2$. Further, T_1 and T_2 are related to each other by

$$\frac{1}{T_2} = \frac{1}{2T_1} + \gamma_c \tag{A.11}$$

, where γ_c is pure dephasing rate. Note that the pre-factor of 2, in the denominator of the first term on the right hand side, is due to consideration of the ground and excited states. If we consider two excited states, then the first term is an average of the population relaxation rates of the two (excited) states. These time-scales (T_1 and T_2) can be included phenomenologically in equations A.10a-c to get

$$\dot{\rho}_{ba} = -\left(i\omega_{ba} + \frac{1}{T_2}\right)\rho_{ba} \quad + \frac{i}{\hbar}V_{ba}(\rho_{bb} - \rho_{aa}) \tag{A.12a}$$

$$\dot{\rho}_{bb} = -\frac{\rho_{bb}}{T_1} - \frac{i}{\hbar}(V_{ba}\rho_{ab} - \rho_{ba}V_{ab}) \tag{A.12b}$$

$$\dot{\rho}_{aa} = +\frac{\rho_{bb}}{T_1} - \frac{i}{\hbar}(V_{ab}\rho_{ba} - \rho_{ab}V_{ba}) \tag{A.12c}$$

A consequence of equation A.8 and A.12a is the time evolution of the induced dipole moment, given by

$$\hat{\mu}(t) = \left[\mu_{ab}\rho_{ba}(0)e^{-i\omega_{ba}t} + complex\ conjugate\right] \cdot e^{-t/T_2} \tag{A.13}$$

, where $\mu_{ab}\rho_{ba}(0)$ is the dipole moment of the system just after the interaction field goes to zero. Thus, the dipole moment of the un-driven atom oscillates at frequency ω_{ba} and

decays with a time-scale T_2 (dipole dephasing time). Note that the part in brackets, on the right hand side, is the solution for equation A.10. Further, it is clear from equations A.12b and A.12c that the population of the eigenstates of the un-driven system relax with a time-scale T_1. Thus, the parameters we have included phenomenologically in the DM formalism, have physical relevance and can be measured experimentally.

Optical Bloch Equations and Feynman diagrams

Optical bloch equations (OBEs') are a simplification of equation A.12 and are useful for interpreting temporal dynamics of experiments in the optical regime. The two formalisms (OBE and DM) have equivalent predictions but their forms can be different. In quantum optics, OBEs' are preferred for calculating material response. The formalism is established by substituting $n = \rho_{bb}, 1 - n = \rho_{aa}$ and $p = \rho_{ba}$. n and p are referred to as the population and polarization respectively. Consequently, equation A.7 is converted to

$$\rho = \begin{pmatrix} 1-n & p^* \\ p & n \end{pmatrix} \tag{A.14}$$

, and equations A.12a and A.12b are converted to

$$\dot{n} + \gamma_r n + \left(\frac{i}{\hbar}\right)(V_{ba}p^* - pV_{ab}) = 0 \tag{A.15a}$$

, and

$$\dot{p} + \Omega p + \left(\frac{i}{\hbar}\right)\dot{V}_{ba}(1-2n) = 0 \tag{A.15b}$$

, where γ_r is the relaxation rate $(1/T_1)$ and $\Omega = \left(i\omega_{ba} + {}^{1}/_{T_2}\right)$.

The coupled equations A.15a-b can-not be solved analytically in the general case. Thus, we extend the OBE formalism through perturbation theory. We write the population and polarization as a Taylor series expansion in incident field amplitudes as

$$n = n^{(0)} + n^{(1)} + n^{(2)} + n^{(3)} + \cdots \tag{A.16}$$

, and

$$p = p^{(0)} + p^{(1)} + p^{(2)} + p^{(3)} + \cdots \tag{A.17}$$

Conveniently, $n^{(0)} = p^{(0)} = 0$. Importantly, we note that the electric field can only create a population in the second order of interaction, i.e. the odd power components of n are zero. Similarly, the electric field can induce a polarization in the first (and odd) order of interaction and thus, even power components of p are zero. Hence, we get

$$\dot{p}^{(1)} + \Omega p^{(1)} + \left(\frac{i}{\hbar}\right) V_{ba} = 0 \tag{A.18}$$

$$\dot{n}^{(2)} + \gamma_r n^{(2)} + \left(\frac{i}{\hbar}\right)\left(V_{ba} p^{*(1)} - p^{(1)} V_{ba}^{*}\right) = 0 \tag{A.19}$$

$$\dot{p}^{(3)} + \Omega p^{(3)} - 2\left(\frac{i}{\hbar}\right) V_{ba} n^{(2)} = 0 \tag{A.20}$$

Thus, $n(p)$ of order j is influenced by $p(n)$ of order j-1. Consequently, a third order polarization field can be influenced by a population of carriers through an interaction field.

The formalism we have established in equations A.18-20 can be used to calculate the transient response of semiconductors to applied laser pulses. Consider a typical optical experiment where a pump field is incident on the sample

$$E(t) = \left(\frac{1}{2}\right)\left[E_1(t)\,\mathrm{e}^{k.r-i\omega t} + E_1^*(t)e^{-k.r+i\omega t}\right] \tag{A.21}$$

Utilizing the rotating wave approximation, the complex conjugate leads to a contribution oscillating at high frequencies, which can be neglected. Thus, we get

$$E(t) = \left(\frac{1}{2}\right)\left[E_1(t)e^{k.r-i\omega t}\right] \tag{A.22}$$

Then p should be of the form

$$p^{(1)} = p^{(1)}(t)\mathrm{e}^{-i\omega t} \tag{A.23}$$

Plugging equation A.22 in A.18, and solving for $p^{(1)}$, we have

$$p^{(1)} = \frac{i\mu}{2\hbar}\left[\int_{-\infty}^{t} E(t')e^{\left(-(\Omega-i\omega)(t-t')\right)}\,dt'\right]e^{(k.r-i\omega t)} \tag{A.24}$$

Consequently, equation A.24 can be used in equation A.19 to obtain $n^{(2)}$ of the form of a double integral. This $n^{(2)}$ can be inserted in A.25 to deduce $p^{(3)}$ of the form of a triple integral. While calculating $n^{(2)}$ and $p^{(3)}$, the pulse ordering (from the actual experiment) is used in the order of integrands.

An elegant way to calculate the contributions to these integrals is through double sided Feynman diagrams. These diagrams can be used to track the order of the interaction field, relatively easily. The Feynman construction follow some general rules for diagrams which are illustrated in Figure A.3. Vertical lines are drawn to track bra and ket that make the density matrix (refer to A.1), time increases from bottom to top and each vertex

(arrow) represents an interaction with optical field that changes the state of the system. Arrows pointing into and out of the diagram follow conventions illustrated in Figure A.3, relating to the direction of wave-vectors and whether energy of the system is increased or decreased via interaction with the optical field.

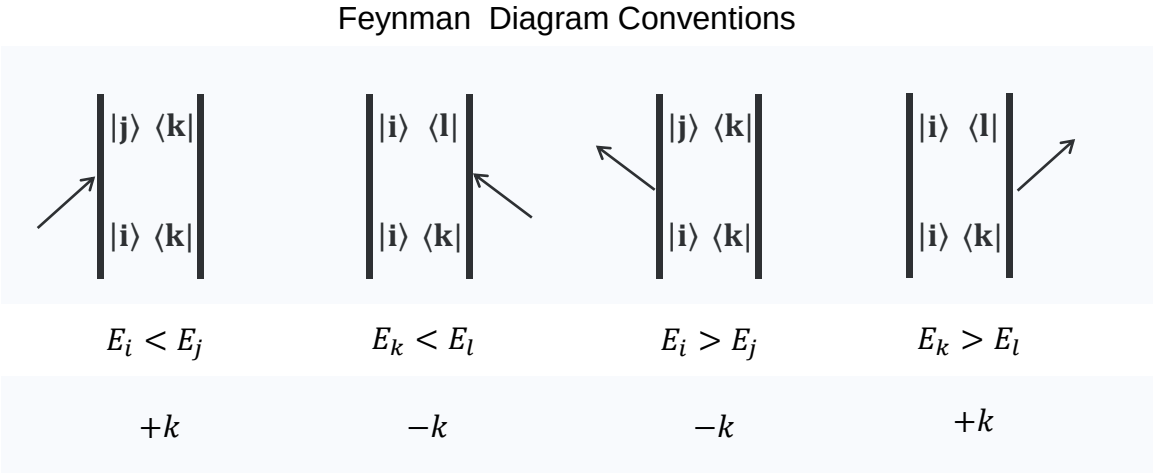

Figure A.3: Energy and wave-vector sign conventions used in double sided Feynman diagrams.

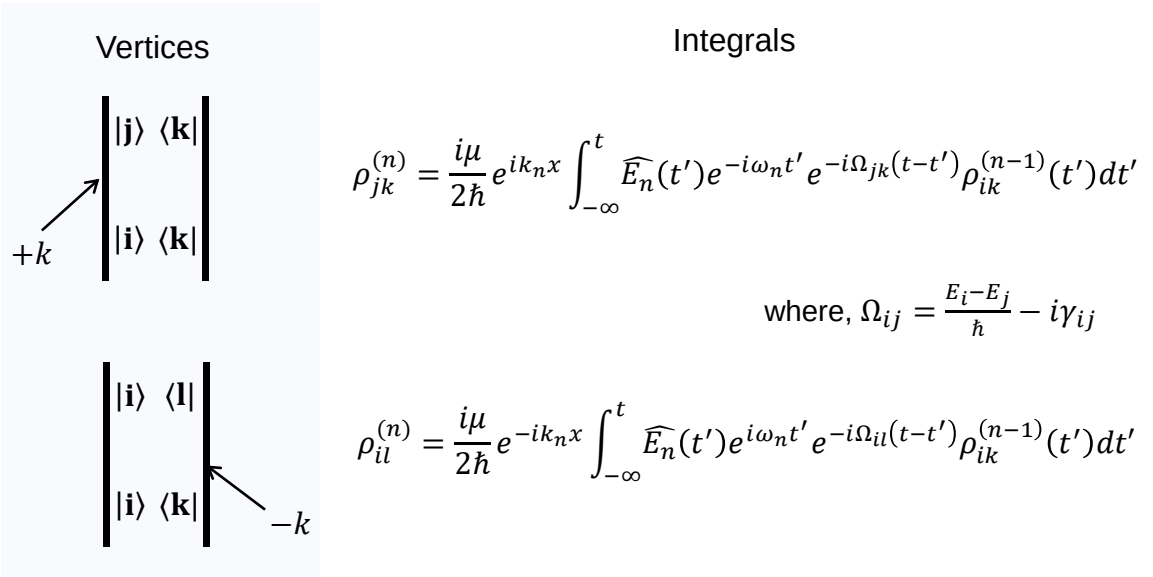

Figure A.4: DM integrals arising from Feynman diagrams.

For calculations through these Feynman diagrams, we switch back to the DM formalism. An illustration of the power of these diagrams is shown in Figure A.4 along with typical expressions of the DM component. Notice that conventions explained in Figure A.3 have been invoked for the k vector (wave-vector). The integrals are expressions for a general multi-level diagram (rather than the two level diagram we have discussed) [170]. Note that $\rho_{jk}^{(n)}$ is dependent on $\rho_{ik}^{(n-1)}$ (transition induced from $|i\rangle\langle k| \rightarrow |j\rangle\langle k|$), which is similar to the conclusion drawn by invoking the OBEs' for a two-level system. For a third-order nonlinear experiment probing a particular state, all the diagrams leading to that state in the third order of interaction field, are added to get the total nonlinear signal. In an actual pump-probe experiment, the optical fields are ultrafast laser pulses which can be considered as delta pulses (in time). Using the concept of delta pulses and causality (pulse ordering, pump pulse comes before probe pulse), the signals can be calculated through numerical integration. This scheme is used to calculate the simulated signal in chapter 4.

APPENDIX- B: OPTICAL BLOCH EQUATIONS FOR MODELLING EXCITON-TRION COUPLING AND FITTING PROCEDURE.

The ultrafast two-dimensional pump-probe spectrum is simulated by analytically solving a perturbative expansion of the optical Bloch equations. The simulations are based on the four-level energy scheme presented in Figure B.1. Before discussing details of the simulation, justification for describing the exciton-trion system using a four-level energy scheme is provided, based on the idea of a Hilbert space transformation S [201]. Let us consider two independent systems with Hamiltonians H_1 and H_2, consisting of m and n uncoupled states, respectively. Each Hamiltonian can be written as

$$H_1 = \begin{pmatrix} E_1 & 0 & \dots & 0 \\ 0 & E_2 & \dots & 0 \\ \vdots & \vdots & \ddots & \vdots \\ 0 & 0 & 0 & E_n \end{pmatrix} \tag{B.1}$$

, and

$$H_2 = \begin{pmatrix} E_1' & 0 & \dots & 0 \\ 0 & E_2' & \dots & 0 \\ \vdots & \vdots & \ddots & \vdots \\ 0 & 0 & 0 & E_n' \end{pmatrix} \tag{B.2}$$

, where the diagonal elements are the energy eigenvalues of the two systems. The two independent systems can be combined through a Hilbert space transformation into a single system with $m \times n$ states and total Hamiltonian H_{tot} given by

$$H_{tot} = H_1 \otimes I_n + I_m \otimes H_2 \tag{B.3}$$

, where I_j is the identity matrix of j. H_{tot} is a diagonal matrix with its diagonal elements equal to the energy eigenvalues of the combined system.

Using this procedure, two independent two-level systems can be represented by an equivalent four-level diamond scheme. Let us consider two non-interacting singly-excited exciton and trion transitions $|g\rangle \leftrightarrow |X\rangle$ and $|g\rangle \leftrightarrow |T\rangle$, respectively, as shown in Figure B.1a. An equivalent four-level system is shown in Figure B.1b, where $|0\rangle$ is the ground state, $|1\rangle$ and $|2\rangle$ are the trion and exciton states, respectively, and state $|3\rangle$ comprises both the $|X\rangle$ and $|T\rangle$ transitions. Similar lines (solid or dashed) indicate the transitions that must have identical properties for the two representations to be equivalent. These two representations are equivalent provided that the lower transitions, $|0\rangle \leftrightarrow |2\rangle$ and $|0\rangle \leftrightarrow |1\rangle$, have equal values for the electronic and optical properties, such as the resonance energy, dipole moment, and dephasing rate, compared to the corresponding upper transitions, $|1\rangle \rightarrow |3\rangle$ and $|2\rangle \rightarrow |3\rangle$, respectively. The states represented in Figure B.1b are essentially two-particle states, as indicated in Figure B.1c. For example, the singly-excited states $|2\rangle$ and $|1\rangle$ are the composite states for the exciton-trion system with either the exciton or the trion in the excited state, respectively.

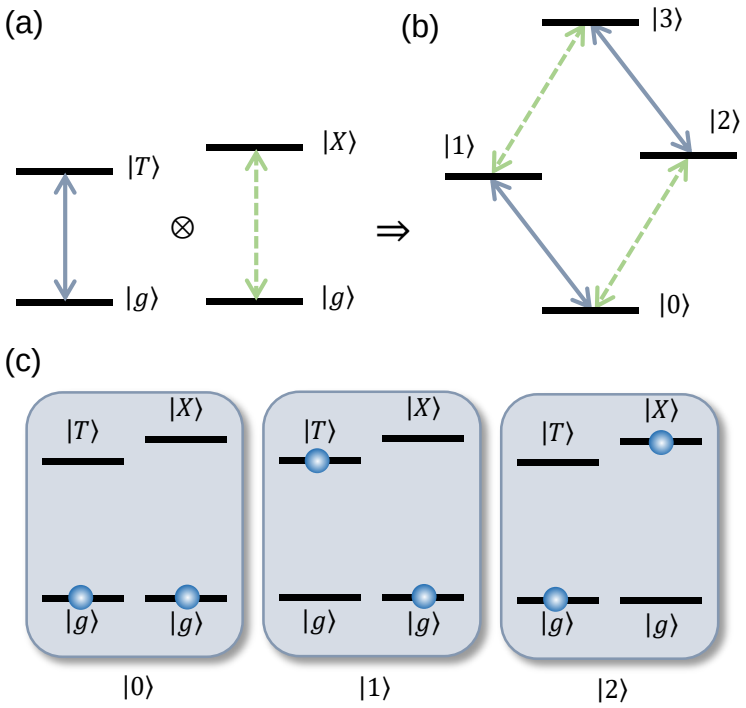

Figure B.1: Two independent two-level systems a) and the equivalent four-level diamond system b). The states in b) consist of two-particle states, as explicitly shown in c).

Experimentally, modulation of the pump and probe amplitudes and phase-sensitive detection of the nonlinear pump-probe signal at the modulation difference frequency isolates quantum mechanical pathways for which the pump field acts twice, the probe field once, and the detected signal comprises the interference between the nonlinear signal and the reflected probe field acting as a local oscillator. Moreover, the experiment is performed so that the pump pulse precedes the probe pulse. All possible quantum pathways for this configuration are represented by the double-sided Feynman diagrams shown in Figure 4.5. Only the quantum pathways for which either the pump or the probe pulse can excite the exciton or trion, but not both simultaneously, are considered, consistent with our experiments. In the experiment, the signal detected at the

photodiode consists of the nonlinear signal generated by the pump and probe pulses as well as the reflected probe pulse acting as a local oscillator and is given by

$$R = \left|E_{pr} + \Delta E_{pr}\right|^2 = \left|E_{pr}\right|^2 + \left|\Delta E_{pr}\right|^2 + E_{pr} \cdot \Delta E_{pr}^* + E_{pr}^* \cdot \Delta E_{pr} \quad \text{(B.4)}$$

, where E_{pr} is the reflected probe field and ΔE_{pr} is the nonlinear signal field. ΔE_{pr} is related to the pump E_p and probe field amplitudes by $\Delta E_{pr} \propto E_{pr} \cdot E_p \cdot E_p^*$, so that the cross term $E_{pr}^* \cdot \Delta E_{pr}$ in equation B.4 is proportional to $\left|E_{pr}\right|^2 \cdot \left|E_p\right|^2$. This was also explained in chapter 3. Thus, to simulate the differential pump-probe signal, $dR = (R - R_0)/R_0$, one needs to use the Feynman diagrams given in Figure 4.5 of the main text to calculate ΔE_{pr}. ΔE_{pr} is calculated in the time domain by perturbatively solving the optical Bloch equations to third order in the applied field using a similar method as in [260]. The simulations are performed using Dirac delta function pulses in time with the pump preceding the probe, as depicted in the timing diagram in Figure B.2a. The total nonlinear signal is given by summing contributions from each double-sided Feynman diagram in Figure 4.5. The Feynman diagrams can be generalized into three types of diagrams corresponding to nonlinearities arising from excited state emission (Figure B.2b), ground state bleaching (Figure B.2c), and excited state absorption (Figure B.2d). For the rephasing (non-rephasing) pulse time ordering, the conjugated pump field, E_p^*, arrives at the sample first (second) and is followed by the unconjugated (conjugated) pump field after a time τ and the probe field, E_{pr}, after a delay t_D.

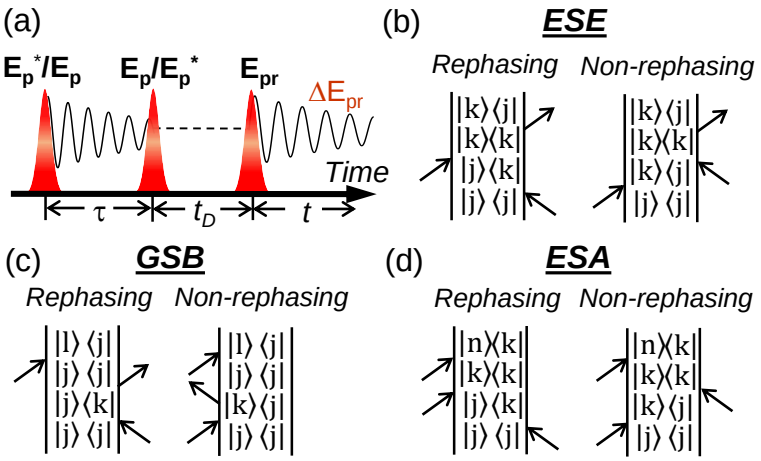

Figure B.2: a) Timing diagram for pump-probe simulations. Generalized double-sided Feynman diagrams used for the simulation are grouped into b) excited-state emission (ESE), c) ground-state bleaching (GSB), and d) excited-state absorption (ESA) terms.

Generalized expressions for diagrams in Figure B.2b, Figure B.2c and Figure B.2d are given by equations B.5, B.6 and B.7 respectively.

$$\Delta E_{pr} \propto \frac{\mu_{kj}^4}{8\hbar^3} \cdot E_{pr} E_p E_p^* \cdot \Theta(t)\Theta(t_D)\Theta(\tau) \times e^{\{i(\pm\omega_{kj}\tau - \omega_{kj}t)\}} \cdot e^{\{-(\gamma_{kj}\tau + \gamma_{kk}^{pop} t_D + \gamma_{kj}t)\}} \tag{B.5}$$

$$\Delta E_{pr} \propto \frac{\mu_{kj}^2 \mu_{lj}^2}{8\hbar^3} \cdot E_{pr} E_p E_p^* \cdot \Theta(t)\Theta(t_D)\Theta(\tau) \times e^{\{i(\pm\omega_{kj}\tau - \omega_{lj}t)\}} \cdot e^{\left\{-\left(\gamma_{kj}\tau + \gamma_{jj}^{pop} t_D + \gamma_{lj}t\right)\right\}} \tag{B.6}$$

$$\Delta E_{pr} \propto \frac{\mu_{kj}^2 \mu_{nk}^2}{8\hbar^3} \cdot E_{pr} E_p E_p^* \cdot \Theta(t)\Theta(t_D)\Theta(\tau) \times e^{\{i(\pm\omega_{kj}\tau - \omega_{nk}t)\}} \cdot e^{\{-(\gamma_{kj}\tau + \gamma_{kk}^{pop} t_D + \gamma_{nk}t)\}} \tag{B.7}$$

Free parameters for each transition include the normalized dipole moment (μ), homogeneous linewidth full-width at half-maximum (γ), population decay rate (γ^{pop}), and transition energy ($\hbar\omega$). Inhomogeneity of the transition energies can be included by integrating each equation over a two-dimensional Gaussian distribution that correlates the transition energies during the first (τ) and third (t) time delays and whose Fourier pairs correspond to the pump and probe frequencies, respectively. Perfect correlation of the transition energies during τ and t implies that any change in the transition energy during t is correlated with changes in the energy during τ. For the rephasing quantum pathways for peaks X and T in which the conjugated pump field (E_p^*) acts on the sample first, perfect correlation results in an elongated peak that is inhomogeneously broadened along the diagonal line connecting similar pump and probe energies ($\hbar\omega_p = \hbar\omega_{pr}$), and is narrow along the orthogonal direction with a linewidth that is determined primarily by the homogeneous linewidth. Because the measured peaks X and T have similar linewidths along these two directions, either the transition energies are uncorrelated during τ and t, or the inhomogeneous and homogeneous linewidths are of similar order of magnitude. Since the experiments are performed for short pump-probe delay t_D = 0.7 ps, deviation from perfect (or nearly-perfect) correlation of the linewidths is unlikely since spectral diffusion processes in semiconductors typically occur on a longer timescale. Thus, the round lineshape of the peaks implies that the homogeneous and inhomogeneous linewidths are similar order of magnitude. This is an interesting result, since such a broad homogeneous linewidth for both X and T, as discussed below, implies that significant pure dephasing mechanisms are present even at low sample temperature and excitation density. Under these conditions, we find negligible quantitative differences when including the effects of inhomogeneity and therefore set the inhomogeneous linewidth to zero.

In total, the number of free parameters in the simulation equals 15, including a relative phase shift between the nonlinear signal and reflected probe and the exciton→ trion population relaxation rate that is modeled by including additional decay and source terms to the Feynman diagrams. We assume that the dipole moments of the $|0\rangle \leftrightarrow |1\rangle$ and $|2\rangle \leftrightarrow |3\rangle$ transitions are equal (similarly for the $|0\rangle \leftrightarrow |2\rangle$ and $|1\rangle \leftrightarrow |3\rangle$), since the transitions originate from the same single-particle transitions. The set of parameters that are used to produce the simulated spectrum in Figure 4.6 of the main text are shown in Table 4.1. The values for E_1 and E_2 are obtained directly from the trion and exciton resonance energies, respectively, in the pump-probe spectrum. The population decay rates for the trion and exciton are obtained from the exponential decay of their amplitudes with respect to the pump-probe delay t_D (data not shown). The remaining nine parameters are determined by comparing the measured and simulated differential probe spectrum for resonant pumping at the exciton and trion resonances and using a least squares regression analysis to minimize the error. The dipole moment and homogeneous linewidth of the $|0\rangle \leftrightarrow |1\rangle$ transition and the signal/probe relative phase are obtained by adjusting the parameters of this transition until the horizontal slice (constant pump energy) through peak T minimizes the least squares error for this peak. A similar procedure is performed to obtain the dipole moment and homogeneous width for the $|0\rangle \leftrightarrow |2\rangle$ transition (minimizing the least squares error for peak X). The effect of the phase will be discussed in Appendix C.

The remaining free parameters in the simulation are associated with exciton-trion interactions, specifically EIS through Δ' and EID effects through an enhanced dephasing rate of the upper transitions. The only set of parameters that reproduces the amplitude and lineshape of peaks XT and TX is an EIS of state $|3\rangle$ equal to $\Delta' = 4$ meV and EID of the $|1\rangle \leftrightarrow |3\rangle$ transition compared to the $|0\rangle \leftrightarrow |2\rangle$ transition with $\gamma' = 25$ meV. EIS is

the only mechanism that produces a negative-absorptive lineshape for peak TX. In order to enhance the amplitude of peak XT compared to TX, EID effects must be present. We estimate an upper and lower limit for EIS of $\Delta' = 5.5$ meV and $\Delta' = 2.5$ meV, respectively, by adjusting Δ' (and subsequently altering the other parameters to minimize the error) until the minimum least squares error increases by 50%.

APPENDIX- C: INFLUENCE OF PHASE BETWEEN REFLECTED PROBE AND NONLINEAR SIGNAL

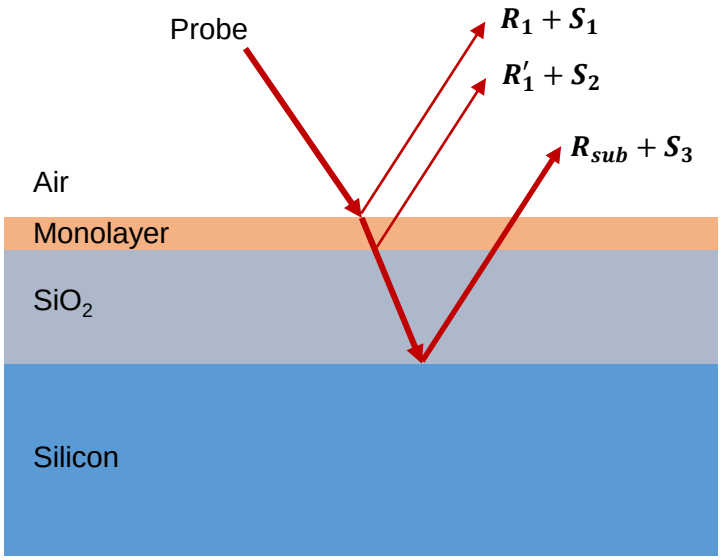

Figure C.1: Probe reflection from different layers of the sample.

In samples with non-transparent substrates, the probe is reflected from the substrate into the detection path. In fact, much more probe is reflected from the substrate than the TMD monolayer. This reflection is illustrated in Figure C.1, where the incidence angle of the probe beam is slightly tilted to make the illustration clearer. Consider a probe beam incident on a sample consisting of the monolayer on a SiO_2/Si layer. The SiO_2 layer is around 280 nm thick while the silicon layer is considered semi-infinite. Consequently, three reflections can occur, as illustrated in Figure C.1. Each pass through the monolayer induces a signal field, but each signal field (S_1, S_2, S_3) are with different (relative) phases due to different optical paths traveled. If we consider the monolayer having (almost) zero thickness, S_1 and S_2 will have same phase with respect to each other but S_3 will have different relative phase. Further, most of the probe field will be reflected at the SiO_2-Si interface. Thus, the signal and the probe field will have a finite relative phase.

The phase difference (between probe and signal fields) is responsible for different optical contrast depending on substrates, the non-visibility of optical signals and quenching of certain Raman or photoluminescence signals [153,261,262]. Thus, optimizing the phase, by suitable choice of SiO_2 thickness or choice of substrate, is critical. Further, characterizing this phase and including it in the calculations (for chapter 4) is important for analysis of lineshapes.

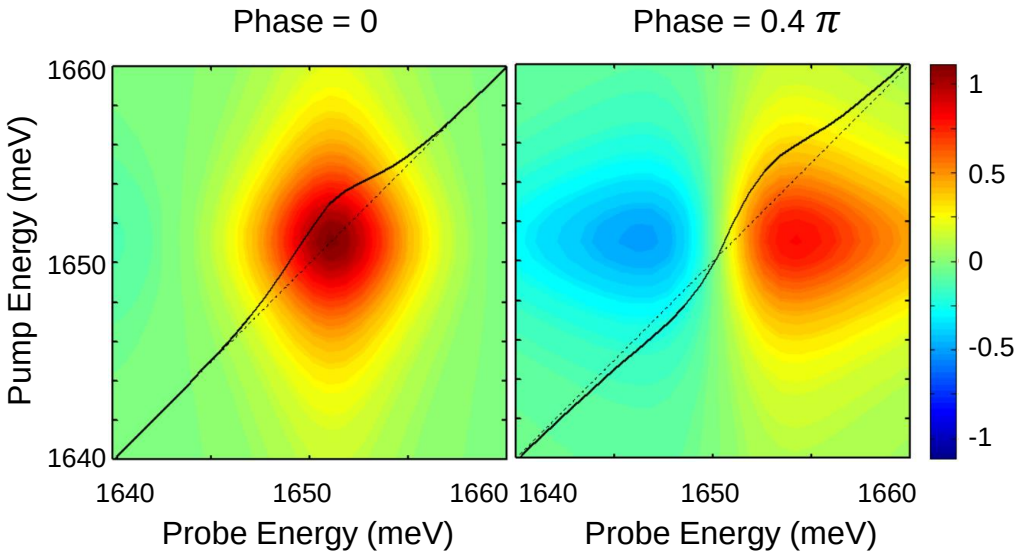

Figure C.2: Influence of the relative phase of signal and probe fields on the shape of the differential pump-probe signal.

An example of including the phase in the calculation of a single exciton peak is illustrated in Figure C.2. Here the phase ϕ, is accounted for in the following way

$$dR = \Delta E_{pr} \times E_{probe} \tag{C.1}$$

$$\Rightarrow \frac{dR}{R_0} = \frac{(\Delta E_{pr} \times E_{probe})}{|E_{probe}|^2} = \frac{(\Delta E_{pr} E_{probe}) e^{i\phi}}{|E_{probe}|^2} \tag{C.2}$$

, where ΔE_{pr} is the total third order nonlinear signal calculated by summing up the different contributing Feynman diagrams, as in Appendix B. The real part of equation C.2 is plotted in the simulation in Figure C.2. The effect of changing the phase (ϕ) can be seen in Figure C.2 where a purely absorptive peak can appear as a dispersive line-shape in the differential reflection signal. The spectrum on the diagonal line is drawn to illustrate the effect of phase on the differential pump-probe signal, when pump and probe are degenerate. Thus, the procedure for analyzing the phase and other simulation parameters, as outlined in Appendix B, is important for analyzing lineshapes. This procedure is relaxed for samples on transparent substrates, which can be utilized for even more complex lineshape analysis.

References

[1] R. W. Cahn, *The science of dirt*, Nat Mater **1**, 3 (2002).

[2] E. F. Zalewski and C. R. Duda, *Silicon photodiode device with 100% external quantum efficiency*, Appl. Opt. **22**, 2867 (1983).

[3] J. R. Arthur, *Molecular beam epitaxy*, Surface Science **500**, 189 (2002).

[4] J. M. Rabaey, A. P. Chandrakasan, and B. Nikolic, *Digital integrated circuits* (Prentice hall Englewood Cliffs, 2002), Vol. 2.

[5] R. R. Schaller, *Moore's law: past, present and future*, Spectrum, IEEE **34**, 52 (1997).

[6] G. E. Moore, *Cramming more components onto integrated circuits*, Electronics **38**, 114 (1965).

[7] A. Jain and R. T. Bonnecaze, *Fluid management in roll-to-roll nanoimprint lithography*, J. App. Phys. **113**, 234511 (2013).

[8] M. Ieong, B. Doris, J. Kedzierski, K. Rim, and M. Yang, *Silicon Device Scaling to the Sub-10-nm Regime*, Science **306**, 2057 (2004).

[9] B. Ohare, Wikimedia, Licensed under CC BY-SA 3.0 via Commons

[10] M. Radosavljevic, B. Chu-Kung, S. Corcoran, G. Dewey, M. K. Hudait, J. M. Fastenau, J. Kavalieros, W. K. Liu, D. Lubyshev, M. Metz, K. Millard, N. Mukherjee, W. Rachmady, U. Shah, and R. Chau, in *Electron Devices Meeting (IEDM), 1999 IEEE International*, pp. 1.

[11] J. H. Choi, Y. Mao, and J. P. Chang, *Development of hafnium based high-k materials—A review*, Materials Science and Engineering: R: Reports **72**, 97 (2011).

[12] M. J. Allen, V. C. Tung, and R. B. Kaner, *Honeycomb Carbon: A Review of Graphene*, Chemical Reviews **110**, 132 (2010).

[13] S. H. Chan, A. K. Wong, and E. Y. Lam, *Initialization for robust inverse synthesis of phase-shifting masks in optical projection lithography*, Optics Express **16**, 14746 (2008).

[14] E. Yablonovitch and R. B. Vrijen, *Optical projection lithography at half the Rayleigh resolution limit by two-photon exposure*, OPTICE **38**, 334 (1999).

[15] P. Gurtler, V. Saile, and E. E. Koch, *High resolution absorption spectrum of nitrogen in the vacuum ultraviolet*, Chem. Phys. Lett. **48**, 245 (1977).

[16] W. Lu and C. M. Lieber, *Nanoelectronics from the bottom up*, Nat Mater **6**, 841 (2007).

[17] J. Li, Q. Ye, A. Cassell, H. T. Ng, R. Stevens, J. Han, and M. Meyyappan, *Bottom-up approach for carbon nanotube interconnects*, App. Phys. Lett. **82**, 2491 (2003).

[18] J. Y. Cheng, C. A. Ross, H. I. Smith, and E. L. Thomas, *Templated Self-Assembly of Block Copolymers: Top-Down Helps Bottom-Up*, Advanced Materials **18**, 2505 (2006).

[19] E. Borgarello, K. Kalyanasundaram, M. Grätzel, and E. Pelizzetti, *Visible Light Induced Generation of Hydrogen from H2S in CdS-Dispersions, Hole Transfer Catalysis by RuO2*, Helvetica Chimica Acta **65**, 243 (1982).

[20] S. D. Tilley, M. Cornuz, K. Sivula, and M. Grätzel, *Light-Induced Water Splitting with Hematite: Improved Nanostructure and Iridium Oxide Catalysis*, Angewandte Chemie **122**, 6549 (2010).

[21] A. Ashkin, J. M. Dziedzic, J. E. Bjorkholm, and S. Chu, *Observation of a single-beam gradient force optical trap for dielectric particles*, Opt. Lett. **11**, 288 (1986).

[22] L. V. Hau, S. E. Harris, Z. Dutton, and C. H. Behroozi, *Light speed reduction to 17 metres per second in an ultracold atomic gas*, Nature **397**, 594 (1999).

[23] D. S. Wiersma, P. Bartolini, A. Lagendijk, and R. Righini, *Localization of light in a disordered medium*, Nature **390**, 671 (1997).

[24] J. J. Rocca, V. Shlyaptsev, F. G. Tomasel, O. D. Cortázar, D. Hartshorn, and J. L. A. Chilla, *Demonstration of a Discharge Pumped Table-Top Soft-X-Ray Laser*, Phys. Rev. Lett. **73**, 2192 (1994).

[25] Z. Zhang and S. Satpathy, *Electromagnetic wave propagation in periodic structures: Bloch wave solution of Maxwell's equations*, Phys. Rev. Lett. **65**, 2650 (1990).

[26] J. D. Jackson, *Classical electrodynamics* (Wiley New York etc., 1999), Vol. 3.

[27] L. Zhu, J. Kapraun, J. Ferrera, and C. J. Chang-Hasnain, *Flexible photonic metastructures for tunable coloration*, Optica **2**, 255 (2015).

[28] Y. Zhou, M. C. Y. Huang, and C. J. Chang-Hasnain, *Large Fabrication Tolerance for VCSELs Using High-Contrast Grating*, Photonics Technology Letters **20**, 434 (2008).

[29] R. Kirchain and L. Kimerling, *A roadmap for nanophotonics*, Nat Photon **1**, 303 (2007).

[30] M. S. Tame, K. R. McEnery, S. K. Ozdemir, J. Lee, S. A. Maier, and M. S. Kim, *Quantum plasmonics*, Nat Phys **9**, 329 (2013).

[31] K. J. Savage, M. M. Hawkeye, R. Esteban, A. G. Borisov, J. Aizpurua, and J. J. Baumberg, *Revealing the quantum regime in tunnelling plasmonics*, Nature **491**, 574 (2012).

[32] J. A. Schuller, E. S. Barnard, W. Cai, Y. C. Jun, J. S. White, and M. L. Brongersma, *Plasmonics for extreme light concentration and manipulation*, Nat Mater **9**, 193 (2010).

[33] N. W. Ashcroft and K. Sturm, *Interband Absorption and the Optical Properties of Polyvalent Metals*, Phys. Rev. B **3**, 1898 (1971).

[34] S. A. Maier, *Plasmonics: fundamentals and applications* (Springer Science & Business Media, 2007).

[35] H. A. Atwater and A. Polman, *Plasmonics for improved photovoltaic devices*, Nat Mater **9**, 205 (2010).

[36] G. Baker and D. Moore, *Progress in plasmonic engineering of surface-enhanced Raman-scattering substrates toward ultra-trace analysis*, Anal Bioanal Chem **382**, 1751 (2005).

[37] B. Huang, M. Bates, and X. Zhuang, *Super-Resolution Fluorescence Microscopy*, Annual Review of Biochemistry **78**, 993 (2009).

[38] L. Schermelleh, R. Heintzmann, and H. Leonhardt, *A guide to super-resolution fluorescence microscopy*, The Journal of Cell Biology **190**, 165 (2010).

[39] T. Brixner, J. Stenger, H. M. Vaswani, M. Cho, R. E. Blankenship, and G. R. Fleming, *Two-dimensional spectroscopy of electronic couplings in photosynthesis*, Nature **434**, 625 (2005).

[40] G. S. Engel, T. R. Calhoun, E. L. Read, T.-K. Ahn, T. Mancal, Y.-C. Cheng, R. E. Blankenship, and G. R. Fleming, *Evidence for wavelike energy transfer through quantum coherence in photosynthetic systems*, Nature **446**, 782 (2007).

[41] R. H. Friend, R. W. Gymer, A. B. Holmes, J. H. Burroughes, R. N. Marks, C. Taliani, D. D. C. Bradley, D. A. D. Santos, J. L. Bredas, M. Logdlund, and W. R. Salaneck, *Electroluminescence in conjugated polymers*, Nature **397**, 121 (1999).

[42] S. Coe, W.-K. Woo, M. Bawendi, and V. Bulovic, *Electroluminescence from single monolayers of nanocrystals in molecular organic devices*, Nature **420**, 800 (2002).

[43] E. F. Schubert, T. Gessmann, and J. K. Kim, in *Kirk-Othmer Encyclopedia of Chemical Technology* (John Wiley & Sons, Inc., 2000).

[44] P. A. Franken, A. E. Hill, C. W. Peters, and G. Weinreich, *Generation of Optical Harmonics*, Phys. Rev. Lett. **7**, 118 (1961).

[45] P. M. Paul, E. S. Toma, P. Breger, G. Mullot, Aug, xe, F., B. Ph, H. G. Muller, and P. Agostini, *Observation of a Train of Attosecond Pulses from High Harmonic Generation*, Science **292**, 1689 (2001).

[46] B. Ferguson and X.-C. Zhang, *Materials for terahertz science and technology*, Nat Mater **1**, 26 (2002).

[47] B. B. Hu and M. C. Nuss, *Imaging with terahertz waves*, Opt. Lett. **20**, 1716 (1995).

[48] M. Tonouchi, *Cutting-edge terahertz technology*, Nat Photon **1**, 97 (2007).

[49] P. L. Knight and P. W. Milonni, *The Rabi frequency in optical spectra*, Physics Reports **66**, 21 (1980).

[50] K. J. Boller, A. Imamoğlu, and S. E. Harris, *Observation of electromagnetically induced transparency*, Phys. Rev. Lett. **66**, 2593 (1991).

[51] S. Andrew, *Quantum computing*, Reports on Progress in Physics **61**, 117 (1998).

[52] C. Bennett, E. Bernstein, G. Brassard, and U. Vazirani, *Strengths and Weaknesses of Quantum Computing*, SIAM Journal on Computing **26**, 1510 (1997).

[53] D. Loss and D. P. DiVincenzo, *Quantum computation with quantum dots*, Phys. Rev. A **57**, 120 (1998).

[54] P. Kok, W. J. Munro, K. Nemoto, T. C. Ralph, J. P. Dowling, and G. J. Milburn, *Linear optical quantum computing with photonic qubits*, Reviews of Modern Physics **79**, 135 (2007).

[55] H. Bernien, B. Hensen, W. Pfaff, G. Koolstra, M. S. Blok, L. Robledo, T. H. Taminiau, M. Markham, D. J. Twitchen, L. Childress, and R. Hanson, *Heralded entanglement between solid-state qubits separated by three metres*, Nature **497**, 86 (2013).

[56] M. Levin and X.-G. Wen, *\textit{Colloquium} : Photons and electrons as emergent phenomena*, Reviews of Modern Physics **77**, 871 (2005).

[57] G. Vidal, *Class of Quantum Many-Body States That Can Be Efficiently Simulated*, Phys. Rev. Lett. **101**, 110501 (2008).

[58] E. Dagotto, *Complexity in Strongly Correlated Electronic Systems*, Science **309**, 257 (2005).

[59] J. Toner and Y. Tu, *Flocks, herds, and schools: A quantitative theory of flocking*, Phys. Rev. E **58**, 4828 (1998).

[60] K. T. Law, P. A. Lee, and T. K. Ng, *Majorana Fermion Induced Resonant Andreev Reflection*, Phys. Rev. Lett. **103**, 237001 (2009).

[61] J. J. Hopfield, *Theory of the Contribution of Excitons to the Complex Dielectric Constant of Crystals*, Phys. Rev. **112**, 1555 (1958).

[62] B. Laikhtman, *Are excitons really bosons?*, Journal of Physics: Condensed Matter **19**, 295214 (2007).

[63] M. A. Lampert, *Mobile and Immobile Effective-Mass-Particle Complexes in Nonmetallic Solids*, Phys. Rev. Lett. **1**, 450 (1958).

[64] D. Brinkmann, J. Kudrna, P. Gilliot, B. Honerlage, A. Arnoult, J. Cibert, and S. Tatarenko, *Trion and exciton dephasing measurements in modulation-doped quantum wells: A probe for trion and carrier localization*, Phys. Rev. B **60**, 4474 (1999).

[65] B. L. Evans and P. A. Young, *Optical Absorption and Dispersion in Molybdenum Disulphide*, Proceedings of the Royal Society of London. Series A. Mathematical and Physical Sciences **284**, 402 (1965).

[66] G. H. Wannier, *The Structure of Electronic Excitation Levels in Insulating Crystals*, Phys. Rev. **52**, 191 (1937).

[67] Y. Sun, N. C. Giebink, H. Kanno, B. Ma, M. E. Thompson, and S. R. Forrest, *Management of singlet and triplet excitons for efficient white organic light-emitting devices*, Nature **440**, 908 (2006).

[68] R. D. Schaller and V. I. Klimov, *High Efficiency Carrier Multiplication in PbSe Nanocrystals: Implications for Solar Energy Conversion*, Phys. Rev. Lett. **92**, 186601 (2004).

[69] P. Neumann, N. Mizuochi, F. Rempp, P. Hemmer, H. Watanabe, S. Yamasaki, V. Jacques, T. Gaebel, F. Jelezko, and J. Wrachtrup, *Multipartite Entanglement Among Single Spins in Diamond*, Science **320**, 1326 (2008).

[70] D. Rugar, R. Budakian, H. J. Mamin, and B. W. Chui, *Single spin detection by magnetic resonance force microscopy*, Nature **430**, 329 (2004).

[71] K. Saeedi, S. Simmons, J. Z. Salvail, P. Dluhy, H. Riemann, N. V. Abrosimov, P. Becker, H.-J. Pohl, J. J. L. Morton, and M. L. W. Thewalt, *Room-Temperature Quantum Bit Storage Exceeding 39 Minutes Using Ionized Donors in Silicon-28*, Science **342**, 830 (2013).

[72] K.-H. Pantke, V. G. Lyssenko, B. S. Razbirin, H. Schwab, J. Erland, and J. M. Hvam, *Coherent and Incoherent Exciton Dynamics in II-VI Semiconductors*, Phys. Stat. Sol. (b) **173**, 69 (1992).

[73] G. Finkelstein, V. Umansky, I. Bar-Joseph, V. Ciulin, S. Haacke, J.-D. Ganiere, and B. Deveaud, *Charged exciton dynamics in GaAs quantum wells*, Phys. Rev. B **58**, 12637 (1998).

[74] M. Hentschel, R. Kienberger, C. Spielmann, G. A. Reider, N. Milosevic, T. Brabec, P. Corkum, U. Heinzmann, M. Drescher, and F. Krausz, *Attosecond metrology*, Nature **414**, 509 (2001).

[75] A. Reina, X. Jia, J. Ho, D. Nezich, H. Son, V. Bulovic, M. S. Dresselhaus, and J. Kong, *Large area, few-layer graphene films on arbitrary substrates by chemical vapor deposition*, Nano Letters **9**, 30 (2008).

[76] J.-J. Wu and S.-C. Liu, *Low-temperature growth of well-aligned ZnO nanorods by chemical vapor deposition*, Advanced Materials **14**, 215 (2002).

[77] B. F. Feuerbacher, J. Kuhl, R. Eccleston, and K. Ploog, *Quantum beats between the light and heavy hole excitons in a quantum well*, Solid State Communications **74**, 1279 (1990).

[78] E. O. Göbel, K. Leo, T. C. Damen, J. Shah, S. Schmitt-Rink, W. Schäfer, J. F. Müller, and K. Köhler, *Quantum beats of excitons in quantum wells*, Phys. Rev. Lett. **64**, 1801 (1990).

[79] K. Leo, J. Shah, E. O. Göbel, T. C. Damen, S. Schmitt-Rink, W. Schäfer, and K. Köhler, *Coherent oscillations of a wave packet in a semiconductor double-quantum-well structure*, Phys. Rev. Lett. **66**, 201 (1991).

[80] M. Z. Maialle, E. A. de Andrada e Silva, and L. J. Sham, *Exciton spin dynamics in quantum wells*, Phys. Rev. B **47**, 15776 (1993).

[81] T. C. Damen, L. Via, J. E. Cunningham, J. Shah, and L. J. Sham, *Subpicosecond spin relaxation dynamics of excitons and free carriers in GaAs quantum wells*, Phys. Rev. Lett. **67**, 3432 (1991).

[82] K. S. Novoselov, D. Jiang, F. Schedin, T. J. Booth, V. V. Khotkevich, S. V. Morozov, and A. K. Geim, *Two-dimensional atomic crystals*, Proceedings of the National Academy of Sciences of the United States of America **102**, 10451 (2005).

[83] Z. Jin, J. Yao, C. Kittrell, and J. M. Tour, *Large-Scale Growth and Characterizations of Nitrogen-Doped Monolayer Graphene Sheets*, ACS Nano **5**, 4112 (2011).

[84] S. Das Sarma, S. Adam, E. H. Hwang, and E. Rossi, *Electronic transport in two-dimensional graphene*, Reviews of Modern Physics **83**, 407 (2011).

[85] A. Splendiani, L. Sun, Y. Zhang, T. Li, J. Kim, C. Y. Chim, G. Galli, and F. Wang, *Emerging photoluminescence in monolayer MoS2*, Nano Letters **10**, 1271 (2010).

[86] K. F. Mak, C. Lee, J. Hone, J. Shan, and T. F. Heinz, *Atomically Thin MoS2: A New Direct-Gap Semiconductor*, Phys. Rev. Lett. **105**, 136805 (2010).

[87] Y. Zhang, T.-R. Chang, B. Zhou, Y.-T. Cui, H. Yan, Z. Liu, F. Schmitt, J. Lee, R. Moore, Y. Chen, H. Lin, H.-T. Jeng, S.-K. Mo, Z. Hussain, A. Bansil, and Z.-X. Shen, *Direct observation of the transition from indirect to direct bandgap in atomically thin epitaxial MoSe2*, Nat Nano **9**, 111 (2014).

[88] C. Zhang, A. Johnson, C.-L. Hsu, L.-J. Li, and C.-K. Shih, *Direct Imaging of Band Profile in Single Layer MoS2 on Graphite: Quasiparticle Energy Gap, Metallic Edge States, and Edge Band Bending*, Nano Letters **14**, 2443 (2014).

[89] R. F. Frindt, *OPTICAL ABSORPTION OF A FEW UNIT-CELL LAYERS OF MOS2*, Phys. Rev. **140**, A536 (1965).

[90] M. Fontana, T. Deppe, A. K. Boyd, M. Rinzan, A. Y. Liu, M. Paranjape, and P. Barbara, *Electron-hole transport and photovoltaic effect in gated MoS2 Schottky junctions*, Sci. Rep. **3**, 1634, 1634 (2013).

[91] A. Chernikov, T. C. Berkelbach, H. M. Hill, A. Rigosi, Y. Li, O. B. Aslan, D. R. Reichman, M. S. Hybertsen, and T. F. Heinz, *Exciton Binding Energy and Nonhydrogenic Rydberg Series in Monolayer WS2*, Phys. Rev. Lett. **113**, 076802 (2014).

[92] A. R. Klots, A. K. Newaz, B. Wang, D. Prasai, H. Krzyzanowska, J. Lin, D. Caudel, N. J. Ghimire, J. Yan, B. L. Ivanov, K. A. Velizhanin, A. Burger, D. G. Mandrus, N. H. Tolk, S. T. Pantelides, and K. I. Bolotin, *Probing excitonic states in suspended two-dimensional semiconductors by photocurrent spectroscopy*, Sci. Rep. **4**, 6608 (2014).

[93] H. Zeng, J. Dai, W. Yao, D. Xiao, and X. Cui, *Valley polarization in MoS2 monolayers by optical pumping*, Nat Nano **7**, 490 (2012).

[94] D. Xiao, G.-B. Liu, W. Feng, X. Xu, and W. Yao, *Coupled Spin and Valley Physics in Monolayers of MoS_{2} and Other Group-VI Dichalcogenides*, Phys. Rev. Lett. **108**, 196802 (2012).

[95] K. He, C. Poole, K. F. Mak, and J. Shan, *Experimental demonstration of continuous electronic structure tuning via strain in atomically thin MoS2*, Nano Letters **13**, 2931 (2013).

[96] Y. Y. Hui, X. Liu, W. Jie, N. Y. Chan, J. Hao, Y.-T. Hsu, L.-J. Li, W. Guo, and S. P. Lau, *Exceptional Tunability of Band Energy in a Compressively Strained Trilayer MoS2 Sheet*, ACS Nano **7**, 7126 (2013).

[97] A. K. Geim and I. V. Grigorieva, *Van der Waals heterostructures*, Nature **499**, 419 (2013).

[98] K. Kosmider and J. Fernandez-Rossier, *Electronic properties of the MoS2-WS2 heterojunction*, Phys. Rev. B **87**, 075451, 075451 (2013).

[99] O. Lopez-Sanchez, D. Lembke, M. Kayci, A. Radenovic, and A. Kis, *Ultrasensitive photodetectors based on monolayer MoS2*, Nat Nano **8**, 497 (2013).

[100] J. S. Ross, P. Klement, A. M. Jones, N. J. Ghimire, J. Yan, D. G. Mandrus, T. Taniguchi, K. Watanabe, K. Kitamura, W. Yao, D. H. Cobden, and X. Xu, *Electrically tunable excitonic light-emitting diodes based on monolayer WSe2 p-n junctions*, Nat Nano **9**, 268 (2014).

[101] Y. J. Zhang, T. Oka, R. Suzuki, J. T. Ye, and Y. Iwasa, *Electrically Switchable Chiral Light-Emitting Transistor*, Science **344**, 725 (2014).

[102] G. H. Li, A. Luican, J. dos Santos, A. H. C. Neto, A. Reina, J. Kong, and E. Y. Andrei, *Observation of Van Hove singularities in twisted graphene layers*, Nat Phys **6**, 109 (2010).

[103] K. C. Hall and M. E. Flatté, *Performance of a spin-based insulated gate field effect transistor* App. Phys. Lett. **88** (2006).

[104] Z. H. Xiong, D. Wu, Z. V. Vardeny, and J. Sh, *Giant magnetoresistance in organic spin-valves*, Nature **427** (2004).

[105] J.-E. Wegrowe, A. Fábián, P. Guittienne, X. Hoffer, D. Kelly, J.-P. Ansermet, and E. Olive, *Exchange torque and spin transfer between spin polarized current and ferromagnetic layers* App. Phys. Lett. **80** (2002).

[106] V. Sih, W. Lau, R. Myers, V. Horowitz, A. Gossard, and D. Awschalom, *Generating Spin Currents in Semiconductors with the Spin Hall Effect*, Phys. Rev. Lett. **97** (2006).

[107] E. Vanelle, M. Paillard, X. Marie, T. Amand, P. Gilliot, D. Brinkmann, R. Levy, J. Cibert, and S. Tatarenko, *Spin coherence and formation dynamics of charged excitons in CdTe/CdMgZnTe quantum wells*, Phys. Rev. B **62**, 2696 (2000).

[108] T. Cao, G. Wang, W. Han, H. Ye, C. Zhu, J. Shi, Q. Niu, P. Tan, E. Wang, B. Liu, and J. Feng, *Valley-selective circular dichroism of monolayer molybdenum disulphide*, Nat Comm **3**, 887 (2012).

[109] K. F. Mak, K. He, J. Shan, and T. F. Heinz, *Control of valley polarization in monolayer MoS2 by optical helicity*, Nat Nano **7**, 494 (2012).

[110] C. Kittel, *Introduction to solid state physics* (Wiley, 2005).

[111] P. Vogl, H. P. Hjalmarson, and J. D. Dow, *A Semi-empirical tight-binding theory of the electronic structure of semiconductors†*, Journal of Physics and Chemistry of Solids **44**, 365 (1983).

[112] M. C. Beard, K. P. Knutsen, P. Yu, J. M. Luther, Q. Song, W. K. Metzger, R. J. Ellingson, and A. J. Nozik, *Multiple Exciton Generation in Colloidal Silicon Nanocrystals*, Nano Letters **7**, 2506 (2007).

[113] R. C. Miller, D. A. Kleinman, W. T. Tsang, and A. C. Gossard, *Observation of the excited level of excitons in GaAs quantum wells*, Phys. Rev. B **24**, 1134 (1981).

[114] P. W. Baumeister, *Optical absorption of cuprous oxide*, Phys. Rev. **121**, 359 (1961).

[115] T. Kazimierczuk, D. Frohlich, S. Scheel, H. Stolz, and M. Bayer, *Giant Rydberg excitons in the copper oxide Cu2O*, Nature **514**, 343 (2014).

[116] Y. U. Peter and M. Cardona, *Fundamentals of semiconductors: physics and materials properties* (Springer Science & Business Media, 2010).

[117] J. Lee, S. S. Kim, K. Kim, J. H. Kim, and S. Im, *Correlation between photoelectric and optical absorption spectra of thermally evaporated pentacene films*, App. Phys. Lett. **84**, 1701 (2004).

[118] N. Peyghambarian, S. W. Koch, and A. Mysyrowicz, *Introduction to semiconductor optics* (Prentice-Hall, Inc., 1994).

[119] G. Itskos, G. Heliotis, P. G. Lagoudakis, J. Lupton, N. P. Barradas, E. Alves, S. Pereira, I. M. Watson, M. D. Dawson, and J. Feldmann, *Efficient dipole-dipole coupling of Mott-Wannier and Frenkel excitons in (Ga, In) N quantum well/polyfluorene semiconductor heterostructures*, Phys. Rev. B **76**, 035344 (2007).

[120] V. M. Agranovich, D. M. Basko, G. C. La Rocca, and F. Bassani, *Excitons and optical nonlinearities in hybrid organic-inorganic nanostructures*, Journal of Physics: Condensed Matter **10**, 9369 (1998).

[121] N. Scheuschner, O. Ochedowski, A.-M. Kaulitz, R. Gillen, M. Schleberger, and J. Maultzsch, *Photoluminescence of freestanding single- and few-layer MoS2*, Phys. Rev. B **89**, 125406 (2014).

[122] K. F. Mak, K. He, C. Lee, G. H. Lee, J. Hone, T. F. Heinz, and J. Shan, *Tightly bound trions in monolayer MoS2*, Nat Mater **12**, 207 (2013).

[123] R. Bratschitsch, Z. Chen, S. T. Cundiff, E. A. Zhukov, D. R. Yakovlev, M. Bayer, G. Karczewski, T. Wojtowicz, and J. Kossut, *Electron spin coherence in n-doped CdTe⁄CdMgTe quantum wells*, App. Phys. Lett. **89** (2006).

[124] G. Wang, L. Bouet, D. Lagarde, M. Vidal, A. Balocchi, T. Amand, X. Marie, and B. Urbaszek, *Valley dynamics probed through charged and neutral exciton emission in monolayer WSe2*, Phys. Rev. B **90**, 075413 (2014).

[125] E. Vanelle, D. Brinkmann, M. Paillard, X. Marie, T. Amand, P. Gilliot, B. Honerlage, J. Cibert, and S. Tatarenko, *Spin Coherence and Formation Dynamics of Charged Excitons in CdTe/CdMgZnTe Quantum Well*, Phys. Stat. Sol. **178**, 2000 (2000).

[126] M. Hagn, A. Zrenner, G. Böhm, and G. Weimann, *Electric-field-induced exciton transport in coupled quantum well structures*, App. Phys. Lett. **67**, 232 (1995).

[127] J. Rudolph, R. Hey, and P. V. Santos, *Long-range exciton transport by dynamic strain fields in a GaAs quantum well*, Phys. Rev. Lett. **99**, 047602 (2007).

[128] D. Sanvitto, F. Pulizzi, A. J. Shields, P. C. M. Christianen, S. N. Holmes, M. Y. Simmons, D. A. Ritchie, J. C. Maan, and M. Pepper, *Observation of Charge Transport by Negatively Charged Excitons*, Science **294**, 837 (2001).

[129] J. S. Ross, Wu, S., Yu, H., Ghimire, N. J., Jones, A., Aivazian, G., Yan, J., Mandrus, D. G., Xiao, D., Yao, W., Xu, X., *Electrical control of neutral and charged excitons in a monolayer semiconductor*, Nat Comm **4**, 1474 (2013).

[130] E. Collini, C. Y. Wong, K. E. Wilk, P. M. G. Curmi, P. Brumer, and G. D. Scholes, *Coherently wired light-harvesting in photosynthetic marine algae at ambient temperature*, Nature **463**, 644 (2010).

[131] R. Q. Yang, B. H. Yang, D. Zhang, C.-H. Lin, S. J. Murry, H. Wu, and S. S. Pei, *High power mid-infrared interband cascade lasers based on type-II quantum wells*, App. Phys. Lett. **71**, 2409 (1997).

[132] J. R. Meyer, C. A. Hoffman, F. J. Bartoli, and L. R. Ram-Mohan, *Type-II quantum-well lasers for the mid-wavelength infrared*, App. Phys. Lett. **67**, 757 (1995).

[133] J. Hu, X. G. Xu, J. A. H. Stotz, S. P. Watkins, A. E. Curzon, M. L. W. Thewalt, N. Matine, and C. R. Bolognesi, *Type II photoluminescence and conduction band offsets of GaAsSb/InGaAs and GaAsSb/InP heterostructures grown by metalorganic vapor phase epitaxy*, App. Phys. Lett. **73**, 2799 (1998).

[134] H. W. van Kesteren, E. C. Cosman, W. A. J. A. van der Poel, and C. T. Foxon, *Fine structure of excitons in type-II GaAs/AlAs quantum wells*, Phys. Rev. B **41**, 5283 (1990).

[135] F. Hatami, N. N. Ledentsov, M. Grundmann, J. Böhrer, F. Heinrichsdorff, M. Beer, D. Bimberg, S. S. Ruvimov, P. Werner, U. Gösele, J. Heydenreich, U. Richter, S. V. Ivanov, B. Y. Meltser, P. S. Kop'ev, and Z. I. Alferov, *Radiative recombination in type-II GaSb/GaAs quantum dots*, App. Phys. Lett. **67**, 656 (1995).

[136] G. Dresselhaus, *Spin-Orbit Coupling Effects in Zinc Blende Structures*, Phys. Rev. **100**, 580 (1955).

[137] J. S. Blakemore, *Semiconducting and other major properties of gallium arsenide*, J. App. Phys. **53**, R123 (1982).

[138] L. C. Andreani, A. Pasquarello, and F. Bassani, *Hole subbands in strained GaAs-Ga 1−x Al x As quantum wells: Exact solution of the effective-mass equation*, Phys. Rev. B **36**, 5887 (1987).

[139] D. J. Hilton and C. L. Tang, *Optical Orientation and Femtosecond Relaxation of Spin-Polarized Holes in GaAs*, Phys. Rev. Lett. **89**, 146601 (2002).

[140] S. Bar-Ad and I. Bar-Joseph, *Exciton spin dynamics in GaAs heterostructures*, Phys. Rev. Lett. **68**, 349 (1992).

[141] X. Marie, T. Amand, P. Le Jeune, M. Paillard, P. Renucci, L. E. Golub, V. D. Dymnikov, and E. L. Ivchenko, *Hole spin quantum beats in quantum-well structures*, Phys. Rev. B **60**, 5811 (1999).

[142] A. P. Heberle, W. W. Rühle, and K. Ploog, *Quantum beats of electron Larmor precession in GaAs wells*, Phys. Rev. Lett. **72**, 3887 (1994).

[143] M. T. Portella-Oberli, J. Berney, L. Kappei, F. Morier-Genoud, J. Szczytko, and B. Deveaud-Pledran, *Dynamics of Trion Formation in InxGa1-xAs QuantumWells*, Phys. Rev. Lett. **102**, 096402 (2009).

[144] G. Finkelstein, H. Shtrikman, and I. Bar-Joseph, *Negatively and positively charged excitons in $\mathrm{GaAs}/{\mathrm{Al}}_{x}{\mathrm{Ga}}_{1-x}\mathrm{As}$ quantum wells*, Phys. Rev. B **53**, R1709 (1996).

[145] SuzukiR, SakanoM, Y. J. Zhang, AkashiR, MorikawaD, HarasawaA, YajiK, KurodaK, MiyamotoK, OkudaT, IshizakaK, AritaR, and IwasaY, *Valley-dependent spin polarization in bulk MoS2 with broken inversion symmetry*, Nat Nano **9**, 611 (2014).

[146] S. Wu, J. S. Ross, G.-B. Liu, G. Aivazian, A. Jones, Z. Fei, W. Zhu, D. Xiao, W. Yao, D. Cobden, and X. Xu, *Electrical tuning of valley magnetic moment through symmetry control in bilayer MoS2*, Nat Phys **9**, 149 (2013).

[147] M. Amani, D.-H. Lien, D. Kiriya, J. Xiao, A. Azcatl, J. Noh, S. R. Madhvapathy, R. Addou, K. C. Santosh, and M. Dubey, *Near-unity photoluminescence quantum yield in MoS2*, Science **350**, 1065 (2015).

[148] A. M. Jones, H. Yu, N. J. Ghimire, S. Wu, G. Aivazian, J. S. Ross, B. Zhao, J. Yan, D. G. Mandrus, D. Xiao, W. Yao, and X. Xu, *Optical generation of excitonic valley coherence in monolayer WSe2*, Nat Nano **8**, 634 (2013).

[149] K. F. Mak, K. L. McGill, J. Park, and P. L. McEuen, *The valley Hall effect in MoS2 transistors*, Science **344**, 1489 (2014).

[150] Y.-M. He, G. Clark, J. R. Schaibley, Y. He, M.-C. Chen, Y.-J. Wei, X. Ding, Q. Zhang, W. Yao, X. Xu, C.-Y. Lu, and J.-W. Pan, *Single quantum emitters in monolayer semiconductors*, Nat Nano **10**, 497 (2015).

[151] M. Koperski, K. Nogajewski, A. Arora, V. Cherkez, P. Mallet, J.-Y. Veuillen, J. Marcus, P. Kossacki, and M. Potemski, *Single photon emitters in exfoliated WSe2 structures*, Nat Nano **10**, 503 (2015).

[152] A. Srivastava, M. Sidler, A. V. Allain, D. S. Lembke, A. Kis, and A. Imamoğlu, *Optically active quantum dots in monolayer WSe2*, Nat Nano **10**, 491 (2015).

[153] G. Rubio-Bollinger, R. Guerrero, D. de Lara, J. Quereda, L. Vaquero-Garzon, N. Agraït, R. Bratschitsch, and A. Castellanos-Gomez, *Enhanced Visibility of MoS2, MoSe2, WSe2 and Black-Phosphorus: Making Optical Identification of 2D Semiconductors Easier*, Electronics **4**, 847 (2015).

[154] Y. Huang, E. Sutter, N. N. Shi, J. Zheng, T. Yang, D. Englund, H.-J. Gao, and P. Sutter, *Reliable Exfoliation of Large-Area High-Quality Flakes of Graphene and Other Two-Dimensional Materials*, ACS Nano **9**, 10612 (2015).

[155] X. S. Li, W. W. Cai, J. H. An, S. Kim, J. Nah, D. X. Yang, R. Piner, A. Velamakanni, I. Jung, E. Tutuc, S. K. Banerjee, L. Colombo, and R. S. Ruoff, *Large-Area Synthesis of High-Quality and Uniform Graphene Films on Copper Foils*, Science **324**, 1312 (2009).

[156] J. N. Coleman, M. Lotya, A. O'Neill, S. D. Bergin, P. J. King, U. Khan, K. Young, A. Gaucher, S. De, R. J. Smith, I. V. Shvets, S. K. Arora, G. Stanton, H. Y. Kim,

K. Lee, G. T. Kim, G. S. Duesberg, T. Hallam, J. J. Boland, J. J. Wang, J. F. Donegan, J. C. Grunlan, G. Moriarty, A. Shmeliov, R. J. Nicholls, J. M. Perkins, E. M. Grieveson, K. Theuwissen, D. W. McComb, P. D. Nellist, and V. Nicolosi, *Two-Dimensional Nanosheets Produced by Liquid Exfoliation of Layered Materials*, Science **331**, 568 (2011).

[157] Y. H. Lee, X. Q. Zhang, W. Zhang, M. T. Chang, C. T. Lin, K. D. Chang, Y. C. Yu, J. T. W. Wang, C. S. Chang, and L. J. Li, *Synthesis of Large-Area MoS2 Atomic Layers with Chemical Vapor Deposition*, Advanced Materials **24**, 2320 (2012).

[158] J.-K. Huang, J. Pu, C.-L. Hsu, M.-H. Chiu, Z.-Y. Juang, Y.-H. Chang, W.-H. Chang, Y. Iwasa, T. Takenobu, and L.-J. Li, *Large-Area Synthesis of Highly Crystalline WSe2 Monolayers and Device Applications*, ACS Nano **8**, 923 (2013).

[159] A. Singh, G. Moody, K. Tran, M. E. Scott, V. Overbeck, G. Berghäuser, J. Schaibley, E. J. Seifert, D. Pleskot, N. M. Gabor, J. Yan, D. G. Mandrus, M. Richter, E. Malic, X. Xu, and X. Li, *Trion formation dynamics in monolayer transition metal dichalcogenides*, Phys. Rev. B **93**, 041401(R) (2016).

[160] D. Geng, B. Wu, Y. Guo, L. Huang, Y. Xue, J. Chen, G. Yu, L. Jiang, W. Hu, and Y. Liu, *Uniform hexagonal graphene flakes and films grown on liquid copper surface*, Proceedings of the National Academy of Sciences **109**, 7992 (2012).

[161] S. Najmaei, Z. Liu, W. Zhou, X. Zou, G. Shi, S. Lei, B. I. Yakobson, J.-C. Idrobo, P. M. Ajayan, and J. Lou, *Vapour phase growth and grain boundary structure of molybdenum disulphide atomic layers*, Nat Mater **12**, 754 (2013).

[162] A. Castellanos-Gomez, N. Agraït, and G. Rubio-Bollinger, *Optical identification of atomically thin dichalcogenide crystals*, App. Phys. Lett. **96**, 213116 (2010).

[163] H. Li, G. Lu, Z. Yin, Q. He, H. Li, Q. Zhang, and H. Zhang, *Optical Identification of Single-and Few-Layer MoS2 Sheets*, Small **8**, 682 (2012).

[164] P. Tonndorf, R. Schmidt, P. Bottger, X. Zhang, J. Borner, A. Liebig, M. Albrecht, C. Kloc, O. Gordan, D. R. T. Zahn, S. M. de Vasconcellos, and R. Bratschitsch, *Photoluminescence emission and Raman response of monolayer MoS2, MoSe2, and WSe2*, Optics Express **21**, 4908 (2013).

[165] H. J. Conley, B. Wang, J. I. Ziegler, R. F. Haglund, Jr., S. T. Pantelides, and K. I. Bolotin, *Bandgap engineering of strained monolayer and bilayer MoS2*, Nano Letters **13**, 3626 (2013).

[166] H. Li, Q. Zhang, C. C. R. Yap, B. K. Tay, T. H. T. Edwin, A. Olivier, and D. Baillargeat, *From bulk to monolayer MoS2: evolution of Raman scattering*, Advanced Functional Materials **22**, 1385 (2012).

[167] H. Sahin, S. Tongay, S. Horzum, W. Fan, J. Zhou, J. Li, J. Wu, and F. M. Peeters, *Anomalous Raman spectra and thickness-dependent electronic properties of WSe${}_{2}$*, Phys. Rev. B **87**, 165409 (2013).

[168] S. Mouri, Y. Miyauchi, and K. Matsuda, *Tunable photoluminescence of monolayer MoS(2) via chemical doping*, Nano Letters **13**, 5944 (2013).

[169] H.-P. Komsa and A. V. Krasheninnikov, *Effects of confinement and environment on the electronic structure and exciton binding energy of MoS${}_{2}$ from first principles*, Phys. Rev. B **86**, 241201 (2012).

[170] R. W. Boyd, *Nonlinear optics* (Academic press, 2003).

[171] M. M. Fejer, *Nonlinear optical frequency conversion*, Physics Today **47**, 25 (1994).

[172] X. Li, J. Willits, S. T. Cundiff, I. M. P. Aarts, A. A. E. Stevens, and D. S. Dessau, *Circular dichroism in second harmonic generation from oxidized Si (001)*, App. Phys. Lett. **89**, 022102 (2006).

[173] R. M. Corn and D. A. Higgins, *Optical second harmonic generation as a probe of surface chemistry*, Chemical Reviews **94**, 107 (1994).

[174] H. Wang, K. Ferrio, D. G. Steel, Y. Z. Hu, R. Binder, and S. W. Koch, *Transient Nonlinear Optical Response from Excitation Induced Dephasing in GaAs*, Phys. Rev. Lett. **71**, 1261 (1993).

[175] D. Walrod, S. Y. Auyang, P. A. Wolff, and M. Sugimoto, *Observation of third order optical nonlinearity due to intersubband transitions in AlGaAs/GaAs superlattices*, App. Phys. Lett. **59**, 2932 (1991).

[176] F. L. Madarasz, F. Szmulowicz, F. K. Hopkins, and D. L. Dorsey, *Calculation of giant third-order nonlinear susceptibilities due to excitonic processes in rectangular GaAs quantum well wires*, J. App. Phys. **75**, 639 (1994).

[177] R. del Coso and J. Solis, *Relation between nonlinear refractive index and third-order susceptibility in absorbing media*, Journal of the Optical Society of America B **21**, 640 (2004).

[178] S. S. Jha and N. Bloembergen, *Nonlinear optical susceptibilities in group-IV and III-V semiconductors*, Phys. Rev. **171**, 891 (1968).

[179] R. Wang, B. A. Ruzicka, N. Kumar, M. Z. Bellus, H.-Y. Chiu, and H. Zhao, *Ultrafast and Spatially Resolved Studies of Charge Carriers in Atomically Thin Molybdenum Disulfide*, Phys. Rev. B **86**, 045406 (2012).

[180] G. Moody, C. K. Dass, K. Hao, C.-H. Chen, L.-J. Li, A. Singh, K. Tran, G. Clark, X. Xu, G. Bergäuser, E. Malic, A. Knorr, and X. Li, *Intrinsic homogeneous linewidth and broadening mechanisms of excitons in monolayer transition metal dichalcogenides*, Nat Comm **6**, 8315 (2015).

[181] M. E. Siemens, G. Moody, H. B. Li, A. D. Bristow, and S. T. Cundiff, *Resonance lineshapes in two-dimensional Fourier transform spectroscopy*, Optics Express **18**, 17699 (2010).

[182] W. R. Rapoport and C. P. Khattak, *Titanium sapphire laser characteristics*, Appl. Opt. **27**, 2677 (1988).

[183] J. P. Heritage, A. M. Weiner, and R. N. Thurston, *Picosecond pulse shaping by spectral phase and amplitude manipulation*, Opt. Lett. **10**, 609 (1985).

[184] T. Tanabe, H. Tanabe, Y. Teramura, and F. Kannari, *Spatiotemporal measurements based on spatial spectral interferometry for ultrashort optical pulses shaped by a Fourier pulse shaper*, Journal of the Optical Society of America B **19**, 2795 (2002).

[185] S. Akturk, X. Gu, M. Kimmel, and R. Trebino, *Extremely simple single-prism ultrashort-pulse compressor*, Optics Express **14**, 10101 (2006).

[186] X. Yin, Z. Ye, D. A. Chenet, Y. Ye, K. O'Brien, J. C. Hone, and X. Zhang, *Edge Nonlinear Optics on a MoS2 Atomic Monolayer*, Science **344**, 488 (2014).

[187] P. F. Moulton, *Spectroscopic and laser characteristics of Ti:Al2O3*, Journal of the Optical Society of America B **3**, 125 (1986).

[188] J. F. Pinto, L. Esterowitz, G. H. Rosenblatt, M. Kokta, and D. Peressini, *Improved Ti:sapphire laser performance with new high figure of merit crystals*, Quantum Electronics, IEEE Journal of **30**, 2612 (1994).

[189] H. O. McMahon and W. E. Gifford, in *Advances in Cryogenic Engineering* (Springer, 1960), pp. 354.

[190] H. Yoshimura, M. Nagao, T. Inaguchi, T. Yamada, and M. Iwamoto, *Helium liquefaction by a Gifford–McMahon cycle cryogenic refrigerator*, Review of Scientific Instruments **60**, 3533 (1989).

[191] T. Korn, S. Heydrich, M. Hirmer, J. Schmutzler, and C. Schüller, *Low-temperature photocarrier dynamics in monolayer MoS2*, App. Phys. Lett. **99**, 102109 (2011).

[192] J. D. Lin, C. Han, FeiWang, RuiWang, D. Xiang, S. Qin, X.-A. Zhang, LiWang, H. Zhang, A. Thye, ShenWee, and W. Chen, *Electron-Doping-Enhanced Trion Formation in Monolayer Molybdenum Disulfide Functionalized with Cesium Carbonate*, ACS Nano **8**, 5323 (2014).

[193] H. Shi, R. Yan, S. Bertolazzi, J. Brivio, B. Gao, A. Kis, D. Jena, H. Xing, and L. Huang, *Exciton Dynamics in Suspended Monolayer and Few-Layer MoS2 2D Crystals*, ACS Nano **7**, 1072 (2013).

[194] S. Sim, J. Park, J.-G. Song, C. In, Y.-S. Lee, H. Kim, and H. Choi, *Exciton Dynamics in Atomically thin MoS2: Interexcitonic Interaction and Broadening Kinetics*, Phys. Rev. B **88**, 075434 (2013).

[195] C. Mai, A. Barrette, Y. Yu, Y. G. Semenov, K. W. Kim, L. Cao, and K. Gundogdu, *Many-body effects in valleytronics: direct measurement of valley lifetimes in single-layer MoS2*, Nano Letters **14**, 202 (2014).

[196] E. J. Sie, A. J. Frenzel, Y.-H. Lee, J. Kong, and N. Gedik, *Intervalley biexcitons and many-body effects in monolayer ${\mathrm{MoS}}_{2}$*, Phys. Rev. B **92**, 125417 (2015).

[197] L. Britnell, R. V. Gorbachev, R. Jalil, B. D. Belle, F. Schedin, M. I. Katsnelson, L. Eaves, S. V. Morozov, A. S. Mayorov, N. M. R. Peres, A. H. C. Neto, J. Leist, A. K. Geim, L. A. Ponomarenko, and K. S. Novoselov, *Electron Tunneling through Ultrathin Boron Nitride Crystalline Barriers*, Nano Letters **12**, 1707 (2012).

[198] J. Feng, X. Qian, C.-W. Huang, and J. Li, *Strain-engineered artificial atom as a broad-spectrum solar energy funnel*, Nat Phot **6**, 866 (2012).

[199] M. O. Scully and M. S. Zubairy, *Quantum Optics* (Cambridge University Press, Cambridge, England, 1997.

[200] S. Mukamel, *Principles of Nonlinear Optical Spectroscopy* (Oxford University Press, New York, 1995.

[201] K. Bott, O. Heller, D. Bennhardt, S. T. Cundiff, P. Thomas, E. J. Mayer, G. O. Smith, R. Eccleston, J. Kuhl, and K. Ploog, *INFLUENCE OF EXCITON-EXCITON INTERACTIONS ON THE COHERENT OPTICAL-RESPONSE IN GAAS QUANTUM-WELLS*, Phys. Rev. B **48**, 17418 (1993).

[202] G. Nardin, G. Moody, R. Singh, T. M. Autry, H. Li, F. Morier-Genoud, and S. T. Cundiff, *Coherent Excitonic Coupling in an Asymmetric Double InGaAs Quantum Well Arises from Many-Body Effects*, Phys. Rev. Lett. **112**, 046402 (2014).

[203] G. Moody, I. A. Akimov, H. Li, R. Singh, D. R. Yakovlev, G. Karczewski, M. Wiater, T. Wojtowicz, M. Bayer, and S. T. Cundiff, *Coherent Coupling of Excitons and Trions in a Photoexcited CdTe/CdMgTe Quantum Well*, Phys. Rev. Lett. **112**, 097401 (2014).

[204] J. Kasprzak, B. Patton, V. Savona, and W. Langbein, *Coherent coupling between distant excitons revealed by two-dimensional nonlinear hyperspectral imaging*, Nat Phot **5**, 57 (2011).

[205] G. Moody, R. Singh, H. Li, I. A. Akimov, M. Bayer, D. Reuter, A. D. Wieck, A. S. Bracker, D. Gammon, and S. T. Cundiff, *Influence of confinement on biexciton binding in semiconductor quantum dot ensembles measured with two-dimensional spectroscopy*, Phys. Rev. B **87**, 041304 (2013).

[206] A. Ishizaki and G. R. Fleming, *On the Interpretation of Quantum Coherent Beats Observed in Two-Dimensional Electronic Spectra of Photosynthetic Light Harvesting Complexes*, Journal of Physical Chemistry B **115**, 6227 (2011).

[207] I. Kylänpää and H.-P. Komsa, *Binding energies of exciton complexes in transition metal dichalcogenide monolayers and effect of dielectric environment*, Phys. Rev. B **92**, 205418 (2015).

[208] K. W. Stone, K. Gundogdu, D. B. Turner, X. Q. Li, S. T. Cundiff, and K. A. Nelson, *Two-Quantum 2D FT Electronic Spectroscopy of Biexcitons in GaAs Quantum Wells*, Science **324**, 1169 (2009).

[209] H. Li, A. D. Bristow, M. E. Siemens, G. Moody, and S. T. Cundiff, *Unraveling quantum pathways using optical 3D Fourier-transform spectroscopy*, Nat Comm **4**, 1390 (2013).

[210] K. Kheng, R. T. Cox, Y. Merle A., F. Bassani, K. Saminadayar, and S. Tatarenko, *Observation of negatively charged excitonsX−in semiconductor quantum wells*, Phys. Rev. Lett. **71**, 1752 (1993).

[211] G. Finkelstein, H. Shtrikman, and I. Bar-Joseph, *Optical Spectroscopy of a Two-Dimensional Electron Gas near the Metal-Insulator Transition*, Phys. Rev. Lett. **74**, 976 (1995).

[212] S. Wu, S. Buckley, J. R. Schaibley, L. Feng, J. Yan, D. G. Mandrus, F. Hatami, W. Yao, J. Vuckovic, A. Majumdar, and X. Xu, *Monolayer semiconductor nanocavity lasers with ultralow thresholds*, Nature **520**, 69 (2015).

[213] M. Buscema, J. O. Island, D. J. Groenendijk, S. I. Blanter, G. A. Steele, H. S. J. v. d. Zant, and A. Castellanos-Gomez, *Photocurrent generation with two-dimensional van der Waals semiconductors*, Chem. Soc. Rev. **44**, 3691 (2015).

[214] C. H. Lui, A. J. Frenzel, D. V. Pilon, Y.-H. Lee, X. Ling, G. M. Akselrod, J. Kong, and N. Gedik, *Trion-Induced Negative Photoconductivity in Monolayer MoS2*, Phys. Rev. Lett. **113**, 166801 (2014).

[215] K. He, N. Kumar, L. Zhao, Z. Wang, K. F. Mak, H. Zhao, and J. Shan, *Tightly Bound Excitons in MonolayerWSe2*, Phys. Rev. Lett. **113**, 026803 (2014).

[216] B. Zhu, X. Chen, and X. Cui, *Exciton binding energy of monolayer WS2*, Sci. Rep. **5**, 9218 (2015).

[217] A. Boulesbaa, B. Huang, K. Wang, M.-W. Lin, M. Mahjouri-Samani, C. Rouleau, K. Xiao, M. Yoon, B. Sumpter, A. Puretzky, and D. Geohegan, *Observation of two distinct negative trions in tungsten disulfide monolayers*, Phys. Rev. B **92**, 115443 (2015).

[218] A. Ramasubramaniam, *Large excitonic effects in monolayers of molybdenum and tungsten dichalcogenides*, Phys. Rev. B **86**, 115409 (2012).

[219] C. Zhang, H. Wang, W. Chan, C. Manolatou, and F. Rana, *Absorption of light by excitons and trions in monolayers of metal dichalcogenideMoS2: Experiments and theory*, Phys. Rev. B **89**, 205436 (2014).

[220] T. Koyama, S. Shimizu, Y. Miyata, H. Shinohara, and A. Nakamura, *Ultrafast formation and decay dynamics of trions in p-doped single-walled carbon nanotubes*, Phys. Rev. B **87**, 165430 (2013).

[221] T. Nishihara, Y. Yamada, M. Okano, and Y. Kanemitsu, *Trion formation and recombination dynamics in hole-doped single-walled carbon nanotubes*, App. Phys. Lett. **103**, 023101 (2013).

[222] J. R. Schaibley, T. Karin, H. Yu, J. S. Ross, P. Rivera, A. M. Jones, M. E. Scott, J. Yan, D. G. Mandrus, W. Yao, K.-M. Fu, and X. Xu, *Population Pulsation Resonances of Excitons in MonolayerMoSe2with Sub-1 μeVLinewidths*, Phys. Rev. Lett. **114**, 137402 (2015).

[223] D. MacNeill, C. Heikes, K. F. Mak, Z. Anderson, A. Kormányos, V. Zólyomi, J. Park, and D. C. Ralph, *Breaking of Valley Degeneracy by Magnetic Field in MonolayerMoSe2*, Phys. Rev. Lett. **114**, 037401 (2015).

[224] See Supplementary Information for details.

[225] A. Singh, G. Moody, S. Wu, Y. Wu, N. J. Ghimire, J. Yan, D. G. Mandrus, X. Xu, and X. Li, *Coherent Electronic Coupling in Atomically Thin MoSe2*, Phys. Rev. Lett. **112**, 216804 (2014).

[226] Q. Wang, S. Ge, X. Li, J. Qiu, Y. Ji, J. Feng, and D. Sun, *Valley Carrier Dynamics in Monolayer Molybdenum Disulfide from Helicity- Resolved Ultrafast Pump-Probe Spectroscopy*, ACS Nano **7**, 11087 (2013).

[227] D. Sanvitto, R. A. Hogg, A. J. Shields, M. Y. Simmons, D. A. Ritchie, and M. Pepper, *Formation and Recombination Dynamics of Charged Excitons in a GaAs Quantum Well*, Phys. Stat. Sol. (b) **227**, 297 (2001).

[228] P. Kossacki, V. Ciulin, M. Kutrowski, J.-D. Ganie, T. Wojtowicz, and B. Deveaud, *Formation Time of Negatively Charged Excitons in CdTe-Based Quantum Wells*, Phys. Stat. Sol. (b) **229**, 659 (2002).

[229] M. M. Glazov, E. L. Ivchenko, G.Wang, T. Amand, X. Marie, B. Urbaszek, and B. L. Liu, *Spin and valley dynamics of excitons in transition metal dichalcogenides*, Phys. Stat. Sol. (B) **252**, 2349 (2015).

[230] R. Matsunaga, K. Matsuda, and Y. Kanemitsu, *Observation of Charged Excitons in Hole-Doped Carbon Nanotubes Using Photoluminescence and Absorption Spectroscopy*, Phys. Rev. Lett. **106** (2011).

[231] F. Wang, G. Dukovic, L. E. Brus, and T. F. Heinz, *The Optical Resonances in Carbon Nanotubes Arise from Excitons*, Science **308**, 838 (2005).

[232] G. Bastard, E. E. Mendez, L. L. Chang, and L. Esaki, *Exciton binding energy in quantum wells*, Phys. Rev. B **26**, 1974 (1982).

[233] H. L. Shi, H. Pan, Y. W. Zhang, and B. I. Yakobson, *Quasiparticle band structures and optical properties of strained monolayer MoS2 and WS2*, Phys. Rev. B **87**, 155304, 155304 (2013).

[234] A. V. Kavokin, *Exciton oscillator strength in quantum wells: From localized to free resonant states*, Phys. Rev. B **50**, 8000 (1994).

[235] C. Rudamas, J. Martinezpastor, L. Gonzalez, A. Vinattieri, and M. Colocci, *Temperature dependence of the effective mobility edge and recombination dynamics of free and localized excitons in InGaP/GaAs quantum wells*, Physica E **17**, 206 (2003).

[236] G. Nardin, T. M. Autry, G. Moody, R. Singh, H. Li, and S. T. Cundiff, *Multi-dimensional coherent optical spectroscopy of semiconductor nanostructures: Collinear and non-collinear approaches*, J. App. Phys. **117**, 112804 (2015).

[237] H. Dery and Y. Song, *Polarization analysis of excitons in monolayer and bilayer transition-metal dichalcogenides*, Phys. Rev. B **92**, 125431 (2015).

[238] X.-X. Zhang, Y. You, S. Yang, F. Zhao, and T. F. Heinz, *Experimental Evidence for Dark Excitons in Monolayer WSe2*, Phys. Rev. Lett. **115**, 257403 (2015).

[239] G. Wang, I. C. Gerber, L. Bouet, D. Lagarde, A. Balocchi, M. Vidal, T. Amand, X. Marie, and B. Urbaszek, *Exciton states in monolayer MoSe 2 : impact on interband transitions*, 2D Materials **2**, 045005 (2015).

[240] C. Mai, Y. G. Semenov, A. Barrette, Y. Yu, Z. Jin, L. Cao, K. W. Kim, and K. Gundogdu, *Exciton valley relaxation in a single layer of WS2 measured by ultrafast spectroscopy*, Phys. Rev. B **90** (2014).

[241] D. Lagarde, L. Bouet, X. Marie, C. R. Zhu, B. L. Liu, T. Amand, P. H. Tan, and B. Urbaszek, *Carrier and Polarization Dynamics in Monolayer MoS2*, Phys. Rev. Lett. **112**, 047401 (2014).

[242] E. A. A. Pogna, M. Marsili, D. D. Fazio, S. D. Conte, C. Manzoni, D. Sangalli, D. Yoon, A. Lombardo, A. C. Ferrari, A. Marini, G. Cerullo, and D. Prezzi, *Photo-Induced Bandgap Renormalization Governs the Ultrafast Response of Single-Layer MoS2*, Acs Nano (2015).

[243] A. Arora, M. Koperski, K. Nogajewski, J. Marcus, C. Faugeras, and M. Potemski, *Excitonic resonances in thin films of WSe2 : from monolayer to bulk material*, Nanoscale **7**, 10421 (2015).

[244] D. A. Kleinman and R. C. Miller, *Band-gap renormalization in semiconductor quantum wells containing carriers*, Phys. Rev. B **32**, 2266 (1985).

[245] H. Wang, C. Zhang, W. Chan, C. Manolatou, S. Tiwari, and F. Rana, *Radiative Lifetimes of Excitons and Trions in Monolayers of Metal Dichalcogenide MoS2*, arXiv:1409.3996v1 (2014).

[246] Y. You, X.-X. Zhang, T. C. Berkelbach, M. S. Hybertsen, D. R. Reichman, and T. F. Heinz, *Observation of biexcitons in monolayer WSe2*, Nat Phys **11**, 477 (2015).

[247] G. Plechinger, P. Nagler, J. Kraus, N. Paradiso, C. Strunk, C. Schüller, and T. Korn, *Identification of excitons, trions and biexcitons in single-layer WS2*, physica status solidi (RRL)-Rapid Research Letters **9**, 457 (2015).

[248] D. K. Zhang, D. W. Kidd, and K. Varga, *Excited Biexcitons in Transition Metal Dichalcogenides*, Nano Letters **15**, 7002 (2015).

[249] D. K. Zhang, D. W. Kidd, and K. Varga, *The biexciton puzzle*, arXiv preprint arXiv:1507.07858 (2015).

[250] K. A. Velizhanin and A. Saxena, *Excitonic effects in two-dimensional semiconductors: Path integral Monte Carlo approach*, Phys. Rev. B **92**, 195305 (2015).

[251] T. C. Damen, K. Leo, J. Shah, and J. E. Cunningham, *Spin relaxation and thermalization of excitons in GaAs quantum wells*, App. Phys. Lett. **58**, 1902 (1991).

[252] J. M. Kikkawa and D. D. Awschalom, *Resonant spin amplification in n-type GaAs*, Phys. Rev. Lett. **80**, 4313 (1998).

[253] J. M. Kikkawa, I. P. Smorchkova, N. Samarth, and D. D. Awschalom, *Room-Temperature Spin Memory in Two-Dimensional Electron Gases*, Science **277**, 1284 (1997).

[254] R. Dingle, H. L. Störmer, A. C. Gossard, and W. Wiegmann, *Electron mobilities in modulation-doped semiconductor heterojunction superlattices*, App. Phys. Lett. **33**, 665 (1978).

[255] L. Yang, N. A. Sinitsyn, W. Chen, J. Yuan, J. Zhang, J. Lou, and S. A. Crooker, *Long-lived nanosecond spin relaxation and spin coherence of electrons in monolayer MoS2 and WS2*, Nat Phys **11**, 830 (2015).

[256] W.-T. Hsu, Y.-L. Chen, C.-H. Chen, P.-S. Liu, T.-H. Hou, L.-J. Li, and W.-H. Chang, *Optically initialized robust valley-polarized holes in monolayer WSe2*, Nat Comm **6** (2015).

[257] M. Takashi, H. Satoshi, F. Toshio, and N. Kazuo, *A New Field-Effect Transistor with Selectively Doped GaAs/n-Al x Ga 1- x As Heterojunctions*, Japanese Journal of Applied Physics **19**, L225 (1980).

[258] G. Yusa, H. Shtrikman, and I. Bar-Joseph, *Onset of exciton absorption in modulation-doped GaAs quantum wells*, Phys. Rev. B **62**, 15390 (2000).

[259] I. Y. Gerlovin, Y. P. Efimov, Y. K. Dolgikh, S. A. Eliseev, V. V. Ovsyankin, V. V. Petrov, R. V. Cherbunin, I. V. Ignatiev, I. A. Yugova, L. V. Fokina, A. Greilich, D. R. Yakovlev, and M. Bayer, *Electron-spin dephasing in $\mathrm{GaAs}/{\mathrm{Al}}_{0.34}{\mathrm{Ga}}_{0.66}\mathrm{As}$ quantum wells with a gate-controlled electron density*, Physical Review B **75**, 115330 (2007).

[260] S. T. Cundiff, *Effects of correlation between inhomogeneously broadened transitions on quantum beats in transient four-wave mixing*, Phys. Rev. A **49**, 3114 (1994).

[261] M. M. Benameur, B. Radisavljevic, J. S. Héron, S. Sahoo, H. Berger, and A. Kis, *Visibility of dichalcogenide nanolayers*, Nanotechnology **22**, 125706 (2011).

[262] H. Zhang, Y. Wan, Y. Ma, W. Wang, Y. Wang, and L. Dai, *Interference effect on optical signals of monolayer MoS2*, App. Phys. Lett. **107**, 101904 (2015).